PHD

Thesis

On

PU Elastomers and Grafted GO/PU Nanocomposite with Self-Healing and Self-Adapting Capabilities for Next-Generation Electrical Insulation

by

TIAN TAN

(*Ph.D. Student Id. 201977395)*

Under the guidance of

Prof. Wah Hoon Siew

(*First Supervisor*)

&

Dr. Martin Given

(*Second Supervisor*)

&

Prof. John Liggat

(*Third Supervisor*)

Department of Electronic and Electrical Engineering University of Strathclyde,

Glasgow G1 1XQ, U.K.

This thesis is submitted for the award of the degree of

Doctor of Philosophy 2023

Declaration

This thesis is the result of the author's original research. It has been composed by the author and has not been previously submitted for examination which has led to the award of a degree.

Signed: TIAN TAN

Date: 31/05/2024

Acknowledgements

I would like to express my sincere appreciation to my first supervisor, Prof. Wah Hoon Siew, whose wealth of experience and knowledge has been the greatest help to my Ph.D. career. With his serious scientific spirit, solid knowledge, and optimistic attitude, he inspired me every day and night. Without his persistent guidance, I would not have been able to complete my Ph.D. study.

I would also like to thank my second supervisor Dr. Martin Given and third supervisor Prof. John Liggat, as them were always friendly and approachable whenever I need assistance. With their professional knowledge, they have helped me to solve many problems that I have encountered in my research.

I really want to extend my special thanks to my host supervisor, Prof. Jinliang He of Tsinghua University. Thanks to his help, I was able to conduct my experimental work at Tsinghua University via the international Strategic Partnership. Adequate funding and equipment support were essential for me to carry out my research successfully.

Further, I owe my sincere appreciation to Prof. Qi Li of Tsinghua University for his long-term support and guidance for my research. With his world-class scientific vision, Prof. Li has been a great help to me in my research on smart dielectric materials.

Last but not least, I owe my sincere appreciation to my colleagues of University of Strathclyde, Dr. Xuhui Duan, Dr. Xiaosi Lin, Mr. Abdul Samad, and colleagues of Tsinghua University, Dr. Shangshi Huang, Dr. Yujie Zhu, Dr. Rui Wang, Dr. Shaojie Wang, Dr. Shishun Hu, Mr. Xinhua Dong, Mr. Lu Han, and Ms. Bingying Chen of North China Electrical Power University, for the numerous ideas exchange, inspiration and help when I encountered difficulties.

Finally, a big thanks to my parents and my fiancée Ms. Liang for supporting me to realize my dream. Also, my sincere appreciation to the University of Strathclyde, a wonderful place that teaches useful learning and provides a world learning research environment. More importantly, I'm a recipient of a partial scholarship supported by the University's International Strategic Partnership with Tsinghua University, and I am also

grateful to the University and my department for providing financial support for the related travel.

Abstract

The demand for next-generation dielectric materials with substantially improved reliability is spurred by the development of global energy industry, where extremely harsh operating environment for electrical and electronic materials and increasingly complex insulation system are present. In order to solve the problem of local electric field distortion and electrical damage of insulating materials in high-voltage electrical equipment, the development of a dielectric material with simultaneous self-healing and self-adaptive electrical properties is an enabling material to achieve this goal but has not yet been realised. In this study, the structure-activity relationship between the microphase-separated structure and the electrical properties of polyurethane elastomers (PUs) is clarified by investigating the morphology, chemical, and electronic structure of PUs with respect to their macroscopic insulating properties. Self-healing capability of electrical damage in PUs with high dielectric strength was achieved using reversible hydrogen bonding network and shape memory effect. By further grafting two-dimensional graphene oxide (GO) nanosheets as the conductive backbone and regulating the concentration of nanoparticles and their interfacial states, it was shown that the GO/PU composites have excellent nonlinear response while retaining the self-healing capability, which has an excellent potential to be developed into a new generation of smart insulating materials.

Firstly, the structure-activity relationship of PU elastomers is investigated comprehensively utilising quantum chemical simulation, chemical-physical structure characterisation and molecular relaxation behaviour to instruct the preparation of the desire PU materials. As a result of the inconsistency in the energy levels of the molecular orbitals between the internal soft segments (SS) and hard segments (HS), the microphase-separated PU possesses a deeper energy barrier between the SS and HS interfaces, which significantly enhances the insulating performance of the material. Subsequently, the reversible hydrogen bonding network and shape memory effect of the screened PU with robust dielectric strength are verified by variable temperature infrared spectrum and calculated conformation entropy, respectively, which are the main driving forces to achieve the self-healing function. 2D optical micrographs, 3D computed micro-

X-ray tomography, and cross-sectional SEM images all confirmed that the micro dendritic defects in the designed PU are completely healed under moderate thermal stimulation, while restoring its insulating strength evaluated by the maximum discharge amplitude (Q_m) of the partial discharge.

Additionally, isocyanate grafted GO nanosheets are introduced into the self-healing PU matrix with the purpose of enabling the nanocomposite to acquire self-adaptive capabilities. The nanocomposite with a 5% volume fraction of GO exhibits superior nonlinear electrical behaviour with a switching field strength of 0.7 kV/mm, a nonlinear coefficient of 4.7, which are much better than those of traditional GO blended composites with a switching field strength of 8.5 kV/mm, a nonlinear coefficient of 2.3. The significantly improved nonlinear characteristic including the switching field strength and the nonlinear coefficient of the grafted nanocomposite is mainly attributed to the tailored interface between GO and PU matrix with considerably lowered interfacial energy barrier, as confirmed by quantum chemical calculations, nanoscale Kelvin probe force microscopy (KPFM) and macroscopic thermally stimulated current. The application of this grafted GO/PU nanocomposite exhibited excellent self-adaptive field grading capability at typical triple junction with field distortion. The grafted GO/PU nanocomposites reveal repeatable self-healing capabilities under the stimulation both of light irradiation and heating, involving the recovery of its novel nonlinear electrical properties and structural restoration. This versatile grafted GO/PU nanocomposite is expected to be promising for next-generation electrical insulation.

Table of contents

List of Acronyms

3D-CT	**three-dimension computerized tomography**
AFM	**atomic force microscopy**
BDO	**butanediol**
DC	**direct current**
DFT	**density functional theory**
DMF	**Dimethylformamide**
DOS	**density of state**
DRS	**dielectric relaxation spectrum**
DSC	**differential scanning calorimetry**
EFM	**electrostatic force microscopy**
FTIR	**Fourier-transform infrared spectrometer**
GO	**graphene oxide**
HDI	**hexamethylene diisocyanate**
HS	**hard segment**
HV	**high voltage**
IPDI	**isophorone diisocyanate**
KPFM	**Kelvin probe force microscopy**
MDI	**methylene diphenyl diisocyanate**
PD	**partial discharge**
PDOS	**partial density of state**
PPG	**polypropylene glycols**
PTMEG	**poly-tetramethylene ether glycol**
PU	**polyurethane**
SAD	**self-adaptive dielectric**
SEM	**scanning electron microscopy**
SHD	**self-healing dielectric**
SMASH	**shape memory assists self-healing**
SME	**shape memory effect**

SS	**soft segment**
TDI	**toluene diisocyanate**
TDOS	**total density of state**
TSDC	**thermal stimulation depolarization current**

List of Figures

List of Tables

Chapter 1 Introduction

1.1 Preface

Electricity is undoubtedly the most important energy contributor to humanity in the 21st century, with £11.4 billion of investment in electricity in the UK alone in 2021, increasing year on year [1]. With a solemn commitment to carbon neutrality, the UK has legislated to achieve zero carbon emissions by 2050. In order to achieve this ambitious target, it is inevitable that renewable energy, such as hydro, wind, and solar will gradually replace traditional fossil power [2]. However, renewable energy resources are distributed remote from the consumer side, and it is necessary to construct transmission networks with higher voltage levels to enable the efficient deployment of energy over long distances [3, 4, 5]. In addition, clean energy, mainly wind & solar, is highly stochastic and volatile, requiring the introduction of large-scale power electronics to maintain supply-demand balance and stability [6]. The critical dielectric insulation materials involved in developing next generation transmission and distribution systems with higher voltage levels, higher power conversion and miniaturization, longer service life and light weight will certainly entail higher requirements and expectations[7, 8, 9].

Polymers and their composites have been widely used as solid insulating components in various electrical and power electronic devices due to their ease of processing, light weight, corrosion resistance and high performance [10]. Therefore, the stability and durability of electrical devices largely depend on the insulating materials [11]. The insulation problems become more and more complicated as the voltage level rises and the size of components shrinks. Systems of more compact size require more sophisticated insulating designs to prevent insulation failure caused by localized electrical stress concentration [12]. This issue is widely prevalent in high-voltage cable terminals [13, 14] capacitor sleeves [15], and packaging materials for power electronic modules [16]. Additionally, damage or deterioration in solid dielectrics is inevitable. In the process of manufacture, transportation, and operation, polymer materials are subjected to long-term electrical, thermal, and mechanical stress, which may cause microdefects in the materials [17]. In electrical fields, microdefects tend to induce electrical field distortion, causing continuous partial discharges, which result in electron

avalanches and dendritic microchannels growing progressively in the polymer [18]. Although traditional insulating materials are designed to be as robust as possible to prevent equipment failure and prolong their service life [19, 20], the accumulation of degradation operating continuously in harsh environment will ineluctably rise to a catastrophic failure [21].

Fortunately, living organisms in an evolutionary process over millions of years have found an appropriate pathway for solving similarly complex problems [22, 23], as shown in Figure 1-1. An intriguing feature of organisms is their ability to adapt to external or internal stimuli by appropriately altering their physicochemical properties. For example, chameleons can change their skin colors by actively tuning a lattice of guanine nanocrystals in the dermis to blend in local environments to camouflage themselves from being detected by predators [24]. Sea cucumbers can switch between relaxed and stiffened states in response to external alterations through their mutable collagenous tissue [25]. Moreover, most living organisms can heal autonomously through cellular regeneration after damage, leading to functional reconstruction and performance recovery [26, 27]. Analogously, we look forward to developing a bioinspired dielectric material with simultaneous self-healable and self-adapting electrical behaviours to cope with increasingly complicated electric fields and reverse damage, for potential application in the next generation of electrical insulation.

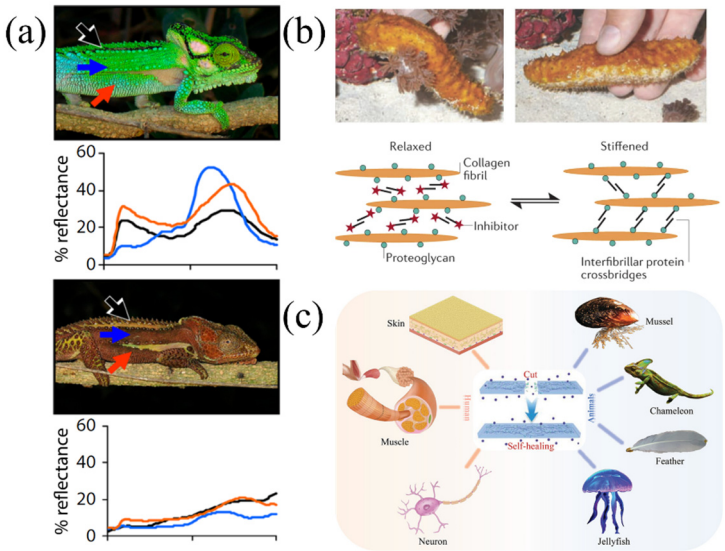

Figure 1-1: Self-adaptive and self-healing behaviour of natural organisms. (a) Changes in the skin colour and reflective spectrum of a chameleon [24]. (b) Sea cucumbers can switch between relaxed and stiffened states because of their mutable collagenous tissue [25]. (c) Self-healing behaviours of various organisms [27].

1.2 Research Motivation

Developing bioinspired smart dielectric materials for the next-generation electrical insulation with self-adaptive and self-healing capabilities is a novel solution to internal electric field grading and damage healing in power equipment [28].

Self-adaptive dielectric (SAD) of which the electrical parameters nonlinearly depend on external field strength, exhibit an excellent ability to spatially grade uneven electric fields and rapidly release intensive charges, avoiding insulation failure caused by locally intensified field [29]. Normally, SADs possess nonlinear conductivity $\sigma(E)$ or permittivity $\varepsilon(E)$ which increases rapidly with local electric field when it exceeds a certain value [7, 13]. The SADs' mechanism can be generalized as: when SADs are stressed at moderated field strength, they behave just like common dielectrics with relatively low conductivity (~10^{-14} S/m) and permittivity; and when local field strength tends to exceed the critical range, SADs exhibit much larger conductivity or permittivity as a response [30], as indicated in Figure 1-2. According to the law of current continuity shown as equation (1.1), larger conductivity σ or permittivity ε means lower field strength E under a continuous current density J, which can effectively suppress E to a safe value.

$$J(E) = \sigma(E) \times E + \varepsilon(E) \times dE / dt \tag{1.1}$$

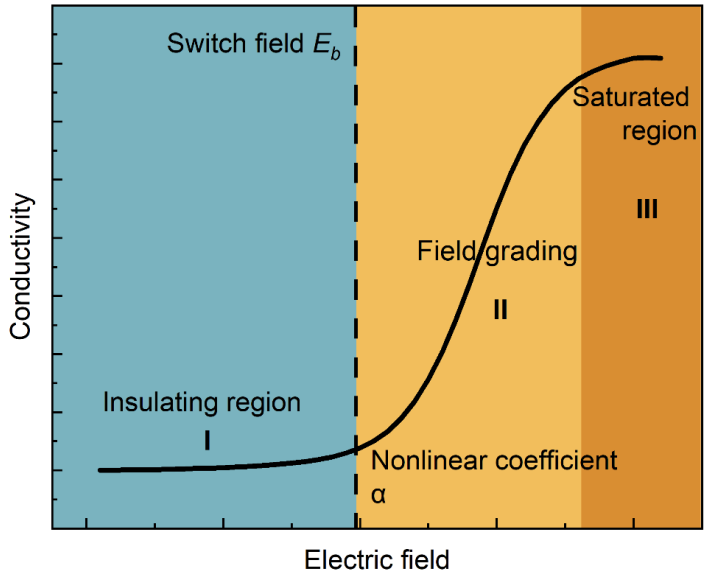

Figure 1-2: Typical nonlinear conductivity characteristics of SADs and their function region [28].

Semiconductor ceramics, such as ZnO and SiC, are widely doped into polymeric matrices to endow them with nonlinear electrical behaviours [31, 32].But the method desires a high doping concentration (usually greater than 30 vol. %) or complex synthesis method [33] to construct a percolated structure of these particles within the matrix. Heavy load of micro-sized fillers leads to poor mechanical property and large dielectric loss of the composites, which greatly limits the application of SADs in high voltage (HV) power apparatus which requires relatively high elasticity and low loss of the material. Whilst some preparation methods of SADs by applying certain AC electric field to align the functional filler to form a direct conduction pathway can reduce the concentration of filler to less than 10 vol. %, its practical application is limited by the complex fabrication techniques [34].

Self-healing dielectrics (SHD) can heal the damaged areas and recover the degraded properties of materials [35]. The approaches to achieving healable polymers generally fall into two types, intrinsic and extrinsic, differentiated by the mechanisms used to establish the healing functionality. The extrinsic self-healing process relies on microcapsules or pipes containing healing agents to achieve recovery [36, 37, 38, 39, 40]. Microcracks formed in the materials will result in the microcapsules rupturing, then releasing the healing agents and crack healing will take place. It cannot be ignored that extrinsic self-healing is not unlimited and depends on the continued availability of healing agents [41]. In contrast, intrinsic self-healing materials that can heal multiple times through inherent reversible bonds or supramolecular interactions should be more suitable for systems that require long periods of continuous operation [42]. Moreover, most of the current research focused on the healing of mechanical damage, in which fracture load and other mechanical properties were used to evaluate the efficiency of healing. With the emerging trend of designing intelligent insulating materials, the self-healing of insulation polymers is attracting more attention.

The development of bioinspired dielectric materials with simultaneous self-healable and self-adapting electrical behaviours is an enabling strategy towards the demand for next generation electrical insulation [43]. At the stage of self-adapting, the electrical parameters of the smart dielectrics vary with environmental factors to maintain performance and avoid degradation. At the stage of self-healing, the damage is repaired,

and the performance is recovered, and at the same time, the materials return to the self-adaptive stage, as exhibited in Figure 1-3. The above cycle can be repeated until the materials completely lost their autonomous functions. Compared with traditional dielectrics, the utilization of smart dielectrics not only increases the stability and prolongs the lifetime, but also reduces the costs of operation and maintenance.

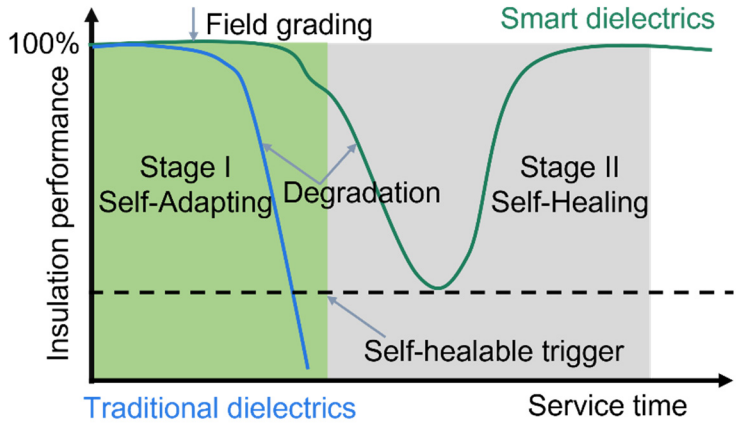

Figure 1-3: Life cycle control of bioinspired smart materials for next-generation electrical insulation.

However, no research has been carried out to organically integrate self-adaptive and self-healing functions into the same insulation materials. The aim of this research is to develop an intrinsic self-healing polymer matrix with robust dielectric properties. One of the disadvantages of intrinsic SHD is that the introduction of a large number of polar groups may lead to significant degradation of the electrical strength [44]. However, some microphase separated self-healing dielectrics, such as polyurethanes (PU), can solve this problem by maintaining high mobility in the soft phase to perform efficient self-healing while relying on the hard phase to keep the robust insulating performance (more details in section 2.5). The introduction of self-adapting function into the polymer matrix is the second key point. Having both self-adaptive and self-healing capabilities appears to be contradictory, as the high proportion of inorganic fillers inevitably restricts the movement of the polymer chains, thus, reducing the self-healing efficiency. Nevertheless, some two-dimension functional fillers might provide a mechanism to achieve a polymer that possesses both self-healing and self-adaptive properties.

1.3 Aims and Objectives

The aim of this research is to design and demonstrate a versatile smart dielectric with simultaneous self-healable and self-adapting behaviours for next generation electrical insulation. To achieve this goal, the fabrication of a self-healing polymer matrix with robust dielectric strength is the first task, as presented in Figure 1-4. The performance requirements of high voltage insulation applications and the high efficiency of self-healing need to be balanced in the design of this self-healing polymer. Furthermore, the charge transport mechanism of carefully designed percolation channels through the introduction of functional fillers will be validated and exploited to achieve excellent non-linear electrical properties in the composite. Finally, the self-healing and self-adaptive capabilities of this composite material will be tested simultaneously.

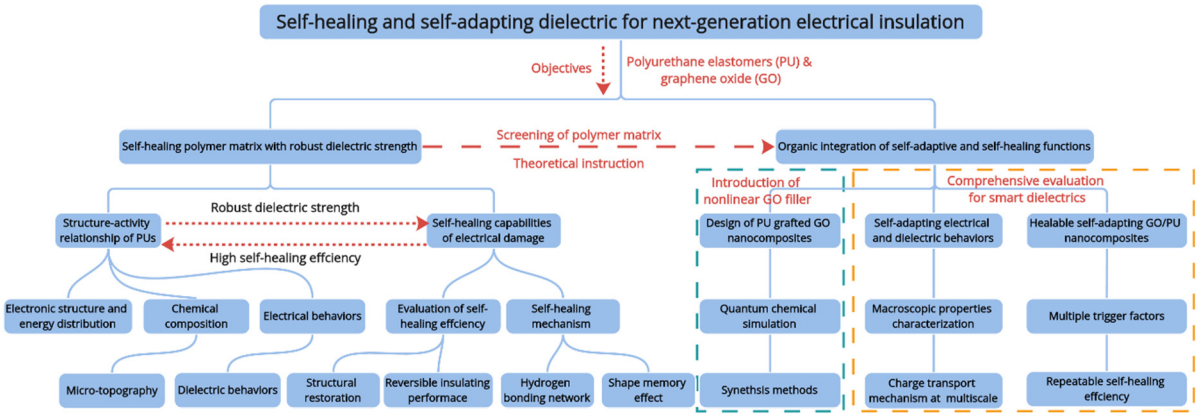

Figure 1-4: Schematic of the research route.

The objectives of this research are listed as follows:

1. Synthesizing a range of polyurethane elastomers with different molecular structures.
2. Investigating the structure-activity relationships between microphase separation of PUs and its electrical and dielectric behaviours.
3. Characterising the self-healing capabilities of electrical damage of designed PU and revealing its healing mechanisms.
4. Designing and fabricating GO grafted PU nanocomposites based on quantum chemical simulation results.

5. Elucidating the mechanism of interfacial effects on charge transport in GO/PU nanocomposites.
6. Achieving the organic integration of self-adaptive and self-healing functions in grafted GO/PU nanocomposites.

1.4 Original contributions

The research works presented in this thesis provide several original contributions in advanced dielectric materials' area which include:

i. An investigation of the structure-activity relationships between microphase separation of PUs and its electrical and dielectric behaviour (Chapter 4). The discontinuity in the energy levels of the molecular orbitals of the soft and hard segments allows for the existence of interfacial polarisation with a deeper energy level at the microphase interface of the phase-separated polyurethane, which is not conducive to carrier transport. Urethane formed from longer polyol chains have a narrower forbidden band width than that of urethane formed from shorter polyol chains. As a result, the DC breakdown strength and DC resistivity of PUs consisting of longer and more flexible polyol chains is low. This result is helpful in guiding the development of polyurethanes with desirable electrical properties.

ii. The demonstration of a self-healing PU elastomer for electrical damage with robust dielectric strength and reveal its self-healing mechanism (Chapter 5). The reversible hydrogen bonding network of the designed PU and its shape memory effect are the intrinsic mechanism for the efficient self-healing function. The designed PU shows excellent self-healing capability of electrical damage, including the recovery of insulating performance and the repair of dendritic defects.

iii. An investigation of the charge transport of GO/PU nanocomposites from nanoscale to macroscale (Chapter 6). The macroscopic nonlinear conductivity response of GO/PU nanocomposites is determined by the charge transport properties of the percolation channels formed by GO nanosheets. Two different GO-PU interfaces are constructed by solution blending and grafting

methods. The significantly improved nonlinear characteristic of the grafted nanocomposite is mainly attributed to the tailored interface between GO and PU matrix with considerably lowered interfacial energy barrier, as confirmed by quantum chemical calculations, nanoscale Kelvin probe force microscopy (KPFM) and macroscopic thermally stimulated current.

iv. Achieve the organic integration of self-adaptive and self-healing function into an insulating material by composing of a reversible hydrogen-bonding PU network with PU grafted GO as the backbone (Chapter 6). The 5 vol. % grafted GO/PU nanocomposites achieved good nonlinear electrical and dielectric response to meet the requirements of self-adaptive electric field grading, while the low doping concentration of GO did not limit the original self-healing capability of PU, and the excellent photothermal response of GO introduced a new light healing mechanism to the composites.

1.5 Thesis Outline

This thesis consists of 7 chapters. Chapter 1 includes the introduction, research motivation, research aims and objectives of the thesis.

Chapter 2 reviews the significance and research progress of self-healing and self-adapting dielectric materials in electrical insulation. The self-healing mechanisms utilised by mainstream self-healing polymer materials are summarised, and the research progress and challenges in insulating self-healing materials are highlighted, the potential advantages of polyurethane systems for developing as novel insulating dielectrics are suggested. Similarly, the current research on self-adapting dielectrics is presented. Additionally, the advantages of using polyurethane elastomers and graphene oxide to achieve these functions are discussed.

Chapter 3 introduces the methodology of this research including the materials' preparation methods and the setup of characterisation experiments. Design ideas and synthesis routes are described. The electrical, thermal, and mechanical properties and corresponding microstructural of materials are included the characterisation experiments.

Chapter 4 investigates the structure-activity relationships between microphase separation of PUs and its electrical and dielectric behaviour. A series of PUs with different phase separated structures are investigated the inter-relationship between the macroscopic electrical and dielectric properties and their microscopic parameters, suggesting important guidelines for next material design.

Chapter 5 shows the self-healing performance of PU against electrical damage. Observations from three-dimensional computed micro-X-ray tomography and optical microscope showed that the PU developed can fully heal the damaged area under moderate thermal stimulation while restoring its electrical performance. The calculation of conformational entropy and the verification of the reversibility of hydrogen bonds further illustrated the reason for efficient self-healing capability of the designed PU.

Chapter 6 designs and demonstrates a self-healable and self-adapting nanocomposite dielectric composed of a reversible hydrogen-bonding PU network with PU grafted GO as the backbone. The grafted GO/PU nanocomposites exhibit outstanding nonlinear conductivity and dielectric properties to meet the requirements of self-adaptive function for resistive or capacitive field grading. Meanwhile, the grafted GO/PU nanocomposites reveal repeatable self-healing capabilities both of thermal and light stimuli stemming from the reversible hydrogen bonding network, involving the recovery of its nonlinear electrical properties and structural restoration.

Chapter 7 contains the conclusion of the contributions in this research, together with some relevant recommendations for future work.

1.6 Author's Publications

Tan, T., Siew, WH., Han, L., Given, M., Liggat J., McKendry, C., Li, Q., He, JL. (2023). Self-Healing of electrical damage in microphase separated polyurethane elastomers with robust dielectric strength utilizing dynamic hydrogen bonding networks. *ACS Applied Polymer Materials.*

Tan, T., Siew, WH., Given, M., Liggat J., McKendry, C., Huang, ZW., Chen, HH., Li, Q., He, JL. (2023). Investigation on dielectric and electrical properties of low

concentration graphene oxide filled polyurethane nanocomposites. *International Symposium on High Voltage Engineering.*

Tan, T., Siew, WH., Given, M., McKendry, C., Liggat J., He JL. (2022). The investigation of conduction current characteristics of segmented PU elastomers. *IEEE International Conference on High Voltage Engineering and Application.*

Tan, T., Huang, ZW.**,** Siew, WH., Han, L., Given, M., Liggat J., Dong, XH., Li, Q., He, JL. (2023). Polyurethane grafted graphene oxide nanocomposites with simultaneous self-healable and self-adapting electrical and dielectric behaviors. *Advanced Materials*. (Submitted)

Chapter 2 Review of Self-Healing and Self-Adapting Dielectric Materials

2.1 Introduction

In this chapter, a review of self-healing and self-adapting dielectrics in terms of their significance, principles and their development in high voltage electrical insulation is performed. Section 2.2 covers the problems here faced by traditional dielectrics with the rapid development of high voltage electrical insulation and the necessity for the introduction of smart dielectric materials. Section 2.3 reveals the basic synthesis strategies and research status of self-healing polymer materials. Section 2.4 indicates the specificity of self-healing materials for electrical damage, as well as the research progress and shortcomings of self-healing insulating materials emerged recently. Section 2.5 introduces the potential advantages of polyurethane elastomers (PUs) for the development as smart dielectric materials. Section 2.6 summarises the main approaches to achieve self-adapting capability and their application scenario. Besides that, section 2.7 presents the potential advantages for integrating self-adaptive and self-healing functions based on graphene oxide (GO) nanosheets as functional fillers.

2.2 Dielectric Materials in the Electrical Insulation

Electricity is one of the most important forms of energy in the 21st century. Insulation systems play an important role in the safe and efficient utilisation of electricity. As the key component in insulation systems, the development of insulating materials has always been in the spotlight. Specially, the explosive growth of the power industry in recent decades has also forced researchers to develop more advanced dielectric materials to meet increasingly demanding operational requirements. As a prominent example, the external insulation systems of solar panel in spacecrafts are not only exposed to higher electrical and mechanical stresses, but also to the ever-present cosmic radiation and thermal cycling, which place more complex demands on the design of dielectric materials [45]. The construction of ultra-high and extra-high voltage power lines

demands that insulating materials work under conditions of combined voltages, space charge accumulation, and polarity reversal.

2.2.1 History of Electrical Insulating Materials

Initially, the insulation system could only use natural insulating materials, such as fibres of cellulose, mica, quartz and natural resins derived from trees and plants including pitch, rosin or linseed oil [46]. Predictably, voltage levels, operating temperatures, etc. had to be kept low to accommodate the limitations of natural materials in the early stages of the energy industry, severely limiting its development.

In 1908, electrical insulation products made from phenolic resin marked the beginning of the synthetic insulation materials. In the following decades, a large number of synthetic materials were introduced in the electrical engineering industry, including alkyd resins, aniline-formaldehyde, polyvinyl chloride (PVC), urea-formaldehyde, acrylic, polystyrene (PS) and nylon and melamine-formaldehyde, glass fibres, which lead to an explosion of new applications in electrical insulation [47]. Furthermore, polymers such as polyethylene (PE), polyurethane (PU), epoxy resins, polypropylene (PP), and polycarbonate (PC) have been widely used in high voltage insulation due to their improved electrical properties and low cost [48]. The key advantage of polymers is that their properties could be adjusted by changing their chemical composition and molecular structure in the process of synthesis. As progress was made in characterising these properties, designing molecular structures, and studying polymers' specialised properties, research on polymer insulating materials was highly successful. Manufacturers could produce insulators in various categories, meet high quality standards, and tailor the materials to meet a wide range of specifications.

However, as the further increase of voltage levels and the diversification of application scenarios, further development of pure polymer systems became limited. Pure polymers are plagued by a variety of problems during long-term operation, including space charge build-up, ageing, partial discharges, etc., which seriously threaten the reliable and safe operation of related equipment. As a result, the concept of nanodielectrics was introduced by Lewis in 1994 with the aim of improving the various performances of composites [49]. Nanodielectrics are prepared by adding nanoscale fillers to a polymeric

matrix. The interface zone, generated by two dissimilar materials (nanoparticles and polymer matrix), will increase drastically as the size of filler particles fall into nanometric scale. It has been demonstrated by large amounts of researchers that the presence of the interface has a predominant effect on the macroscopic behaviours of composites [50]. The introduction of nanofillers can significantly improve the electrical strength, thermal properties, and space charge suppression properties of composites at appropriate concentrations and interface status [51].

Zhang *et al.* incorporated poly(stearyl methacrylate)-grafted SiO_2 into crosslinked polyethylene (XLPE), and the measurements show that the accumulation of space charge was effectively suppressed, resulting in limited internal field distortion under 10.6% over a wide range of external DC field from 30 to 100 kV/mm at room temperature [52]. The deep trap introduced by nanofillers has been used to explain the space charge suppressing behaviour in nanodielectrics. Additionally, polypropylene (PP)-based nanodielectrics have been shown great potential used as recyclable HVDC cable insulation material, and its space charge characteristic has been fully studied by Zhou *et al* [3].

Higher voltage levels and smaller component sizes have made the thermal effect of electrical currents more pronounced. Thermal conductivity is an important criterion for certain insulation materials. Most of inorganic particles (e.g. BN, MgO, Al_2O_3, SiO_2, SiC), and carbon materials (e.g. carbon nanotube, graphene) have been proven to substantially increase the thermal conductivity of composites [53, 54].

Moreover, nanofiller doping is an important method of improving the PD resistance of composites. There are two main ideas to achieve this goal. On the one hand, ceramic nanoparticles are incorporated into the polymer matrix to enhance the bonding between the filler and the matrix, meanwhile, blocking the transport path of the energetic charges within the polymer [55]. A comprehensive experimental investigation of XLPE and its nanocomposite with fumed silica (SiO_2) has been performed by Tanaka *et al* [56]. The measurement shows that PD resistance is markedly improved after nanofiller addition.

On the other hand, some nanofillers with nonlinear electrical or dielectric properties can be used to achieve field grading characteristics of the nanodielectrics, which means they can homogenise the distribution of electric field, avoiding the stress concentration

[30]. Nanodielectrics with nonlinear field grading properties will be further discussed in section 2.6.

Despite the emergence of traditional nanodielectrics to improve the various properties of insulating materials, the burgeoning power industry still faces more brand-new challenges.

2.2.2 Smart Dielectric Materials for Next-Generation Electrical Insulation

The carbon-neutral vision has spawned an energy structural revolution based on equipment innovation. Insulating materials, as the foundation of electrical power equipment, faces a series of unprecedented challenges and opportunities. Electric power equipment, which includes cables, transformers, capacitors, gas-insulated switches etc., is responsible for carrying, monitoring, and regulating power flow and serves as an important part of the power grid. Being the core section of power equipment, the performance of insulating material directly determines the safety of power equipment. In the context of the construction of new power grid, the traditional power structure is transformed from thermal power to renewables, and the change in operation mode will bring severe challenges to insulating materials.

Wind power, for example, does not produce any carbon emissions and is one of the forms of power generation with the most potential. Wind now represents over half of installed renewable capacity in the UK [57]. However, as shown in Figure 2-1, large capacity wind turbines are usually located far from electrical load centres. The offshore wind power transmission calls for cross-sea large capacity electric power transmission. For such kind of application, HVDC cable power transmission becomes the best choice for long-distance offshore wind power, which is also the main direction advocated by CIGRE [58]. Higher voltage levels and longer distances in transmission networks directly affect the lifetime and safety of insulation components. The increase in the number of cable joints also exacerbates the problem of regions of uneven electric field distribution, making it difficult to design and manufacture safe and reliable insulation systems.

In contrast, on the urban electricity consumption side, compact and miniaturised power equipment has been promoted in recent years, considering the environmental impact and electromagnetic pollution. These power devices tend to be designed towards high operating voltage, with their size getting smaller and smaller, where the insulation endures complex coupled electrical, thermal, and mechanical stresses [59]. In the new power system, other critical power equipment, such as high voltage motors, power transformers, power capacitors, and power electronic devices, also suffer from more complicated insulating problems [60].

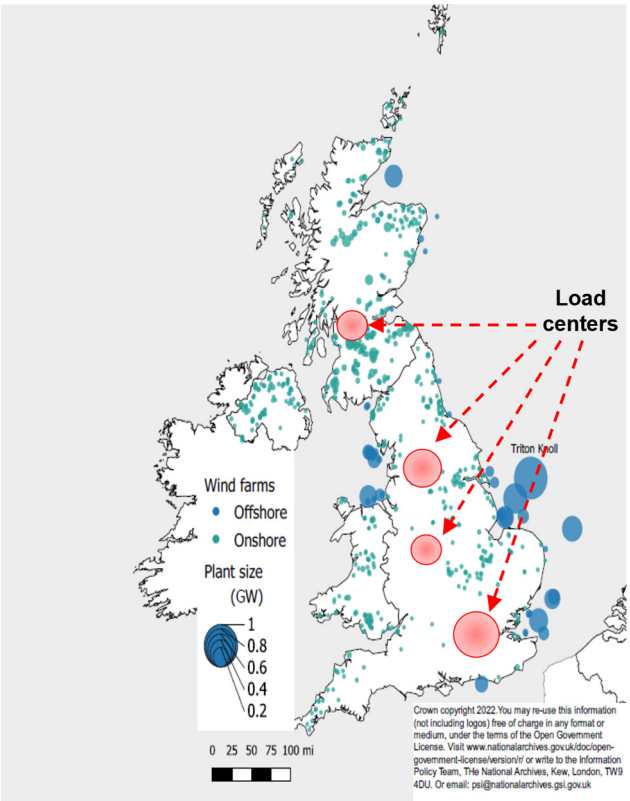

Figure 2-1: Map of UK wind capacity 2021 [57].

Improvements in insulation materials are required to the next generation high-voltage power grid that is greener, more reliable, and longer lifespan. In the field of electrical insulation, engineers look forward to designing and fabricating smart dielectric materials with bioinspired and autonomous functions to avoid and repair electrical deterioration, which is conducive to improving the robustness of the dielectric materials and prolonging their service life. Smart dielectrics, defined as functional composite materials, whose insulating properties can be automatically or semi-automatically adjusted with the electric field and the state parameters of the material itself, include adaptive field grading

materials (self-adaptive dielectrics) and self-healing dielectrics capable of repairing electrical ageing damages [28]. The research and development of smart dielectric materials plays a significant role in reducing the design and manufacturing difficulty as well as lowering the cost and improving the operational reliability of high-voltage equipment. However, most of the current research focuses only on the development of single function insulating materials, which is not beneficial for the extension of these laboratory materials to complex real-world operating conditions. The organic integration of multiple functions into a single insulating material is still unresolved. A new approach to this problem will be provided in our study.

More detailed information regarding to the principles and research status on self-healing and self-adaptive dielectric materials are presented in the following sections of this chapter.

2.3 Self-Healing Polymer Materials

In nature, biological systems can heal themselves autonomously and regenerate their structures and original set of properties after suffering from external damage. Inspired by the ability of biosystems to heal wounds autonomously, self-healing polymers have been exquisitely designed to imitate these properties using ingenious physical and chemical methods. Self-healing polymers refer to the polymers that possess the ability to repair themselves and recover their functionalities after damage using the resources inherently available to them [26, 27, 61]. As such, this approach is expected to extend the lifetime, safety, and durability of polymeric materials. The healing strategies generally fall into two categories: extrinsic and intrinsic, as indicated in Figure 2-2 [62].

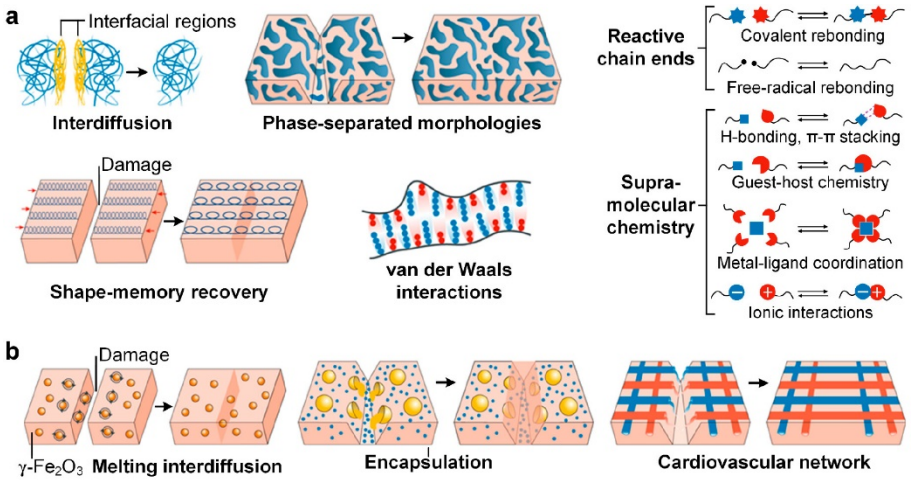

Figure 2-2: Schematic of the self-healing mechanisms in polymers, including (a) intrinsic and (b) extrinsic methods [62].

2.3.1 Extrinsic Self-Healing Strategies

The history of research into self-healing materials originates in 2001, when S. R. White et al. first proposed an extrinsic capsule-based self-healing composite [63]. Extrinsic self-healing strategies work by carrying reactive liquid healing agent in microcapsules or micro vessels, which are pre-embedded in the polymer matrix. When damage occurs, the healing agent is released, and flows into the damaged area through a capillary effect. Once the healing agent comes in contact with the catalyst that is preblended in the polymer matrix, polymerization reaction is triggered to heal the damage.

There are three main types of microcapsule-based self-healing methods, depending on the loading approaches, as shown in Figure 2-3 (a). In the first scheme (capsule-catalyst), the healing agent is an encapsulated liquid, and the polymerizer is a dispersed catalyst phase. The approach has been extensively investigated for its simple synthesis technique and is widely used in a variety of common polymer, such as epoxy resins and polydimethylsiloxane etc. [64, 65, 66, 67]. However, the performance of materials and the activity of the catalyst would be affected by the direct addition of catalyst within matrix. Hence, multi-capsule method (scheme 2) was developed by also encapsulating the catalyst to form multiple capsules systems [68, 69, 70]. This multi-capsule technique can be expanded to include as many distinct capsule types as necessary to sequester the reactive components of the healing system. Additionally, some single component self-

healing systems (scheme 3) was designed that the healing agent is encapsulated or dispersed as particles, and the polymerizer is residual reactive functionality in the matrix or an environmental stimulus, which minimises the adverse effects of the introduction of microcapsules on the composites [71, 72]. The self-healing mechanism and design process for a vascular system (Figure 2-3 (c)) is similar to that of microcapsule systems (Figure 2-3 (b)). The healing agent is encapsulated in a pre-embedded microtubules in polymer matrix. The vascular self-healing system enhances the transport capacity and storage capacity of the healing agent compared to that of microcapsule systems, increasing the number of repairs and the size of repairable regions [73, 74].

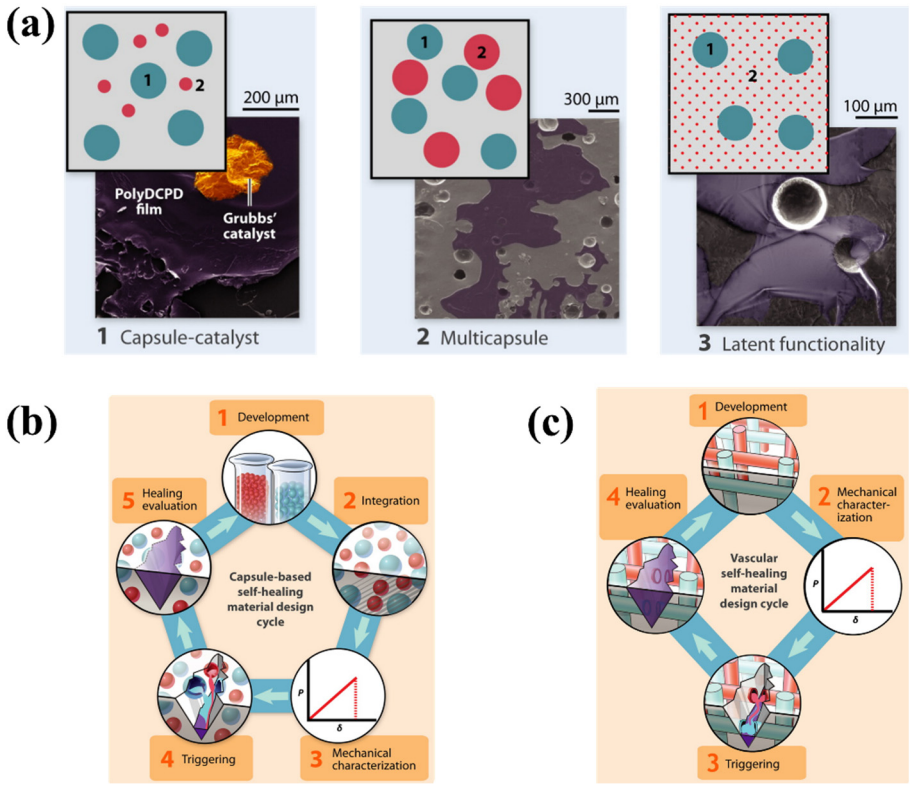

Figure 2-3: Schematic of extrinsic self-healing methods. (a) Capsule-based self-healing includes 3 main loading ways. (b) The design cycle for capsule-based self-healing materials. (c) The design cycle for vascular self-healing materials [35].

2.3.2 Intrinsic Self-Healing Strategies

Intrinsic self-healing polymers allow for autonomous repair of damage through reversible/dynamic interactions between molecules. As these interactions are reversible, the intrinsic self-healing polymers is able to achieve multiple healing cycles in the same location, contrary to extrinsic self-healing polymers which are dependent on the

availability of healing agents [75]. Notably, although intrinsic self-healing materials do not require any healing agents or catalysts, where the reversable reaction requires energy from external sources to proceed, external stimuli such as temperature, pH, irradiation, humidity etc are required. [76, 77].

As depicted in Figure 2-2 (a), the reversible dynamics of interactions utilised by intrinsic self-healing systems typically consist of two types, covalent chemical bonding, and supramolecular interactions. The reversible Diels-Alder (DA) reaction is one of the dynamic covalent bonds used in the synthesis of various intrinsic materials [78, 79, 80], in addition to disulphide bond [81], siloxane [82], diaryl-bisphenylfuranone group etc. [83]. Supramolecular chemistries concentrate on the reversible noncovalent interactions, including hydrogen bonding [84], metal–ligand coordination [85], π–π interaction [86], ionic interaction [87], and host–guest interactions [88]. Although these interactions are not as strong as covalent bonds, they can form mechanically dynamic and robust systems that are particularly attractive for designing self-healing polymers. Particularly, the shape memory effect (SME), has been recognised as an important aid to achieving efficient self-healing polymers in recent years [89, 90]. Shape memory materials are featured by the ability to recover their original shape from a significant and seemingly plastic deformation when a particular stimulus is applied [91]. During the self-healing process, the shape memory effect acts to restore entropic energy when the force causing the damage is released to fill the "open wound" in the material [92]. Due to the absence of microcapsules, intrinsic self-healing polymers are specifically suited for the incorporation of nanoparticles to tailor functionalised self-healing materials, thus, broadening their application scenarios.

2.4 Self-Healing of Electrical Damage in Insulating Materials

Although a great deal of research has been carried out on self-healing polymers, the introduction of self-healing techniques into high-voltage (HV) insulating materials still faces new challenges. Not only is there a demand for robust dielectric strength in the field of electrical insulation, but electrical damage has more complicated formation process compared to usual mechanical damage.

2.4.1 Electrical Damage in Insulating Materials

With the harsh environment of high voltage operation, polymeric dielectrics inevitably experience degradation and eventually suffer dielectric breakdown during long term operation. Electrical treeing, a pre-breakage phenomenon occurring in solid insulating polymers, is a major problem leading to failures in various HV equipment, such as HV cables, cable accessories, and power electronic equipment insulation [93]. An electrical tree can initiate from impurities, gas voids and mechanical defects, where the local electric field is distorted in small areas of the insulation material [94]. The growth of an electric tree can generally be described in three stages: initiation, propagation, and runaway [95], as presented in Figure 2-4. The initiation of an electrical tree is associated with the injection of electrical charges from high-voltage electrodes or (partial discharge) PDs that provide energy to cause physical damage and create tubulars or channels. The propagation phase of the electric tree is marked by the appearance of a current pulse due to PD in the small gas filled tubes or channels. During the runway phase, relatively few channels propagate towards the ground electrode, eventually forming a complete conductive channel where the insulation is fully destroyed. During the growth of an electrical tree most time is spent in the initiation and propagation stages, which provides a window of time to inhibit or repair these electrical damages. Conventional methods of electric tree inhibition include various types of organic or inorganic additives, the main idea of which is to inhibit the rate of electric tree growth to prolong the life of the material [96, 97, 98, 99]. These fillers can inhibit the process of electron avalanche by restricting the movement of polymer molecular chains or by adding chemical traps to capture high-energy electrons.

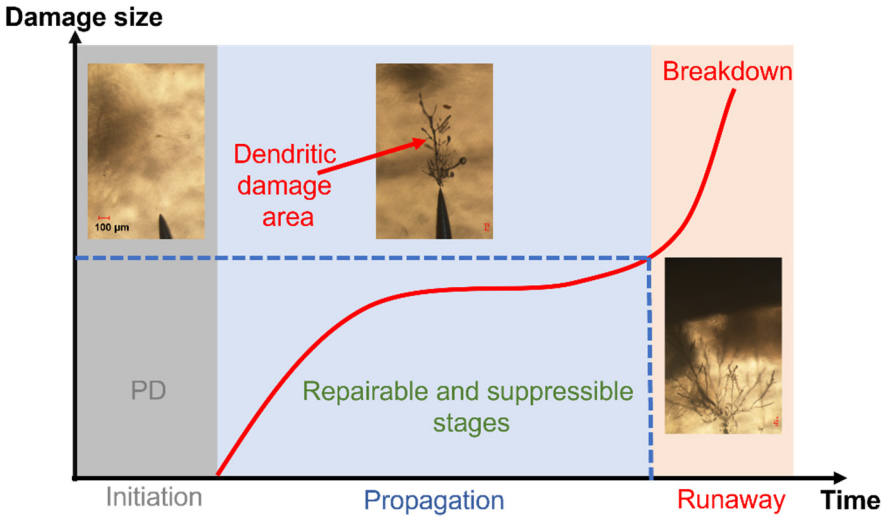

Figure 2-4: Electrical treeing growing characteristics and microscopic image [95].

2.4.2 Self-Healing Dielectrics

Self-healing materials exhibit great potential for improving the reliability, durability, and service life of insulating dielectrics. In contrast to various suppression methods for electrical tree growth, self-healing dielectrics not only eliminate the dendritic defects that have developed, but also restore the initial insulation properties and reverse the degradation state of the material.

Research into self-healing insulating materials began in 2019, when Yang et al. successfully healed electrical dendrite damage in thermoplastic polypropylene and restored the insulating properties using the thermal effects of superparamagnetic nanoparticles under an oscillating magnetic field (Figure 2-5 a) [36]. More extrinsic microcapsule-based self-healing approaches were subsequently developed using traditional polymeric dielectrics. Exploiting the specificity of electrical damage, Gao and Xie et al. designed two polymerization reaction of healing agents triggered by UV light and free radicals generated during the growth of the electrical tree (Figure 2-5 b, c), respectively [38, 40]. However, it is undeniable that the industrial application of extrinsic self-healing methods is difficult to achieve due to the exhaustion of the healing agents and the complexity of preparation techniques of microencapsulation. The introduction of microcapsules resulted in an extreme decrease in the breakdown strength of the material to about 37 kV/mm.

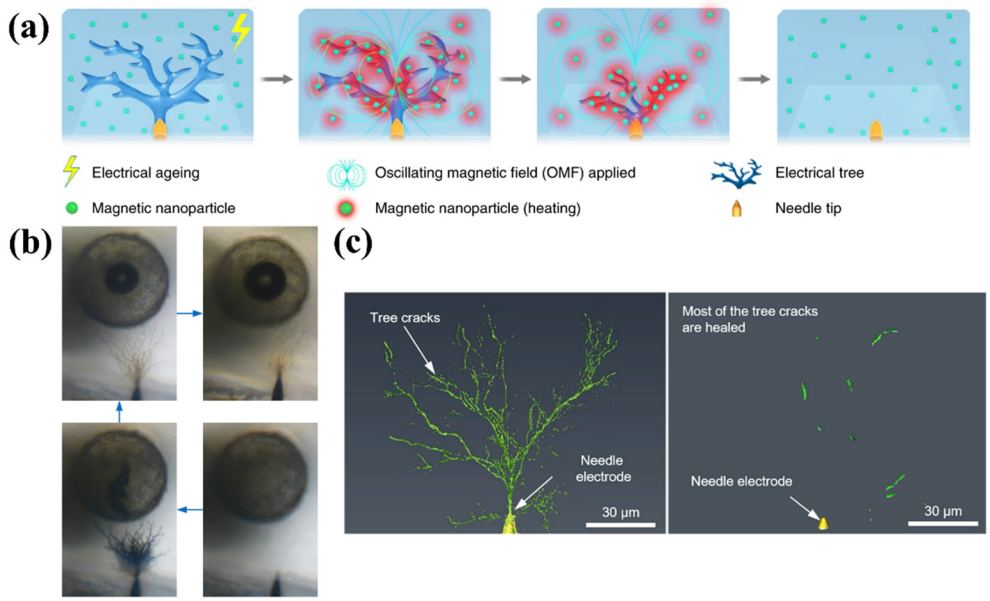

Figure 2-5: Extrinsic self-healing dielectrics. (a) Superparamagnetic nanoparticles magnetothermal healing [36]. (b) optical microscopic healing image of microcapsule-based self-healing dielectrics [38]. (c) 3D X-ray CT healing image of microcapsule-based self-healing dielectrics [40].

In contrast, intrinsic self-healing dielectrics show reproducible self-healing capabilities. Zhang et al. designed a thermoplastic methyl thioglycolate-modified styrene-butadiene-styrene elastomer modified with butadiene blocks to confer self-healing capabilities of mechanical and electrical damage [100]. Salvatierra et al. reported on the healing behaviour of silicon gels under electrical stress facilitated by incorporated liquid phase [101]. In parallel to these thermoplastic, ultra-soft gels or elastic materials, self-healing thermosetting dielectrics with robust mechanical performance have also been developed. Xie et al. designed a mechanical robust self-healing epoxy resin utilizing a reversibly convertible molecular network [42], as indicated in Figure 2-6. The introduced Diels–Alder bond endowed the material with a reversible structure between the fully cross-linked state and the partially cross-linked state. The self-healing epoxy resin can almost completely repair the electrical damage after exposure to a temperature of 130 °C for 1 h.

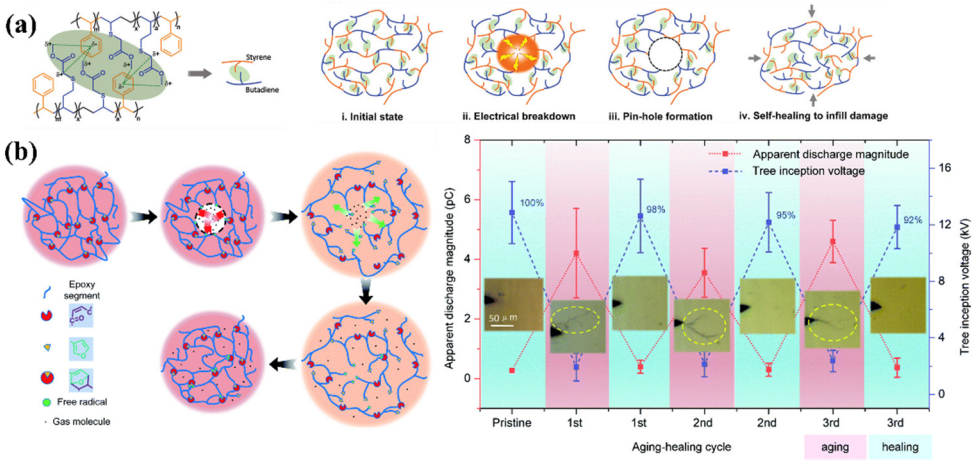

Figure 2-6: Intrinsic self-healing dielectrics. (a) Structure and healing mechanism of the healable dielectric elastomer based on electrostatic interaction [100]**. (b) The schematic diagram of repairing internal defects with self-healing polymer of interconvertible fully crosslinked and partially crosslinked states. And repeatable insulating properties recovery and dendritic channels repair during the multiple aging-healing cycles [42].**

However, both the introduction of microcapsules for extrinsic self-healing materials and the various types of polar reversible bonds for intrinsic self-healing materials result in a dramatic reduction in the electrical strength of the material. The DC breakdown strength of currently reported self-healing electrical insulating materials is generally below 50 kV/mm, which is much lower than that of typical dielectric polymers, e.g. 165 kV/mm for epoxy resins and 270 kV/mm for XLPE. The significant reduction in dielectric strength makes it less desirable for HV applications.[102].

2.5 Self-Healing Polyurethane Elastomers

In 1937, the genius German chemist Prof. Otto Bayer first synthesised a polyurethane (PU) through a normal polyaddition reaction between aliphatic diisocyanate and diamine. The chemical linkage existing in the polymer is denoted as urethane (-NHCOO-). PUs are usually synthesized by the addition of alcohols and isocyanates. Diols or polyols are the alcoholic part and the diisocyanate are reacted with them. The typical synthesis route of polyurethanes is shown in Figure 2-7, where a wide choice of raw materials is available. The most commonly used isocyanates for the synthesis of polyurethane are diphenylmethane diisocyanate (MDI) or toluene diisocyanate (TDI), hexamethylene diisocyanate (HDI) or isophorone diisocyanate (IPDI). Polyols used for the synthesis of PUs can be polyether polyols and polyester polyols. The polyether polyols are ethylene glycol, propylene glycol, poly-ethylene propylene oxide and the polyester polyols are

condensed products of adipic acid or phthalic acid with 1,4-butane diol, or 1,6-hexane diol. Another feature of PUs is that the polyol components can come from natural sources such as castor oil, soybean oil, and sunflower oil etc [103]. The synthesis of PU from renewable resources is a method adopted by many researchers. Furthermore, it is the variety of the base materials and the simplicity of the synthesis routes that make it possible to obtain a wide range of polyurethane products in a variety of styles, ranging from rigid and hard to flexible and soft. Therefore, PUs have been presented in many forms in our lives, from mobile phone cases to clothes, from furniture to cables, from cars through to the construction field.

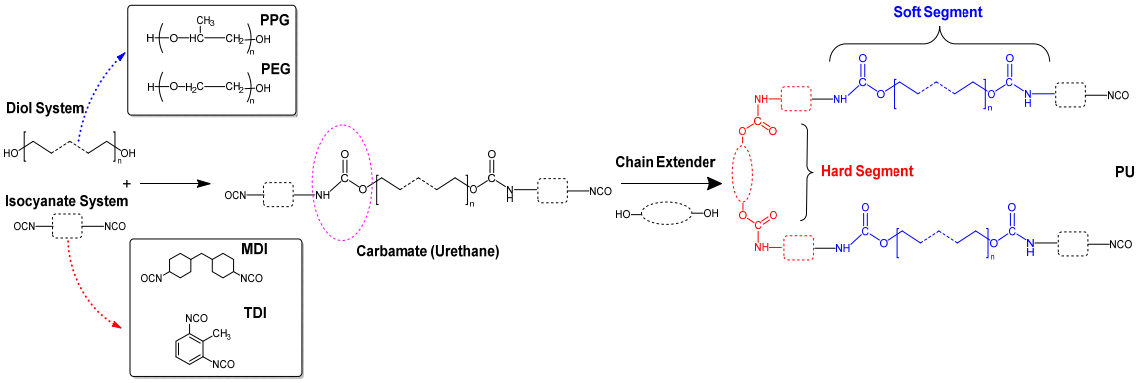

Figure 2-7: Typical synthesis route of polyurethanes.

There are two main types of PUs, PU foams and PU elastomers, based on the different synthetic route and applications. It becomes PU foam when gas is introduced, either via reaction of the isocyanate with water, or with blowing agents [104]. PU foams may be low density flexible foams or low-density rigid foams for different application field. Another important type is thermoplastic PU elastomers. PU elastomers are considered as excellent substitutes for plastics and rubbers. They have high abrasion resistance, resistance to solvents and chemicals, high impact strength, and low moisture uptake. These superior properties make them suitable for a variety of applications in the manufacturing field. Polyurethane elastomers are typically multiblock copolymers that consist of alternating hard and soft segments. Very often the flexible and long soft segments (SS) are made from long chains of polyester or polyether and the polar and rigid hard segments (HS) consist of diisocyanate and chain extenders [105]. The thermodynamic incompatibility of the HS and SS results in a unique microphase separated structure of PU at mesoscopic length scales [106]. The HS form physical

crosslinks arising from polar interactions, hydrogen bonding and potential crystallization in the hard domain, while the SS form an elastic and flexible phase [107], where the phase-separated structure is exhibited in Figure 2-8. Depending on the specific micro-phase separation structure, PU elastomers offer a series of versatile and seemingly contradictory properties, such as superior mechanical strength while retaining great elasticity and even shape memory effects, which make PU interesting for various applications, including bio-medical, automotive, and electronic industries [82, 108, 109]. Additionally, PU elastomers can be processed as typical recyclable thermoplastics due to the reversible crosslinking network composed of hydrogen bonds [110, 111]. The latter thermoplastic polyurethane elastomer is clearly more likely to be developed as a high voltage insulating material due to the ease of processing and opportunities for self-healing, so the subsequent PUs in this thesis refers to polyurethane elastomers. However, the inter-relationship between the performance of PU under HV and its structure has not been systematically elucidated, thus, hindering the introduction of PU as HV insulating materials. Consequently, one of the objectives of this research is to investigate the structure-property relationships of a series of PU formulations.

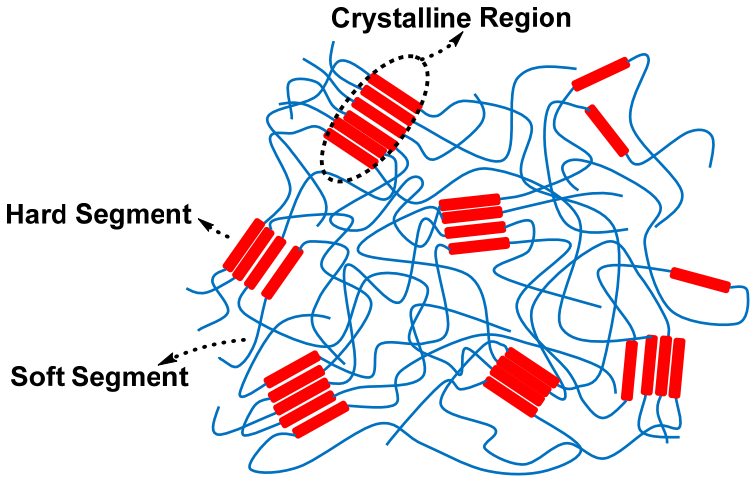

Figure 2-8: Phase-separated structure of PU elastomers. hard segment in red, soft segment in blue.

Extensive research confirms that PUs are widely suitable as a polymeric matrices for achieving self-healing capabilities, which benefits from the numerous synthetic raw materials and good mobility of SS [112]. Extrinsic self-healing PUs based on microcapsules are popular in anti-corrosive self-healing industrial coatings. Any cracks or damage to be healed could be repaired by the leakage of the healing agent from the

protective microcapsule at the site of damage. Natural vegetable oils are widely used as core healing agents and are synthesised into microcapsules by means of interfacial polymerisation to form shell materials [113]. Koh et al. developed a renewable PU microcapsule containing isosorbide derivatives for self-healing anticorrosion coatings. The efficiency of the PU microcapsules containing the self-healing corrosion inhibitor was investigated in a painting system. The results indicated that the microcapsules provided noteworthy corrosion resistance with a rusting degree in the range from 0 to 0.47% with inhibitor loading from 25 ppm to 200 ppm under accelerated corrosion testing [114]. Besides that, novel single-layer PU-type microcapsules loaded with a PU for corrosion resistance based healing agent was fabricated by Haghayegh et al. [115]. The healing agent was prepared through the reaction of an excess amount of IPDI with 2-ethyl-2-hydroxymethyl-1,3-propanediol. The healing agent was then encapsulated with a PU shell via an oil-in-water emulsion polymerization technique. Interestingly, it was observed that the microcapsules were very stable even after 10 months and lost less than 7 wt % of their loaded isocyanate molecules.

PUs is also one of the most widely available polymeric matrixes for achieving intrinsic self-healing capabilities. Zhang et al. designed a PU using TDI and BDO (butanediol) as the HS and polyether polyols as the soft segment [116]. They showed that the self-healing capability of the PU at room temperature decreased with increasing HS content based on tensile test results and the healing ability was lost when it reached 50% HS content. The self-healing capability of PU was ascribed to reversible hydrogen bonds and mobility of the SS at room temperature. Similarly, Kim et al. synthesized PU prepolymers from PTMEG (Poly-tetramethylene ether glycol) and IPDI [117]. These prepolymers were end capped with propylamine to synthesize PU urea. The urea and urethane groups undergo hydrogen-bonding formation to facilitate self-healing in these polymers. In addition to these non-covalent interactions, different types of reversible covalent bonds have been introduced into the synthesis of PUs to achieve self-healing functionality. Du et al. synthesised a thermally stimulated DA based self-healing PU v*ia* a Diels–Alder (DA) reaction between a polyurethane prepolymer end-capped with furan groups (MPF) and bismaleimide (BMI) [118]. The self-healing efficiency of the PU, determined by the recovery of breaking tensile strength, after being damaged and healed at 120 ℃ can reach up to 80%. Fu et al. used acidified multi-walled carbon

nanotubes (MWCNT) as the conductor, to develop a new kind of thermally reversible self-healing PU film that simultaneously had good processing properties, high thermal stability and great electrostatic dissipation capacity. They conjugated a multi-furan ring with liquid hyperbranched poly-siloxane terminated by multi-maleimide to form the self-healing polymer [119], as shown in Figure 2-9 (a). Multi-maleimide groups in PU-DA-CNTs provide higher proceeding possibility of the DA reaction between furan rings and maleimide groups, thus leading to a high self-healing efficiency. Yuan et al. achieve a self-healing PU elastomer (Figure 2-9 b) in which they synthesised an alkoxyamine-based diol and reacted it with tri-HDI and polyethylene glycol (PEG) [82]. The thermally dynamic reversible equilibrium between fission/recombination of C–ON bonds in alkoxyamine moieties enabled repeated cross-linking and de-crosslinking of PU chains at a certain temperature and hence facilitated crack healing. Zhang et al. developed a series of self-healing linear PUs with the disulfide linkage as the grafting point [120], as indicated in Figure 2-9 (c). The self-healing polyurethane can quickly restore its over 90% of its mechanical properties after healing at 100 °C for 10 min.

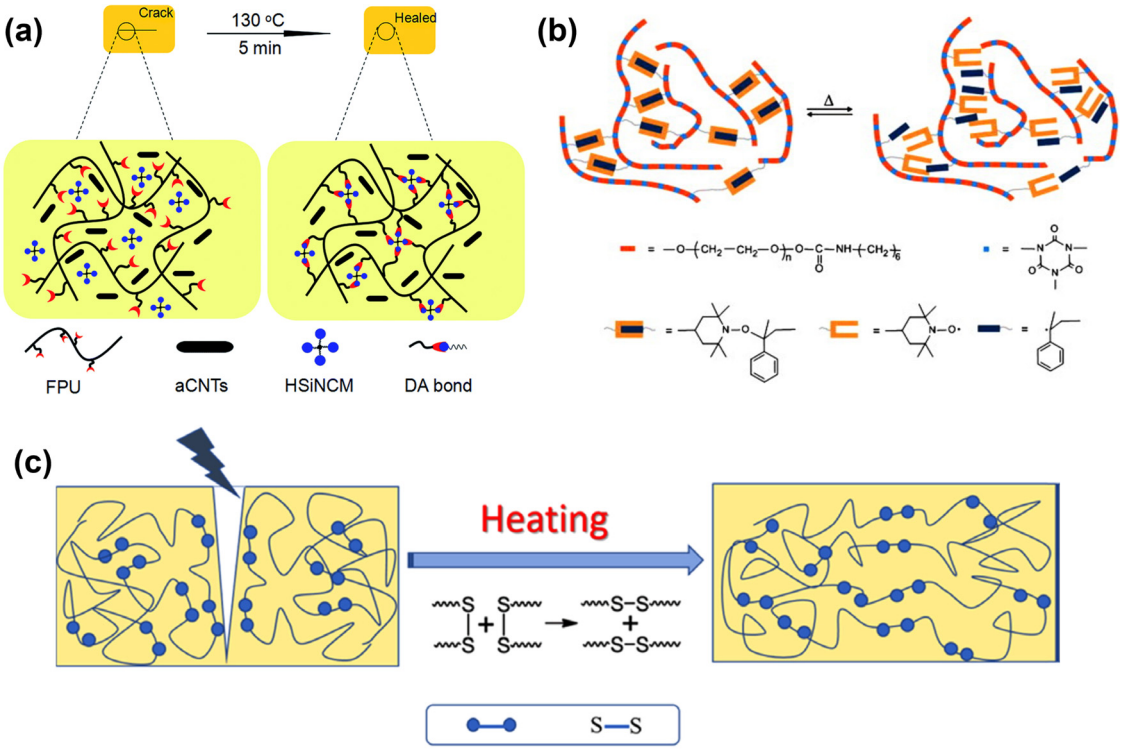

Figure 2-9: Intrinsic self-healing PUs based on reversible covalent bonds. (a) Self-healing in PU-DA-CNT films after maintaining at 130 °C for 5 min [119]**. (b) Healing mechanism of PU cross-linked by alkoxyamine** [82]**. (c) self-healing mechanism of linear PU based on disulfide linages** [120]**.**

All self-healing of structural damages requires at least two steps: close then heal, similar to the biological healing of wounds in the skin. In this process, the structural scale crack will be first sealed or closed by a certain mechanism before the potential self-healing mechanisms can take effect. With traditional self-healing polymers, artificial intervention is often necessary, such as holding the damaged area tightly in place for subsequent damage repair. Shape recovery functionality of thermally activated shape memory polymers can be utilised to achieve the self-closing purposes [121]. Shape memory assisted self-healing" (SMASH) is a concept which has emerged as a path-breaking strategy over the past decade wherein the crack closure is achieved by using smart shape memory polymers without the need for any manual intervention [122]. PU is known for the shape memory effect conferred by its block copolymer structure, which allows it to be considered an excellent candidate for SMASH applications. Xu et al. studied a smart PU composed of PTMEG, HDI, and 2-hydroxyethyl disulphide (Figure 2-10 a), which combines the self-healing properties of disulphide links with the shape memory effect of PU [123]. Autonomous healing of cracks took just 5 min and a healing process of 4 h led to almost full recovery of the mechanical properties upon heating above 80 °C by activating the shape memory effect and disulphide exchange reaction simultaneously. Van Herk et al. prepared a crosslinked SMASH PU thermoset network having PCL and a thermos-reversible cross-linker based on Triazoline Dione chemistry [124], as exhibited in Figure 2-10 (b). A single heating step at about 70 °C triggers both shape-recovery and reversible TAD chemistry, which allows fast SMASH from large scale damage up to 1 mm.

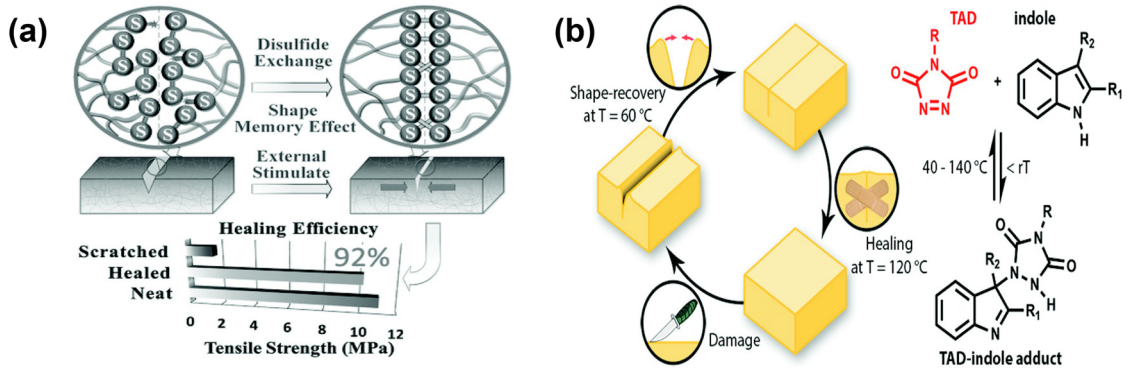

Figure 2-10: (a) Disulphide exchange reactions for SMASH PU [123]**. (b) SMASH in PU thermosets using reversible Triazoline Dione chemistry** [124]**.**

With the easy polycondensation process, tailorable characteristics, and mature experience in designing mechanically self-healing polymers, PUs are well positioned to develop into next-generation smart polymeric materials in a variety of industries. However, current research on PUs is mainly focused on the mechanical field. The relationship between its electrical properties and structure is still unclear. Besides that, the balance between the electrical strength and self-healing properties of PUs is also a tricky one. These issues will be investigated in this research for designing a self-healing PU material with robust electrical strength.

2.6 Self-Adapting Dielectrics with Nonlinear Electrical and Dielectric Behaviour

In chapter 1.2, we discussed the definition of SADs and some examples. In this section the mechanism and applications of SADs are further elaborated, while some potential methods for integrating self-healing and self-adaptive functions are also presented.

2.6.1 Self-Adaptive Dielectric Materials

In traditional approaches to achieve electric field control, material electrical property and electrode structure directly determine the spatial electric field distribution in power apparatus. Assuming the electric field (E) as the control target, this approach is an open-loop control without any feed-back mechanism. The control performance is not satisfying, and it is rather sensitive to parameter disturbance. Small discrepancies in the geometry of the field grading structure with fixed design, temperature change, and materials aging process can lead to a much different E distribution from the expectation [125]. On the contrary, field grading and stress control by SADs are typical closed-loop control. On one hand, the material parameters affect the electric field distribution; on the other hand, the electric field also feeds back to the material parameter which self-adaptively changes with it. In this case, an effective and stable field grading effect can be obtained by SADs regardless of the discrepancies in geometry, different temperatures, or material aging [28].

For SADs, the most important parameters for their performances are the switching field E_b and the nonlinear coefficient α. E_b is defined as the switching above which the

material begins to show a rapidly changing conductivity or permittivity [126, 127]. It should be adapted to specific applications as different power apparatus or electronic devices with different voltage has different requirements on the electric field. Thereby, E_b of SADs is expected to be flexibly tuned according to practical cases, which may range from 0.1 to 5 kV/mm. In terms of the nonlinear coefficient α it is the slope of current density as a function of electric field curve and reflects the degree by which the electric field changes the material parameters. The greater the α is, the better the field grading performance will be.

As polymer dielectrics do not possess desired field-dependent electrical properties, doping of functional fillers is performed to endow them with nonlinear behaviours [15]. SADs are also called nonlinear composites. Semiconductive ceramic filler, such as SiC and ZnO has been widely used to obtain nonlinear response in SADs. Ideally, the SADs have double Schottky barrier whose barrier height is tuned by the localized states and applied electric field [128]. Under a relatively low electric field, the conduction barrier is relatively high, and the composite retains a good insulation property. As the field strength increases, all the localized states are filled, and the barrier height falls dramatically. The SADs have switched to the conduction state. Hence, the quality of the nonlinear response relies on both the physical formation of the percolation pathways and the alignment of barrier height. For instance, for SiC fillers (Figure 2-11 a), the potential barrier is formed at the interface between the fillers [129], as opposed to ZnO filler (Figure 2-11 b), where the Schottky barrier is located inside the grain boundaries of each ZnO particle [130]. Obviously, the latter barrier height is highly aligned and the nonlinear properties of the ZnO composites are more stable compared to those of the SiC composites. Moreover, the through conduction paths of the functional filler, the percolation pathways, are required to guarantee stable nonlinear conducting behaviour. Percolation threshold usually depends on the geometry of the filler and is around 30% for micron-sized particles [131] but can be reduced to around 5% utilizing some low dimensional fillers with high aspect ratio, such as ZnO whisker (Figure 2-11 c) [132], or 2-D carbon fillers (Figure 2-11 d) [133]. Bespoke methods, like using an AC electric field to precisely align the conductive pathways, can also reduce the filler concentration to around 10 vol. % (Figure 2-11 d) [34].

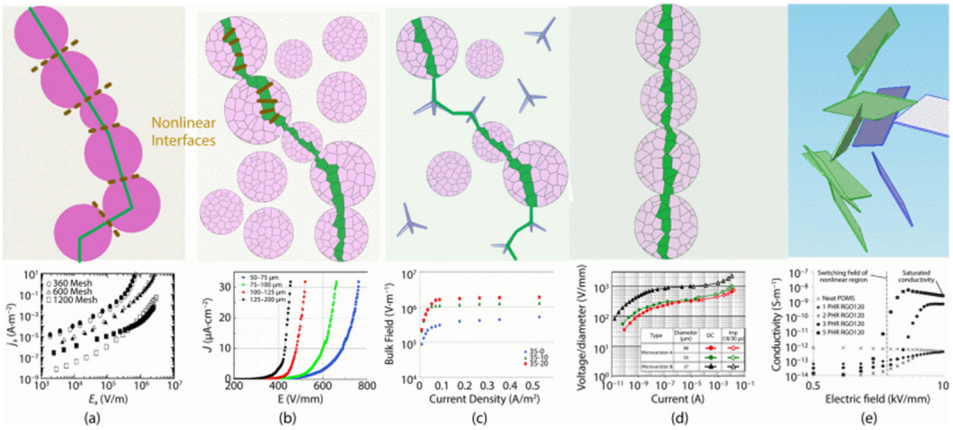

Figure 2-11: Schematic diagram and J(E) characteristics of SAD composites. (a) SiC [129]. **(b) ZnO micro varistor** [130]. **(c) ZnO microvaristor and ZnO whisker** [132]. **(d) Aligned ZnO whiskers [34]. (e) GO filler** [134].

2.6.2 Application Based on Self-Adaptive Dielectric

SADs are mainly used in electrical and electronic equipment with triple junction structures for the suppression of local field distortion [135, 136]. Yang et al. presented a design in which a SADs layer was applied near the terminals of outdoor insulators to achieve a homogenous electric distribution (Figure 2-12 a) [15]. After the optimization simulation of geometry and parameters of the SADs layer, they prepared a 220 kV prototype and electric field distribution measurements were performed by an optical electric field sensor at 10 reference points. The simulated electric field distribution on insulators with the SADs layer had a significant decrease at the end of the insulator string than the traditional insulator. Li et al. analysed the charge transport and control strategy of HVDC spacers of the GIS (gas insulated switchgear) system and put forward a novel model based on SADs to release the surface charge accumulation [137, 138, 139]. The charge adaptive spacer (CACS) was shaped like a bowl, which was composed of the insulation region and the charge adaptive control region. This design allowed the CACS to meet the requirements of the longitudinal mechanic force, and more crucially, the normal component of the electric field may be centered on the spacer's sidewall near the ground enclosure, as shown in Figure 6(a). CACS with different properties were optimized by changing the ratio of Al2O3, SiC, and epoxy resin. To prove the effect of nonlinear material on limiting surface charge, the regular spacer (RS), novel shaped spacer (NSS), and charge adaptive spacer (CACS) was compared under AC and DC surface flashover tests. The AC surface flashover voltage of NSS and CACS range from 200 to 225 kV, which were higher than RS with a breakdown value ranging from 160 to

180 kV, as shown in Figure 2-12 b. The operation reliability of high voltage bushing is a key problem in power transmission projects. With a cylindrical structure in the radial direction and a “plug-in” structure in the axial direction, the concentration of electric field may cause the discharge or even breakdown of the insulation. Zhao et al. designed a three-layer adaptive bushing based on nonlinear materials (Figure 2-12 c) [140]. The field grading layer used the conventional nonlinear composites material with a low nonlinear coefficient and high threshold electric field for the field grading in the radial distribution of electric field, while the electrode extended layer used ZnO particle loaded micro-varistors with a high nonlinear coefficient and low threshold electric field for the suppression discharge at the edge of the flange. Under the condition where the temperature difference between inner conductive rod and the outermost layer of the bushing changes in real time, the electric field inside the nonlinear bushing can always be maintained with a uniform distribution, which helps to prevent both flashover at the flange and partial discharge from the main insulating material. For application in electronics, Wang et al. first proposed the idea of using composites with nonlinear conductivity as novel packaging materials of power electronic module to achieve a homogeneous distribution of electric field [141]. A ferro-electric filler barium titanite was added into a silicon-based gel to form a composite gel with nonlinear conductivity. Using this composite gel in a power electronic module through finite element simulation, the electric field level neat the triple junction was significantly reduced. Besides that, the application of non-linear materials in high-voltage rotating motors and cables accessories has been investigated, both with excellent electric field grading results [142, 143].

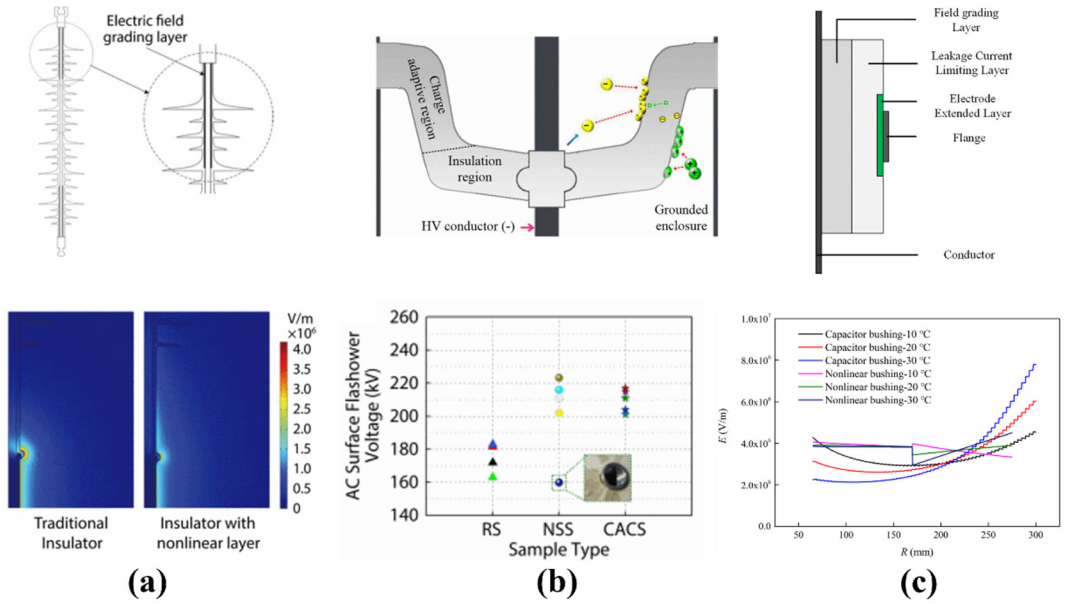

Figure 2-12: HV Application based on self-adaptive dielectrics. (a) application of SADs in polymeric outdoor insulators [15]. (b) A novel HVDC spacer based on SADs [113]. (c) Design of adaptive bushing based on SADs [140].

2.7 Graphene Oxide Nanosheets

In an effort to achieve an organic integration of self-healing and self-adaptive functionality, two issues must first be addressed. The concentration of filler should be as low as possible, provided that the percolation threshold is satisfied, in case robust fillers restrict the migration of molecular chains, thus, reducing the self-healing efficiency of the material. Then, the interface between filler and matrix should be tuneable to obtain an excellent and stable nonlinear response. With this considerations, graphene oxide (GO) emerges as a superior choice, due to its ultra-high aspect ratio and abundant surface functional groups.

Since 2004, when Novoselove et al. published their research on mechanically exfoliated monolayers of graphene (Figure 2-13 a), this single-layer, two-dimensional material of single-layered carbon atoms arranged in a honeycomb pattern has sparked great research both of scientific and engineering communities [144]. The carbon bonds are sp^2 hybridized, where the in-plane $\sigma_{C\text{-}C}$ bond is one of the strongest bonds in materials and the out-of-plane π bond, which contributes to a delocalized network of electrons, is responsible for the electron conduction of graphene and provides the weak interaction among graphene layers or between graphene and substrate. Graphene is favoured by researchers for its ultra-high carrier mobility at room temperature (~10000

$cm^2V^{-1}s^{-1}$, [144]), large theoretical specific surface area (2630 $m^2\ g^{-1}$, [145]), ultra-high Young's modulus (~1 TPa, [146]) and thermal conductivity (3000–5000 $Wm^{-1}\ K^{-1}$, [147]), is considered more promising than other nanostructured carbon allotropes, that is, one-dimensional nanotubes and 0-dimensional fullerenes, from the application viewpoint. However, pristine graphene is a hydrophobic material, and has no appreciable solubility in most solvents, which makes it extremely difficult to directly obtain graphene/polymer composites. Therefore, in the actual processing of graphene-based composites, graphene oxide (GO), a graphene derivative prepared from natural scaled graphite by the Hummer method, is widely used [148, 149, 150]. On the one hand, the large number of oxygen-containing functional groups on the bottom and edges of graphene oxide, such as epoxy groups, hydroxyl groups, carboxyl groups and carbonyl groups, as shown in Figure 2-13 (b), allows GO to be easily dispersed in polar solvents. These oxygen-containing functional groups make GO well compatible with polymer matrix, which can be used as reactive sites for the polymerization/grafting reaction with polymer chains [151]. On the other hand, the oxygen-containing functional groups disrupt the sp^2 hybridization orbitals of graphene and acts as an energy barrier for electron transport in the olefin conjugate structure [134]. This makes GO have remarkable semiconductor properties. These features allow the surface of GO to be further modified by grafting, *in situ* polymerisation etc. for tailoring the interfacial barriers and obtaining efficient nonlinear response [152, 153, 154].

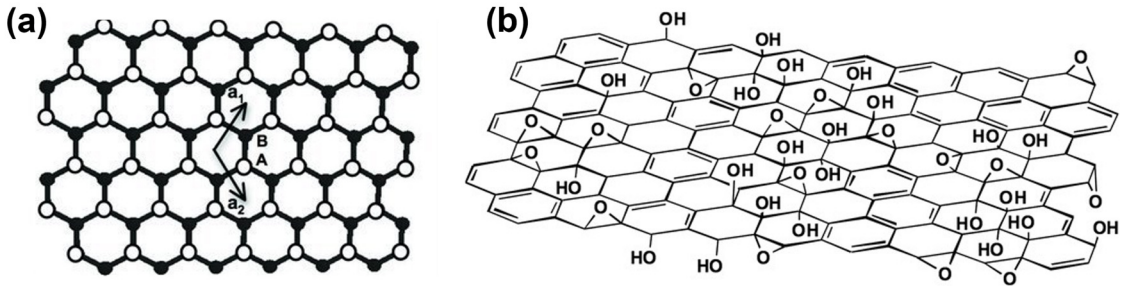

Figure 2-13: Proposed schematic of graphene (a) [144] and graphene oxide structure (b) [151].

GO and reduced GO (rGO) are important filler materials for polymer composites, because of their good conductivity, lower density, and excellent mechanical strength. Similar to the conventional polymer nanocomposites processing, the methods applied for the fabrication of GO/polymer composites are solution mixing, melt blending, and *in-situ* polymerization [155], [156], [157]. In general, GO is expected to be well

dispersed in the polymer and to have a good interfacial interaction with the matrix in order to obtain the desired composite performance. An important application of GO/rGO fillers is to largely enhance the electrical conductivity of composite. The large specific surface area of GO allows it to form percolation structures within the polymer at a relative low volume fraction of about 3% [54]. GO sheets in composite provide a conductive path for the electron when the concentration of the conductive filler is above the percolation threshold. The conductivity performance of GO polymer composites is not only limited by the dispersion of nanosheets in matrix, but the attachment of the foreign molecules may change the charge transport properties. Macosko *et al*. compared the difference in electrical property of graphene/PU composites of carbon sheets exfoliated from GO via two different processes: chemical modification (isocyanate treated GO, iGO) and thermal exfoliation (thermally reduced GO, TRG), and three different methods of dispersion: solvent blending, in situ polymerization, and melt compounding [158], as indicated in Figure 2-14. Solution blending and in-situ polymerisation have better filler dispersion than melt blending and exhibit higher conductivity for the same volume. Strong interfacial bonding with matrix polymers enabled by surface functionalization is an advantage of iGO. However, inadequate chemical reduction processes may limit the electrical conductivity of the composite. Sometimes it is important to trade off the properties. Additionally, GO nanosheets are also used to improve the mechanical strength, thermal conductivity and gas barrier properties of composites [159, 160, 161]. GO and its composites with high doping content are conductors, at which point it is not meaningful to discuss their breakdown strength. For low doping content GO polymer composites the breakdown strength is usually considered to be similar to that of the pure polymer matrix, and therefore there are very little of the literature discussed the breakdown strength of these composites.

It is promising that autonomous capabilities including self-adaptive and self-healing functions can be organically integrated into the same dielectric utilizing GO and self-healing PU through appropriate material design and processing methods.

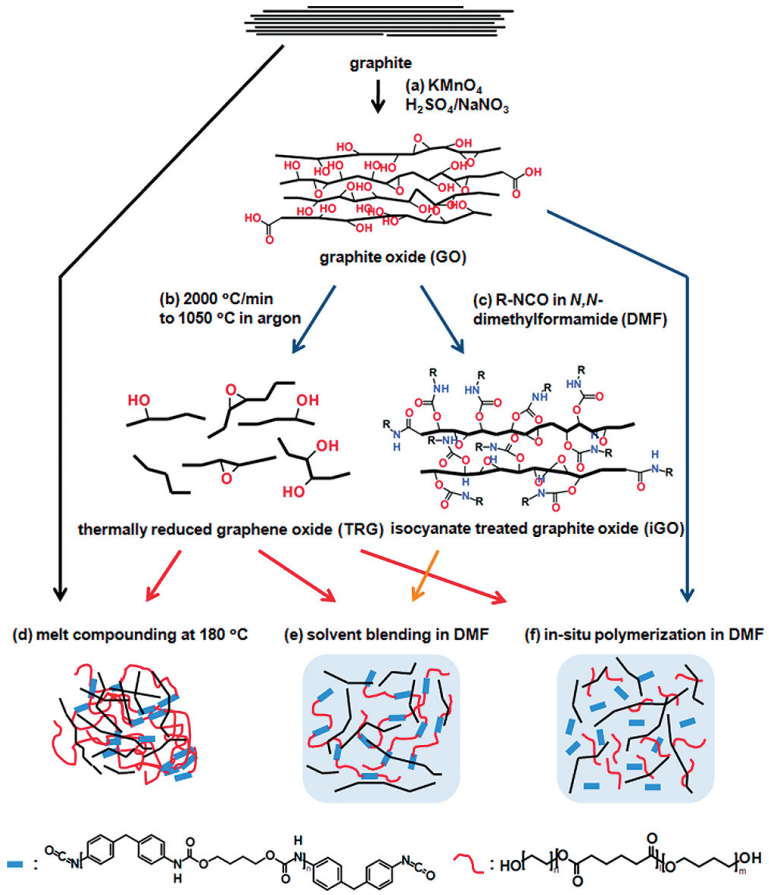

Figure 2-14 : Schematics of TPU/graphene composite preparation routes: (a) GO (b) Rapid thermal reduce (TRG) or (c) Organic modification with isocyanate in DMF (iGO); (d) Melt compounding; (e) Solvent blending; (f) In situ Polymerization [158].

2.8 Summary and Conclusions

This chapter reviewed the importance of smart dielectrics, including self-healing and self-adapting materials, for the next-generation electrical insulation and the relevant research progress.

Section 2.2 started with a review of the development of electrical insulation materials. From natural materials to single synthetic polymers up to the nanodielectrics, the innovation in insulation materials is undoubtedly an essential foundation for the evolution of electrical industry. In today's carbon-neutral vision, the construction of novel advanced power transmission networks is imminent, raising more stringent challenges to traditional dielectric materials. Bio-inspired smart materials such as self-healing and self-adaptive materials are an important way to build greener, more reliable, and longer-lasting electrical insulation systems. The basic synthesis strategies, extrinsic

and intrinsic, for self-healing polymer materials were introduced in section 2.3. The new challenges involved in introducing self-healing polymers into the field of electrical insulation were described in section 2.4. The mechanisms of formation and manifestations of electrical damage specific to HV insulating materials are presented, as well as a summary of research progress in self-healing dielectrics. A potential solution to the low dielectric strength of existing self-healing dielectrics may lie in the unique phase separation structure of PU elastomers (section 2.5). Methods of achieving an efficient and stable nonlinear electrical response, the construction of percolation pathways and interfacial barrier alignment, are clarified in section 2.6 by reviewing the mechanisms of self-healing dielectrics and their applications to HV insulation. At the same time, 2D GO nanosheets are a potential option for the organic integration of self-adaptive and self-healing functions due to their extremely low percolation threshold and abundance of surface reactive groups. Through a comprehensive review of the progress and shortcomings of existing research on self-healing and self-adapting dielectrics, PU elastomers and GO nanosheets were selected to enable the smart dielectric with simultaneous self-healing and self-adapting electrical and dielectric behaviours (section 2.7).

Chapter 3 Materials Preparation and Methodology

3.1 Introduction

Chapter 3 presents the general methodology used in this thesis. The design ideas, synthesis routes and sample preparation methods for PU elastomers are described in detail in Section 3.2. Multi-level, multi-perspective analytical approaches to the study of solid dielectric materials is presented in Section 3.3. The principles and operating procedures of a comprehensive research methodology are detailed, including quantum chemical simulations, chemical and physical structural characterisation, electrical, dielectric, mechanical and thermal properties.

3.2 Design and Preparation of PUs

The potential application of PU elastomers in high voltage insulation is attractive, but too little research has been carried out. This research will start with the preparation of materials and the design of a series of PU elastomers for investigating the relationship between their properties and structure.

The category of polyurethane discussed here is thermoplastic polyurethane (TPU), which has excellent elasticity and transparency. TPU is a phase separated polyurethane with alternating hard (HS) and soft (SS) segments, where the length of SS and HS can be controlled during the synthesis process for achieving a desirable property. As a result, TPU can be available in different states from flexible to rigid [162]. Here, TPUs with different phase separations obtained by adjusting the length and equivalent weight of the polyol used in synthesis were designed. TPUs were synthesized using two bifunctional polypropylene glycols (PPG) with different molecular weights, Arcol 1004 (MW=450, obtained from Covestro) and Lupranol 1100 (MW=1100, obtained from BASF), and 4,4’-methylene diphenyl diisocyanate (MDI, obtained from Covestro), and 1,4-butanediol (BDO, obtained from Sigma-Aldrich). The formulation of designed TPU is indicated in Table 3-1. Eq. 2.1 defines the percentage of mass in the hard segment as the

HS%, but it is worth noting that this is only a defined value and does not reflect the actual phase separation of the TPU. Figure 3-1 shows the molecular structure of all raw materials.

Table 3-1: Formulation of designed TPUs

Sample Code	Molecular Weight of PPG	Isocyanate	Chain Extender	Molar Ratio (Isocyanate: PPG: Chain Extender)	wt% of Hard Segment
PU1	450	MDI	-	2.1: 2.1: 0	-
PU2	450	MDI	BDO	2.1: 2: 0.1	35%
PU3	450	MDI	BDO	2.2: 1: 1.2	55%
PU4	1100	MDI	BDO	2.2: 1: 1.2	35%

$$\textbf{wt\% of hard segment} = \frac{weight_{\mathrm{BDO}} + weight_{\mathrm{MDI}}}{weight_{\mathrm{BDO}} + weight_{\mathrm{PPG}} + weight_{\mathrm{MDI}}} \times 100\% \quad (weight_{\mathrm{BDO}} \neq 0) \quad (3.1)$$

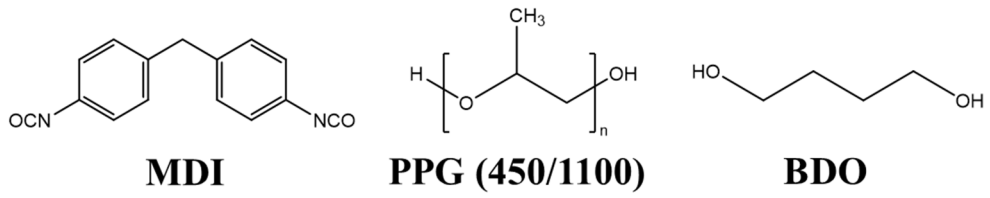

Figure 3-1: Molecular structure of raw materials.

TPU's basic reaction is the formation of the urethane group from the hydroxyl group with the isocyanate group under inert gas at 70 ℃, as shown in Figure 3-2 (a). The PPG oligomers and BDO were dried and degassed under vacuum in a flask at 70 ℃ for 24 hours before use. All PUs were prepared by a typical two-step polymerization in a four-necked round bottom flask equipped with an anchor type propeller stirrer, funnel, and nitrogen inlet, as exhibited in Figure 3-2 (b). In the first step, pre-polymerization, an NCO-terminated prepolymer was prepared by carefully adding MDI to the flask containing the appropriate dried PPG at 70 ℃, while keeping the rotational speed at 400 rpm for 2 hours. In the second step, the reaction was initiated by dripping BDO into the flask for 2 hours. The reaction is carried out under a nitrogen atmosphere throughout. The solution was then cast into a silicone mould and the solvent evaporated at 70 °C for

24 hours to obtain block materials that can be used for further processing. Dimethylformamide (DMF, anhydrous, obtained from Sigma-Aldrich) was used as the solvent to aid with viscosity regulation in the two-step process. For all samples, the ratio of isocyanate groups to total hydroxyl groups, r=[NCO]/[OH], was kept at unity to obtain fully end-linked linear chains. Meanwhile, samples with different hard segment ratios were obtained by controlling the amount of chain extenders.

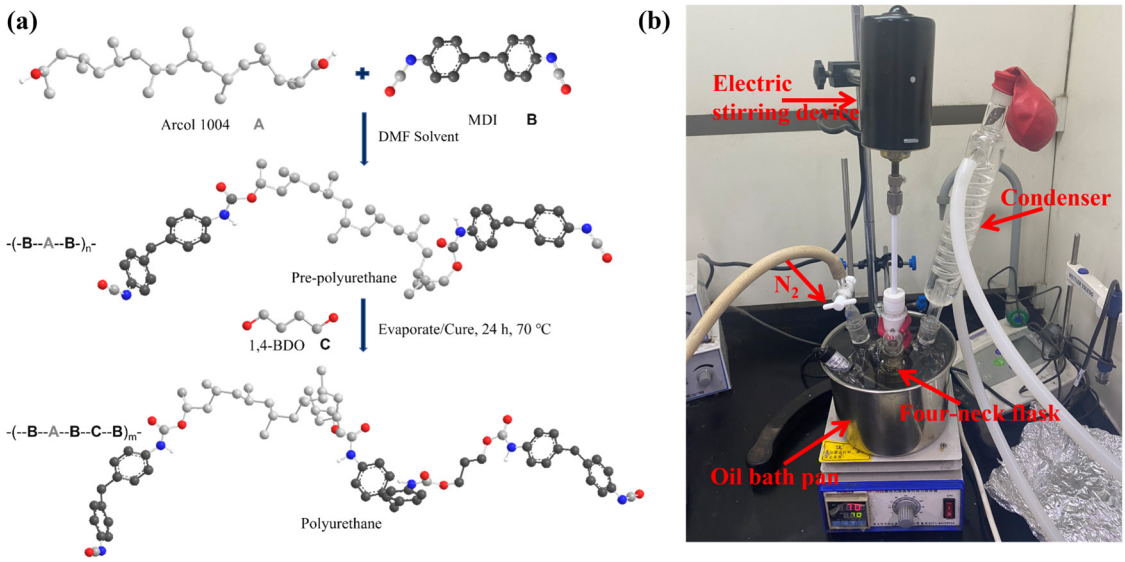

Figure 3-2: Synthesis method (a) and platform (b) of TPU.

Film PU samples with uniform thickness are essential to be suitable for the various subsequent tests. After synthesising the block PU samples, the bubble-free portion of the PU samples are cut off and further prepared by hot pressing method to form film samples that can be used for various types of tests. Parts of block PU samples were hot pressed through a plate vulcanizer (Yitong Test Technology) at 160 °C and 15 MPa for 10 min, and then cooled with water at 10 MPa for 5 min to room temperature. Even if there is a small amount of air bubbles in a selected block sample, the air bubbles can be removed by applying pressure in the molten state of samples, resulting in a bubble-free, flat film sample. The thickness of the film samples produced were 100 μm, 200 μm, 500 μm, 1 cm, and 2 cm, as shown in Figure 3-3, by using different moulds.

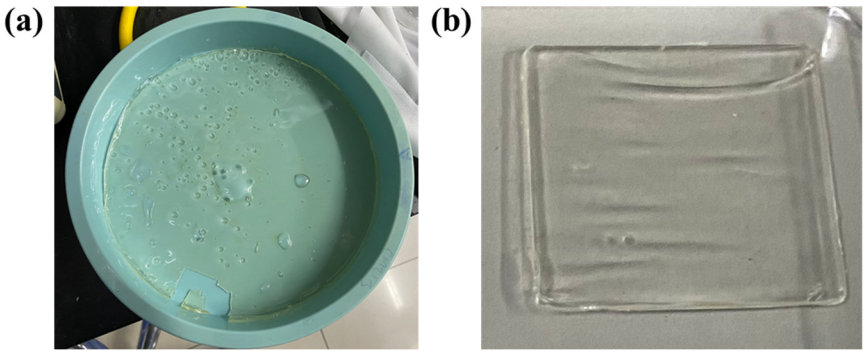

Figure 3-3: TPU block sample (a) and film sample (b).

3.3 Characterization Methods

The following simulation and experimental methods were extensively used in this study to provide a comprehensive understanding of polyurethane materials.

3.3.1 Quantum Chemical Calculations

The basic principle of quantum chemical calculations is quantum mechanics, which takes the electron as the most basic unit and theoretically calculates the HOMO-LUMO orbitals, orbital energy levels, electrostatic potentials, and other microscopic parameters of the dielectric, to study the energy band structure and trap distribution and other related parameters of the dielectric. The theoretical basis for quantum chemical calculations is the Schrödinger equation, which can be solved to obtain the state of electronic motion within the molecule. Quantum chemical calculation methods include Ab initio method, semi-empirical method, and density functional theory. The concept of density functional theory (DFT) originated from the Tomas-Fermi model and was developed on the basis of the Hohenberg-Kohn theorem, which, like the ab initio method, is based on Hartree Fock's principle and allows predictions to be made for microscopic systems. It describes the system in terms of the electron density distribution function rather than the wave function, which is a huge simplification for multi-electron systems, and because of the time saving and efficiency, density functional theory is more widely used. Considering the calculation speed and accuracy, the level of the basis set is given as 6-31g(d); the exchange-correlation general function is set as b3lyp, which adopts Becke's three-parameter hybridisation method and Lee, Yang and Parr correlation general functions. After the optimisation, the HOMO-LUMO orbitals, orbital energy levels, and

electrostatic potentials of the molecules can be analysed. An initial repeating unit of PU2 segments (Figure 3-4) was constructed in DFT model, where SS fragments composed of PPG (MW=400) and MDI, and HS fragments composed of BDO and MDI assemble the PU segment. The calculation is based on the quantum chemical software Gaussian 09 (Gaussian, Inc.) [163].

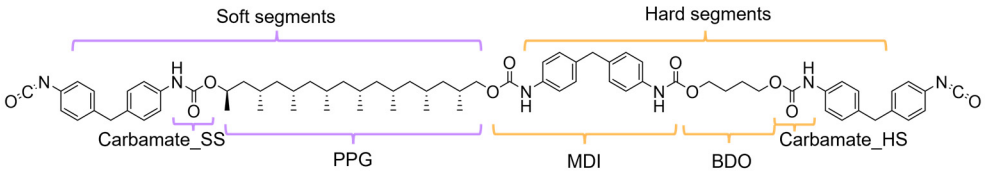

Figure 3-4: Theoretical modelling molecular structure of PU's repeating unit.

3.3.2 FTIR

Fourier-transform infrared spectrometer (FTIR, Thermo Fisher Nicolet iS10, USA) was used to characterize the chemical composition of PUs between 800 and 4000 cm^{-1} with a resolution of 4 cm^{-1}. Additionally, a small-scale *in situ* FTIR between 1640 and 1780 cm^{-1} was used to scan the state of hydrogen bonding network of PU samples at different temperature points.

3.3.3 GPC

Gel permeation chromatography (GPC, Agilent 1260, USA) is a type of size exclusion chromatography (SEC). It is mainly used to measure the molecular weight of polymer compounds. The molecular weight distribution shows how much molecular weight contains in a sample, and it is widely used for quality control to know the difference in the properties of polymer compounds. THF was selected as the solvent for GPC mobile phase. PU samples were dissolved in THF solvent. The polymer solution flowed through a column containing different pore size with a mobile phase flow rate of 1.0 mL/min.

3.3.4 AFM

Atomic Force Microscopy (AFM) is a technique that scans a small area of a sample at the micron level through a probe with a nanometre radius of curvature at the tip. Small interactions between the sample and the probe cause the probe to bend, and further progressive magnification, capturing and recording of such small changes allows the

interaction of the probe with the sample to be calculated, thus helping to analyse the properties of the sample [164, 165]. Microphase separation topography of PUs was investigated with AFM (Bruker Dimension Icon) by peaking force tapping mode, where the probe was ScanAsyst-Air with a radius of curvature of 5 nm.

There are two ways to fabricate ultra-thin film samples for AFM testing, spin coating and drop coating. Spin coating involves applying drops of sample solution to a substrate then rotating the substrate at high speed on a horizontal turntable, throwing off and evaporating the excess solvent to form an ultra-thin film [166]. Drop coating is the application of drops of the sample solution onto the substrate, followed by evaporation of the solvent at high temperatures to obtain a thin film. The thickness of the film obtained by spin coating is much smaller than that obtained by drip coating when the same concentration of solution is applied. In this case, a PU/DMF solution with a concentration of 30 mg/ml was obtained by dissolving the PU block sample prepared in the previous section in DMF. To remove any residual contaminants and undissolved polymer particles from the solution, the solution is completely filtered through a PTFE injection filter (200 nm pore size) prior to use. The solution was heated to 70 °C, dropped onto 60 °C preheated silicon wafers (Sibranch Microelectronics) and spin coated (Setcas KW4E) at 3000 rpm for 30 seconds to obtain approximately 100 nm PU films. Another batch of samples was obtained by pipetting 50 μL of PU/DMF solution onto silicon wafers and evaporation of the solvent at 70 °C for 24 hours. Both batches were then quenched to maintain the same thermal history as the hot-pressed samples by heating to 160 °C followed by rapid cooling to room temperature.

Figure 3-5 presents the image and AFM height image of (a) spin coating PU2 sample and (b) drop coating PU2 sample. Apparently, the spin-coating samples have a more homogeneous surface morphology with the mixed phase filling the surface, whereas in the drop-coated samples a clear structure of separated phases is visible. The reason for this phenomenon is that the phase separation of polyurethane is stem from the thermodynamic incompatibility between its SS and HS. However, the high quenching rate of the solution during spin coating prevented the phase separation from being completed [167, 168]. Another reason is that because the spin-coated sample is much thinner than the drop-coated sample, the forces between the film and the silicon substrate

are much stronger, preventing the formation of the phase separation structure during the quenching process. Therefore, drop coating PU samples were employed in subsequent experiments to measure the surface topography.

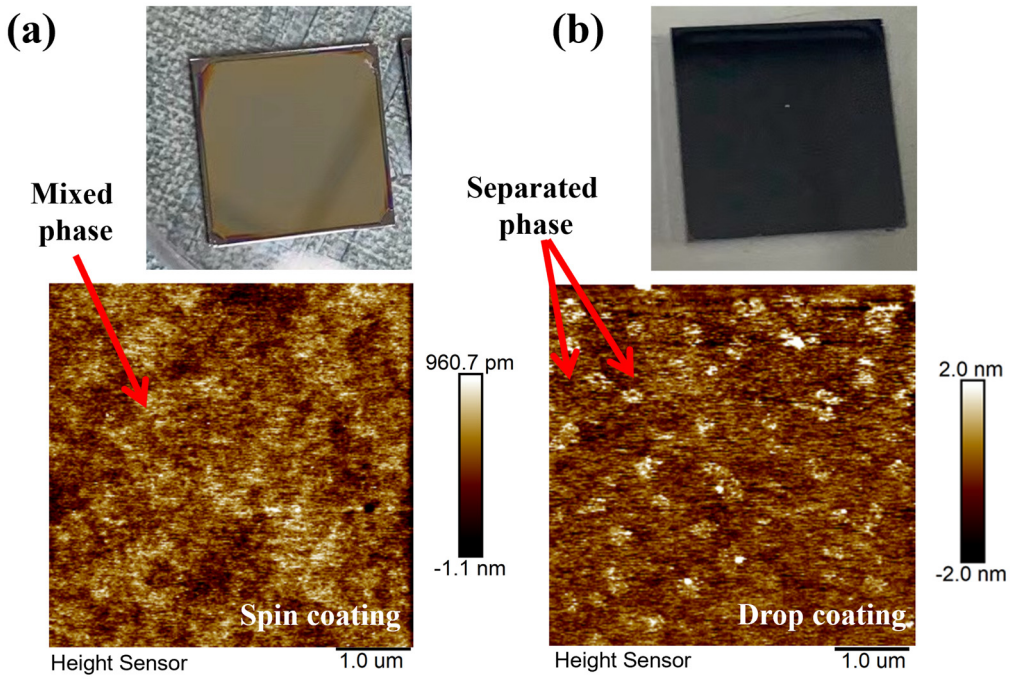

Figure 3-5: Image and AFM height image of (a) spin coating sample, (b) drop coating sample.

3.3.5 DSC

The thermal properties of the PUs were determined by differential scanning calorimetry (DSC, TA Instruments Q2000, USA). Samples for DSC tests were prepared by cutting 5 mg of prepared PUs in hermetically sealed aluminium pans. All samples were allowed to attain isothermal equilibrium at 30 ℃ for 10 min then heated to 150 ℃ to erase the thermal history of prepared samples before collecting data. The response was measured in nitrogen at a heating/cooling rate of 5 ℃/min through cooling to -50 ℃ and heating back to 200 ℃.

3.3.6 DMA

A single dynamic mechanical analysis (DMA) experiment allows us to quantify the shape memory effect in terms of stored and released energy densities and their relationship with the shape memory efficiency [89]. The tests were performed for tensile

tests (Q800 TA Instrument) of PU samples at a heating rate of 2 ℃/min from -50 ℃ to 100 ℃ based on the strain sweep method.

3.3.7 DC Conductivity

DC volume conductivity was measured with a digital high-resolution electrometer (Keithley 2635B, USA) equipped with standard three-electrode system according to standard IEC 60093, where the diameter of the measuring electrode is 2 cm. The measurement system is indicated in Figure 3-6. The measurements were performed on the samples with a thickness of 500 μm and with 1-15 kV/mm DC electric field applied. The steps of electric field for each set of measurements was 1 kV/mm. The measurement time at each voltage level was 30 min to obtain the steady-state DC conduction current. The charging current for 30 min at each voltage level is close to steady state, as shown in figure 3-7. The sampling frequency of the electrometer was set to 1 data point per second. Hence, each point on the I-E curve is obtained as the average of the data collected during the final 10 min. Although we used the same sample to test the conduction current at different applied voltage levels, we will release the residual charge by grounding the sample after each charging tests for 30 min. Based on this operation, we can confirm that the I-E curve was not affected by the residual charge in every individual charging test. The testing temperature was controlled at 25 ℃ by a thermostatic oven. This procedure was repeated for different samples to obtain consistent data. No significant difference was found between the primary and repeated experiments.

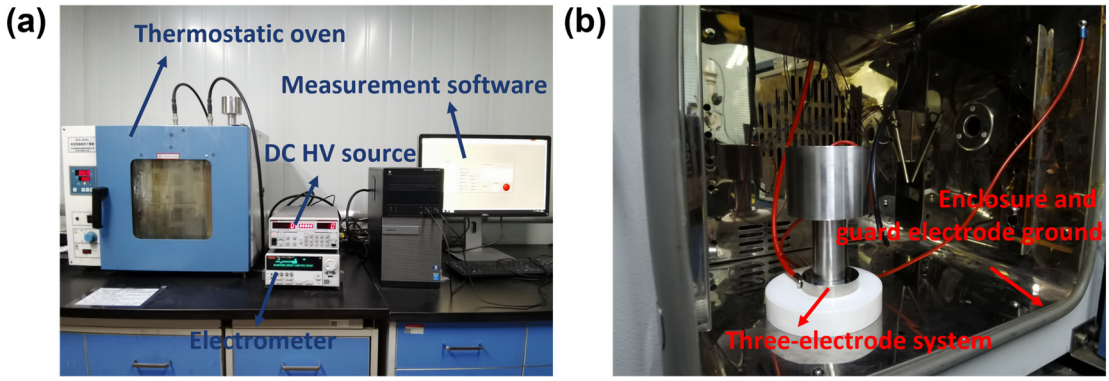

Figure 3-6: (a) DC conductivity measuring system. (b) Three-electrode system.

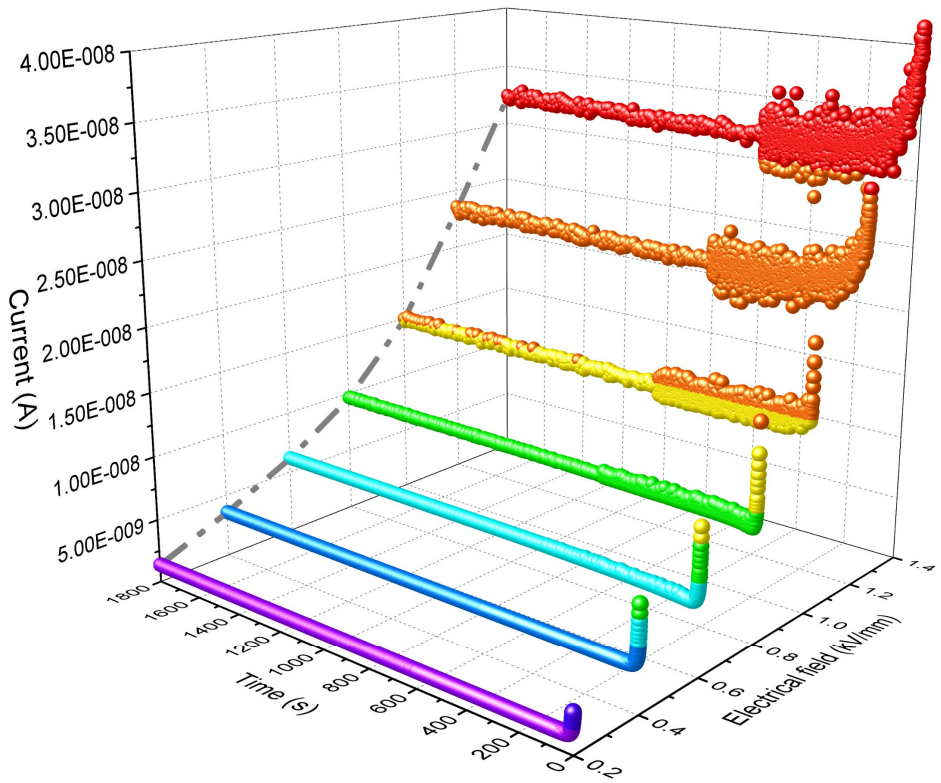

Figure 3-7 Conduction current of PUs over time.

3.3.8 DC Breakdown

DC electric breakdown tests were performed using a dielectric strength tester (HT-50, Guilin Electrical Equipment Scientific Research Institute, China) on film samples with a thickness of around 500 μm at 23 ℃, as shown in Figure 3-8. The samples were sandwiched between two 10 mm ball electrodes and immersed in silicone oil to prevent surface flashover. A ramp-voltage, increased at the rate of 1 kV/s was applied across each of the samples until dielectric breakdown was achieved. For each sample, 10 different points were tested, and the test data were processed using two-parameter Weibull statistical distribution according to IEEE Std 930-2004.

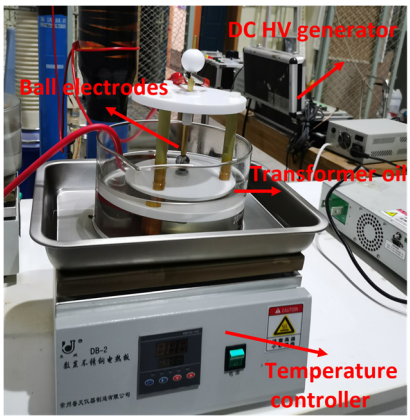

Figure 3-8: DC electric breakdown testing system.

3.3.9 Dielectric Relaxation Spectroscopy (DRS)

Broadband dielectric spectroscopy (BDS), with its ability to apply an alternating electric field to a sample over a wide frequency range and to study the corresponding molecular relaxation processes, is the most commonly used method to study molecular motion in the field of dielectrics [169]. A Novocontrol Alpha-A high-performance frequency analyzer (GmbH, Germany) equipped with a Quatro-Cryosystem temperature control system was utilized to measure the broad band dielectric relaxation spectroscopy of PU samples. All the measurements were carried out in the frequency range 1^{-1} to 10^{6} Hz under a 1.0 V alternating-current voltage, while temperature ranging from -100 ℃ to 75 ℃ were applied at 25 ℃ intervals. A gold layer was evaporated onto both surfaces of the sample to serve as electrodes. The thickness of the measured sample is 500 μm and the diameter of the measuring electrode is 2 cm.

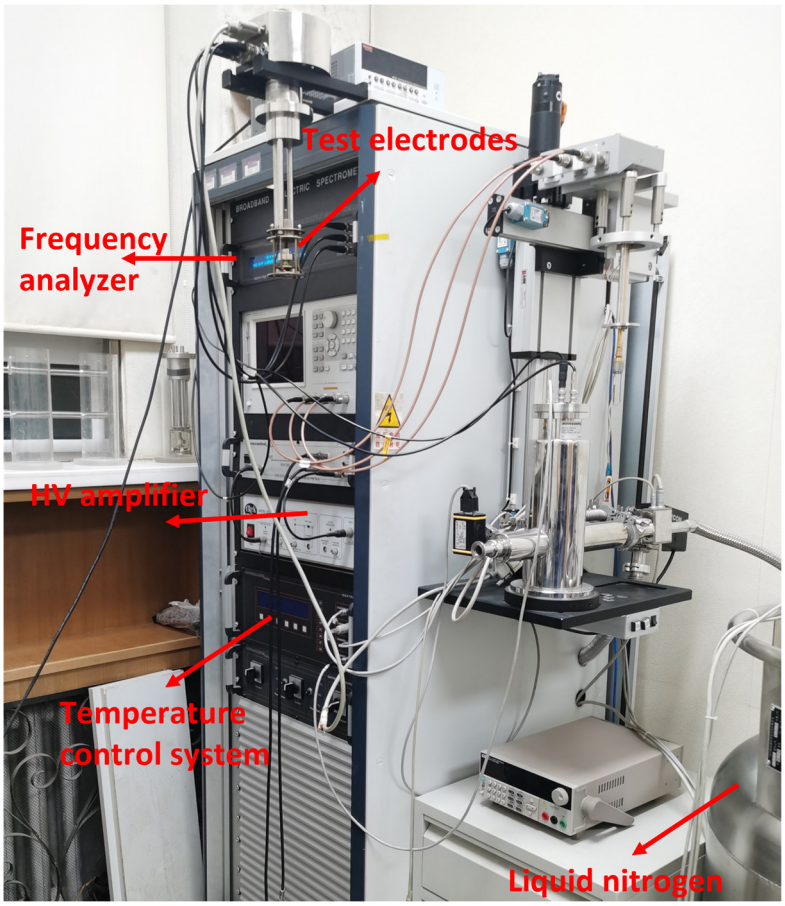

Figure 3-9: BDS measuring system.

3.3.10 TSDC

Thermally Stimulated Currents (TSC) measurements can use thermal stimulation to determine the activation energies associated with the movement of charge carriers in a dielectric, and the obtained thermal stimulation current peaks reflect the charge transport behaviour of the dielectric [170]. Samples with a thickness of 500 μm was polarized under 1.5 kV/mm at 25 ℃ for 30 min, then cooled to -50 ℃ at a rate of 10 K/min, and then heated to 60 ℃ at a rate of 5 K/min. During the heating process, the depolarization current of the material was measured by electrometer (Keithley 6517b). The precise control of the temperature is in line with the Quatro-Cryosystem temperature control system.

During the heating measurement process, frozen charges in the material are excited to form depolarization currents at different temperatures according to their different activation energy [171]. Either the rotation of dipoles, the migration or recombination of

ions, the trapping or separation of space charges can be covered as depolarization processes. In order to obtain corresponding microscopic parameters of materials during the depolarization process, TSDC current density can be described by the first order kinetic equation [172]:

$$J(t) = -\frac{dn}{dt} = (\frac{n}{n_0})^c s n_0 \exp(-\frac{E_t}{kT}) \tag{3.2}$$

Where n is charge density (nC/cm^2), s is escape frequency (Hz) that is defined as the number of times per second that the electrons escaped from traps, n_0 is initial charge density, E_t (eV) is activation energy level, k is Boltzmann's constant, T (K) is absolute temperature, c is a number describing the kinetic order and can theoretically take values between 0.5 to 3.

Furthermore, the equation is expanded to [172]:

$$\begin{aligned} J(t)_{c=1} &= s n_0 \exp(-\frac{E_t}{kT}) \exp(-\frac{s}{\beta}\int_{T_0}^{T} e^{-\frac{E_t}{kT'}} dT') \\ J(t)_{c\neq 1} &= -\frac{dn}{dt} = (\frac{n}{n_0})^c [1+(c-1)]\frac{s}{\beta}[\int_{T_0}^{T} e^{-\frac{E_t}{kT'}} dT']^{\frac{c}{1-c}} \end{aligned} \tag{3.3}$$

β is the rate of heating and increases linearly with time.

Setting the derivative of function (d$J(t)$/dt) to zero will allow to obtain the extreme of this function:

$$\begin{aligned} &\frac{\beta E_t}{kT_m^{\,2}} = s e^{-\frac{E_t}{kT}} && (c=1) \\ &1+\frac{(c-1)s}{\beta}\int_{T_0}^{T} e^{-\frac{E_t}{kT'}} dT' = \frac{cskT_m^{\,2}}{\beta E_t} e^{-\frac{E_t}{kT}} && (c\neq 1) \end{aligned} \tag{3.4}$$

Activation energy E_t and charge density n for each relaxation peak can be calculated based on taking three points on the TSDC curve, (T_1, J_1), (T_2, J_2), (T_3, J_3) [172]:

$$E_t = \frac{k[\ln(\frac{J_3}{J_1})\ln(\frac{n_2}{n_1}) - \ln(\frac{J_2}{J_1})\ln(\frac{n_3}{n_1})]}{(\frac{1}{T_2} - \frac{1}{T_1})\ln(\frac{n_3}{n_1}) - (\frac{1}{T_3} - \frac{1}{T_1})\ln(\frac{n_2}{n_1})} \quad (3.5)$$

$$n = \frac{1}{\beta}\int_{T}^{T_\infty} J(T')dT'$$

3.3.11 Tensile Tests

The tensile tester (Instron 3343) was used to test the mechanical properties of PU samples according to ASTM D882-18. The 1 mm thick specimen was cut into dumbbell shaped strips with 12 mm long and 2 mm wide in the test area. The test temperature was 25 °C and the strips were stretched at a rate of 20 mm/min. Each type of material 5 samples were tested, and the average value was recorded. The equation of stress (σ, MPa) and strain (ε, %) is:

$$\sigma = \frac{F}{b \times d}$$
$$\varepsilon = \frac{l - l_0}{l_0} \times 100\% \quad (3.6)$$

Where b is the wide (mm), d is the thickness (mm), l is the length when tensioning (mm), and the l_0 is the initial length of sample (mm).

3.3.12 Electric Tree Observation Methods

An optical microscope (Nikon DS-Ri2) connected to a computer was used to display real-time images of the growth or healing process of electric trees in transparent samples for qualitative evaluation of the size and extent of dendritic channels. The 3D topographic features of the electrical tree channel before and after healing were measured using a 3D X-ray micro-CT (3D-CT, Xradia micro-XCT-500, Carl Zeiss XRM, Germany) to complement those details missed by the 2D images as well as for a quantitative analysis of channel healing efficiency. Samples were mounted on the holder with an aluminium tube as the adapter and rotated horizontally, pausing at discrete angles to collect 2D projection images, which were then combined to produce a 3D reconstruction of the sample's volume dataset. Scanning electron microscopy (SEM) can

also be used to observe the state of repair of electrical tree channels. However, SEM is a destructive testing method as it requires the sample to be embrittled under liquid nitrogen to obtain a cross-section that can be used for observation. As a result, SEM is usually only used as an auxiliary observation tool to determine if electrical tree channels have been refilled.

3.3.13 Partial Discharge

Partial discharge (PD) testing is widely used to examine the reliability of insulated equipment and to determine defects or air gaps within the equipment. PD in polymers is thought to be a major origin of electrical damage, and the size of the dendritic damage is positively correlated with the maximum apparent discharge magnitude (Q_m) [18]. A multi-channel digital partial discharge (PD) analyzer (TWPD-2E, Baoding Tianwei, China) was used to detect the maximum apparent discharge amplitude (Qm) under an applied voltage of 3 kV at different stages of tree formation and healing to characterize the degree of electrical aging. The same sample will be used for PD testing at different stages of ageing or healing, which is intended to provide a more intuitive comparison of the electrical properties of the same sample before and after electrical damage repair. PD tests were carried out at six different stages, initial state, ageing for 15 min, ageing for 30 min, stopping ageing, self-healing for 24 h, self-healing for 48 h. The same sample was tested at each stage of the PD for 1 min and 10 data points of were measured. The discharge amplitude was obtained by averaging the 10 data points measured. The PD test utilises the same electrode structure as in the electrical tree initiation test to ensure that each PD measurement point corresponds to the observed state of the visualised electrical tree. At the same time, the PD test is performed at a voltage of only 3 kV/ 50 Hz and the test time is short. It is therefore considered a non-destructive test and does not further extend the electrical damage of the sample in every PD test.

3.4 Summary

The PU materials prepared, and the general methodology of this research were presented in this chapter. In section 3.2, four PU materials with different degrees of phase separation were developed by adjusting the molecular length and equivalent weight of the polyol in the synthesis process. PU film samples with certain thickness were obtained

by hot pressing, ready for further various tests. Multi-level, multi-perspective analytical approaches have been employed in this research, including quantum chemical calculations based on density functional theory, FTIR for chemical composition analysis, GPC tests, AFM for characterisation of surface topography, conductivity and breakdown, DRS and TSDC for description of electrical and dielectric behaviour, and DSC and tensile testing for evaluation of thermal and mechanical properties of PUs. Notably, the methods outlined in this chapter are the general methods used in this research, with some more specific and unique methods detailed in the relevant chapters.

Chapter 4 Structure-Activity Relationship of Microphase-Separated PU Elastomer

4.1 Introduction

Chapter 4 investigates the comprehensive properties of PUs for its potential application in HV insulation. FTIR spectrometer and AFM are firstly used to analyse the chemical composition and microphase separating structure of PU samples indicated in section 4.2 and 4.3, respectively. Section 4.4 then shows the macro electrical properties of PUs with different phase separated structure. Two perspectives, TSDC and variable temperature DRS, are used to reveal the relaxation behaviour of PUs, and the corresponding microscopic parameters are calculated in section 4.5. Section 4.6 illustrates the structure-activity relationships between the microscopic phase-separated structure of PUs and their macroscopic electrical properties by combining quantum chemical simulations with experimental data. The thermal and mechanical performance of the materials are supplemented in section 4.7. Understanding the interrelationship between the structure and properties of polyurethane helps to instruct the design and preparation of ideal polyurethane materials.

4.2 Chemical Composition

The chemical composition of PU samples is revealed in FTIR spectra, Figure 4-1. After curing, the -NCO absorbance peak around 2280 cm^{-1} disappears, which confirmed that the synthesis reaction of PUs was completed. Hydrogen bonding between the secondary amine group (-NH) and the carbonyl group (C=O) is the intrinsic driving force for the phase separation of PUs, which is important for the self-healing performance [173]. The hydrogen bonding interaction makes the carbonyl bond length elongated and results in the reduction of the stretching vibration frequency [174]. Hence, mathematical deconvolution of the carbonyl stretch peak around 1740 cm^{-1} can be used to divide the free and hydrogen carbonyl, while the stretching peak at lower wavenumber belongs to H-bonding carbonyl [168]. As shown in the partially enlarged drawing of Figure 4-1, a hydrogen-bonded carbonyl stretching peak is found at 1705 cm^{-1}, which proved the

structure of hydrogen bond crosslinking between different chain segments of PU samples. The addition of chain extender will not significantly affect the content of H-bonding carbonyl of PUs, when using the same formulation of PPG and MDI. Even if there are no so-called HS in PU1, hydrogen bonds might still be formed between non-adjacent -NH and C=O groups in SS. The hydrogen bond crosslinking degree of PUs increases with the raising of HS content, where the H-bonding C=O content increased from 73.9% of PU2 to 83.8% of PU3. Yet, a longer molecular chain of PPG will lead to a lower degree of hydrogen bond crosslinking of PUs with the same HS content.

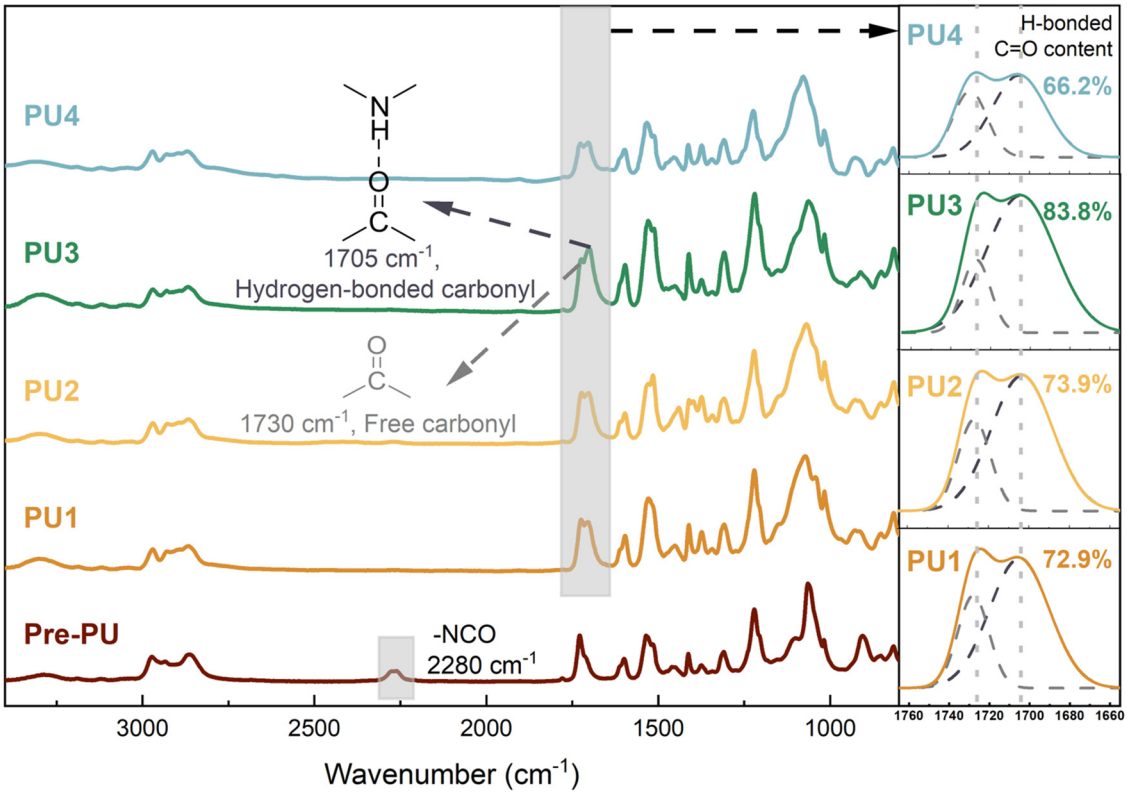

Figure 4-1: FTIR spectra of PU samples and the deconvolution peaks of C=O regions.

Number average molecular weight (M_n) and weight average molecular weight (M_w) of designed PUs are shown in Figure 4-2 and Table 4-1, separately. Mn and Mw are two common parameters to describe the molecular weight of polymers. Number average molecular weight is averaged the molecular number in polymer. Weight average molecular weight is averaged by the molecular weight. The abscissa is the molecular weight, and the ordinate reflects the amount of substance. The M_n and M_w of the synthesized PUs increases with the increase of the HS content. The results are in accord with expectations, since the utilization of more chain extenders means that more

repeating urethane units are incorporated into the PU backbone, while keeping the same isocyanate index constant.

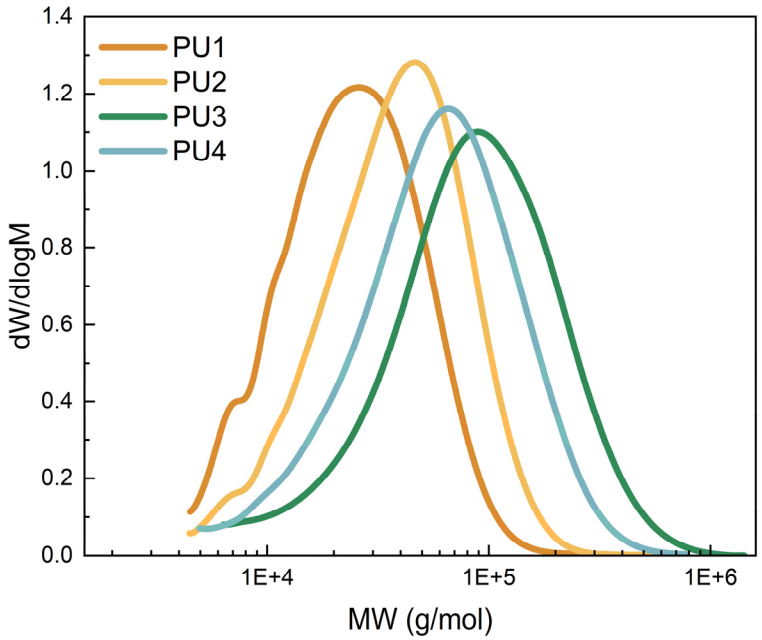

Figure 4-2: Molecular weight distribution of different PU samples.

Table 4-1: Number average molecular weight (Mn) and weight average molecular weight (Mw) of designed PUs.

Sample	Mn (g/mol)	Mw (g/mol)
PU1	18689	30292
PU2	27815	47498
PU3	55251	118700
PU4	39493	79109

4.3 Micro-topography

AFM has been widely used to investigate the nanoscale morphology of microphase domain in PUs [164, 167]. The height images of PU1, PU2, PU3, and PU4 as obtained by AFM are presented in Figure 4-3 (a), (b), (c), (d), separately. The bright speckles in these images, the "bumps" of the surface, are generally considered as a key feature formed by the orderly stacking and higher modulus of the HS regions [175]. The corresponding modulus mapping of PU3 with the largest bright region in the height image is also measured at the same position, as shown in Figure 4-3 (e). There is a very high consistency between the bright speckles in the height image and the high modulus area in the modulus mapping. Hence, the "bumps" in the height graph can be identified

as aggregating domains of HS. Although the defined HS% (wt% of hard segments) is shown in Table 3-1, only isocyanates that react with chain extenders can form so-called HS. A revised HS% is given by multiplying the defined HS% by the percentage of the number of moles of the chain extender to that of all polyols in the synthesis. Additionally, the region with height above 1 nm in AFM image is allocated to HS domain and the actual HS% is defined as the area percentage of HS, as presented in Figure 4-3 (f). The actual HS% is very close to the revised HS%. The actual HS% of PU1 is 0, due to the absence of chain extender. Comparing the AFM images of PU2 and PU3, the hard phase transforms from the dotted distribution of PU2 to the large area of banded distribution of PU3 in the continuous distributed soft phase, while the actual HS% also increased from 2.9% to 25.8%. The actual HS% of PU4 is 20.7%, and its HS domain is significantly increased, but the hard phase has not aggregated to form a banded distribution.

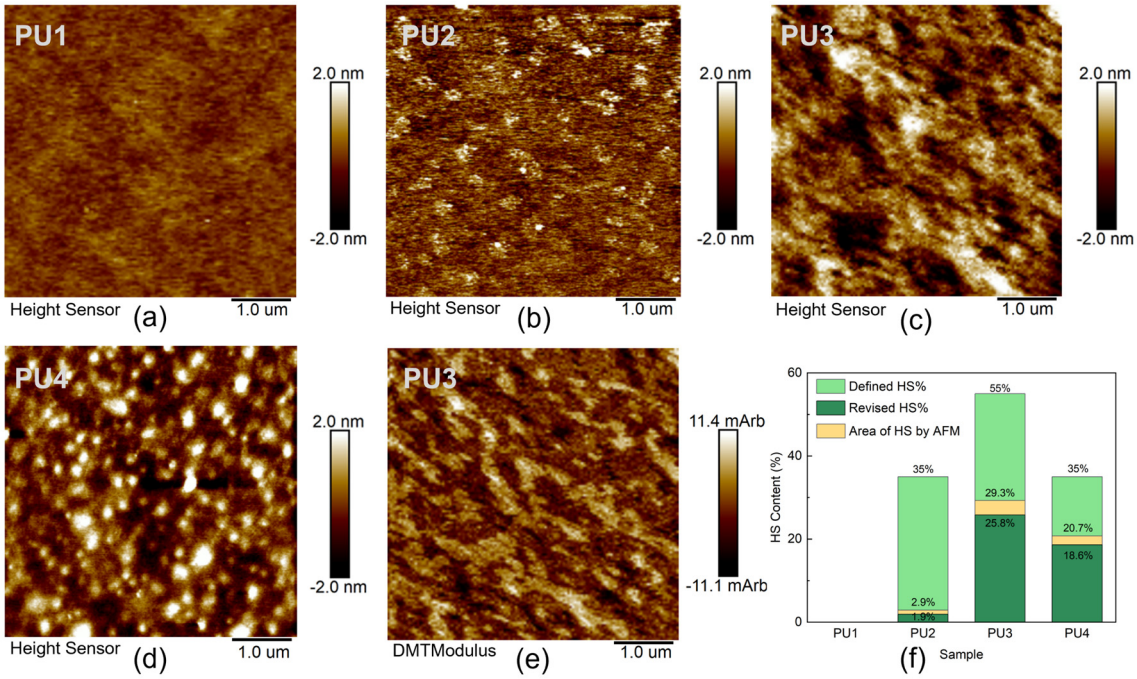

Figure 4-3: Height image of (a) PU1, (b) PU2, (c) PU3, (d) PU4, and corresponding DMT modulus map of (e) PU3 as obtained by AFM. (f) HS contents of PU samples as obtained by different calculating approaches.

4.4 Electrical Behaviours

DC conductivity properties and DC breakdown strength are two significant parameters for evaluating the electrical property of dielectric polymers. For a more intuitive comparison, the electrical performance of a common engineering dielectric elastomer (Silicone rubber, Si-R, Wacker R230) was also tested. In the DC conductivity test,

three samples of each sample's type were tested (section 3.3.7). The statistical results of the conductivity including average and standard deviation are presented in

Table 4-2. Comparing the conductivity results of PU1-PU3, as shown in Figure 4-4 (a), the HS% is the critical factor limiting the conductivity of PUs, which decreases as the HS% increases, when the same PPG and MDI are used. It is noticeable that the presence of longer SS significantly lifts the conductivity of PUs. The conductivity of PU4 is two orders of magnitude higher than that of PU2, at the same defined HS%. Although the conductivity of Si-R is lower than that of PUs, the opposite results appear in the DC breakdown tests, as shown in Figure 4-4 (b). The characteristic breakdown strength is defined in terms of the alpha parameter of the Weibull distribution in the field at which 63.2%. The shape parameters of the measured samples were all greater than 10, the data were considered reliable (as shown in

Table 4-2). The characteristic breakdown strength of Si-R is 78.19 kV/mm, which is higher than that of PU1 at 32.72 kV/mm. The absence of the HS constructed from isocyanate and short-chain diols results in a much lower breakdown strength of PU1 than other PUs. The dielectric strength of PUs with microphase separating structure is much higher than that of Si-R, in which PU2 is 140.60 kV/mm, and PU3 is 311.64 kV/mm. Dielectric breakdown is a complex process affected by the coupling of electronic avalanches, thermal effects and mechanical effects [176]. It is believed that the reason for lower breakdown field for PU4 is the energy barrier between the SS and HS of phase separated PUs. PU elastomers composed of shorter polyol chains and a higher content of HS achieve lower electrical conductivity and higher breakdown strength. The underlying reasons for this phenomenon will be further investigated in the next section.

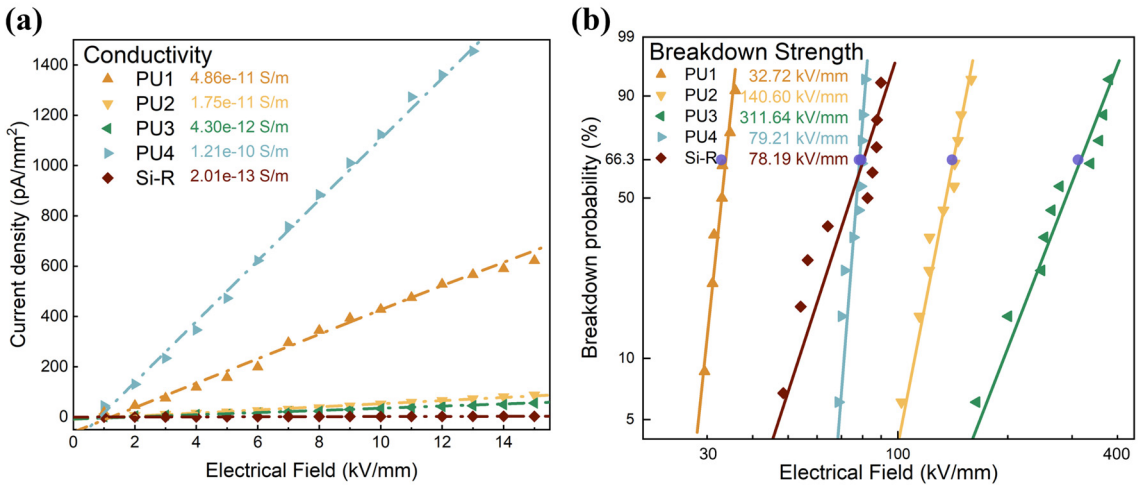

Figure 4-4: (a) DC conductivity properties of designed PUs. (b) Weibull characteristic DC breakdown strength of designed PUs.

Table 4-2: Statistical results of DC conductivity and breakdown strength of designed PUs

Sample code	Conductivity (S/m)		Breakdown strength (kV/mm)	
	Average value	Standard deviation	Characteristic value	Shape parameter
PU1	4.86e-11	2.91e-12	37.72	17.75
PU2	1.75e-11	1.96e-12	140.60	14.54
PU3	4.30e-12	2.58e-13	311.64	12.83
PU4	1.21e-10	1.13e-11	79.21	15.73
Si-R	2.01e-13	2.67e-14	78.19	23.87

4.5 Dielectric Behaviours

The dielectric relaxation behaviours of the PUs were revealed from the TSDC results and the DRS at different temperatures, bridging the microstructure of PUs to their macroscopic electrical properties.

4.5.1 DRS Results

Broad-band dielectric relaxation spectroscopy with temperature variation is not only an effective method for characterising the dielectric properties of materials, but also a powerful tool for the study of polymer chain dynamics [177, 178]. Figure 4-5 and Figure 4-6 show the temperature and frequency dependence on the relative permittivity and dielectric loss tangent (tan δ) for designed PU samples, separately. For all PUs, the spectra are complicated presenting processes of different natures, dipole, and conductive, in some cases closely superimposed. At temperatures below glass transition temperature (T_g, Figure 4-11), the dielectric constant exhibits values with about 3.5 that vary only slightly with frequency. The contribution comes from the electronic polarization of small groups induced by the electric field. As the PU main molecular chains unfreeze, the permittivity rises rapidly to around 10, with different transition temperatures due to the different T_g of the designed PUs. Finally, the strong increase in the dielectric constant values for temperatures above 50°C is associated with the presence accumulation of charges at the electrode-sample interface [179].

There are two obvious relaxation processes, α transition and β transition, indicated in the loss factor spectra, as shown around the arrow regions in Figure 4-6. The β transition, a secondary relaxation caused by localised vitrification motions, occurs in the low temperature, high frequency region. In previous studies, this has typically been attributed to side groups on the aliphatic backbone of the PU, such as free carbonyl groups [106, 180]. The plotted Arrhenius curve (Figure 4-7) confirms that the activation energy of β relaxation is consistent across the different PU samples, which is due to the fact that these PUs are all composed of the same polypropylene hydrocarbon structure and that differences in phase separation do not have an effect on this secondary relaxation. At higher temperature, the increase of the dielectric loss is associated with the glass transition, α relaxation, of the PUs. The increase in HS limits the α relaxation of PU3, as opposed to the more flexible SS molecular chain of PU4, which has a lower activation energy for α-relaxation. Interestingly, PU2 and PU1 exhibit the same α and β relaxation behaviour, probably as a result of their same PPG and MDI formulation. In theory, the only difference between PU2 and PU1 is the absence of the hard segments in PU1, resulting from the reaction of the chain extender with the isocyanate, which means that there is no phase separation structure. This difference is supposed to be reflected in the interfacial relaxation that follows the glass transition due to charge separation at the internal phase separation interface [169, 181]. However, in this dielectric spectrum, the process is overshadowed by the conduction process in the high temperature and low frequency region, so that the interfacial relaxation of the PUs cannot be effectively analysed. The interfacial polarisation behaviour of the designed PUs will be further investigated by the TSDC method in the next section.

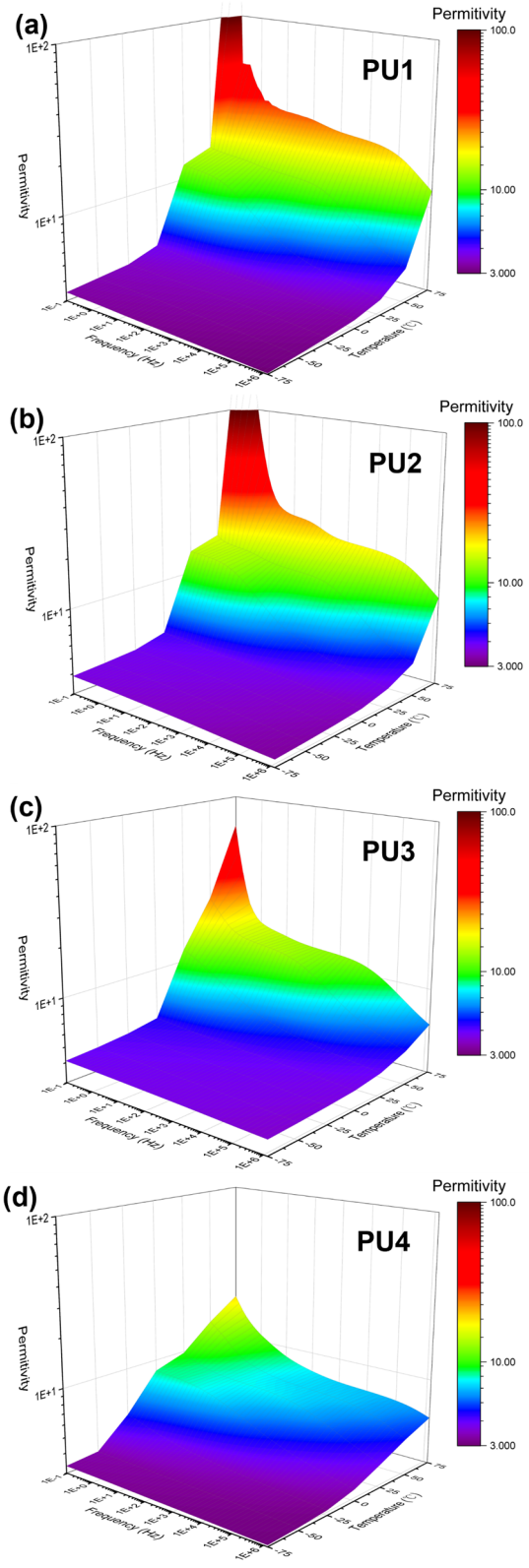

Figure 4-5: The relative permittivity versus the frequency and temperature of PU1 (a), PU2 (b), PU3 (c), and PU4 (d).

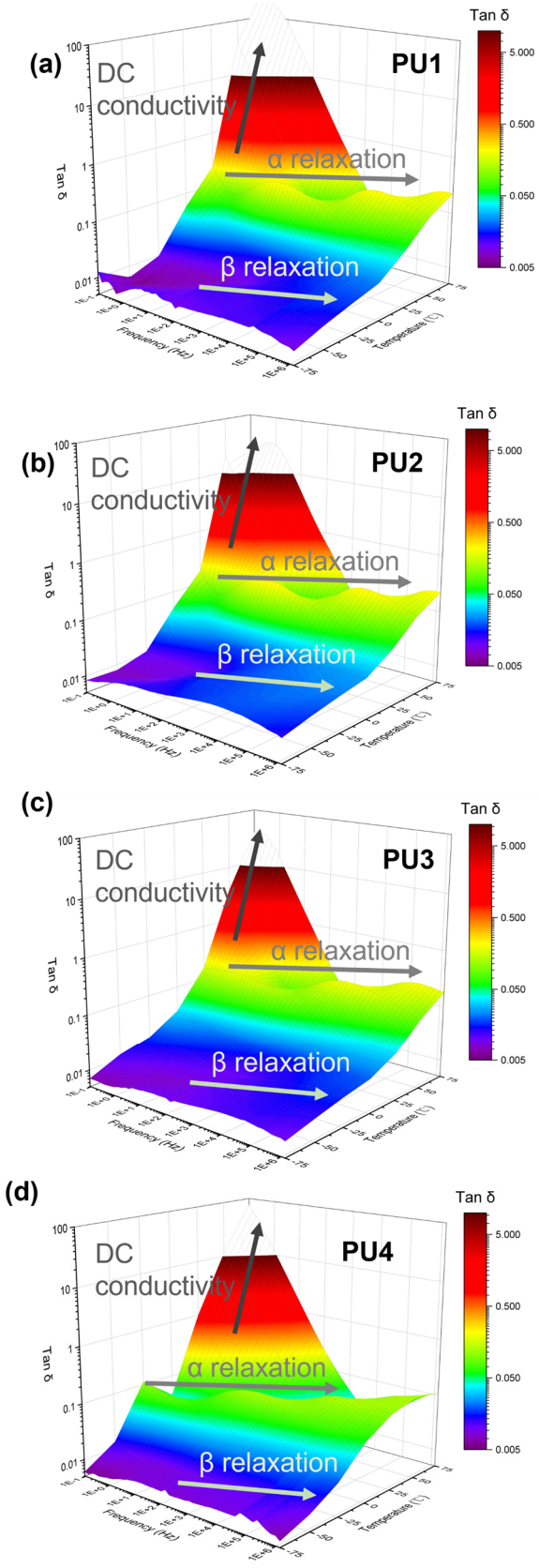

Figure 4-6: Dielectric loss tangent (tan δ) versus the frequency and temperature of PU1 (a), PU2 (b), PU3 (c), and PU4 (d).

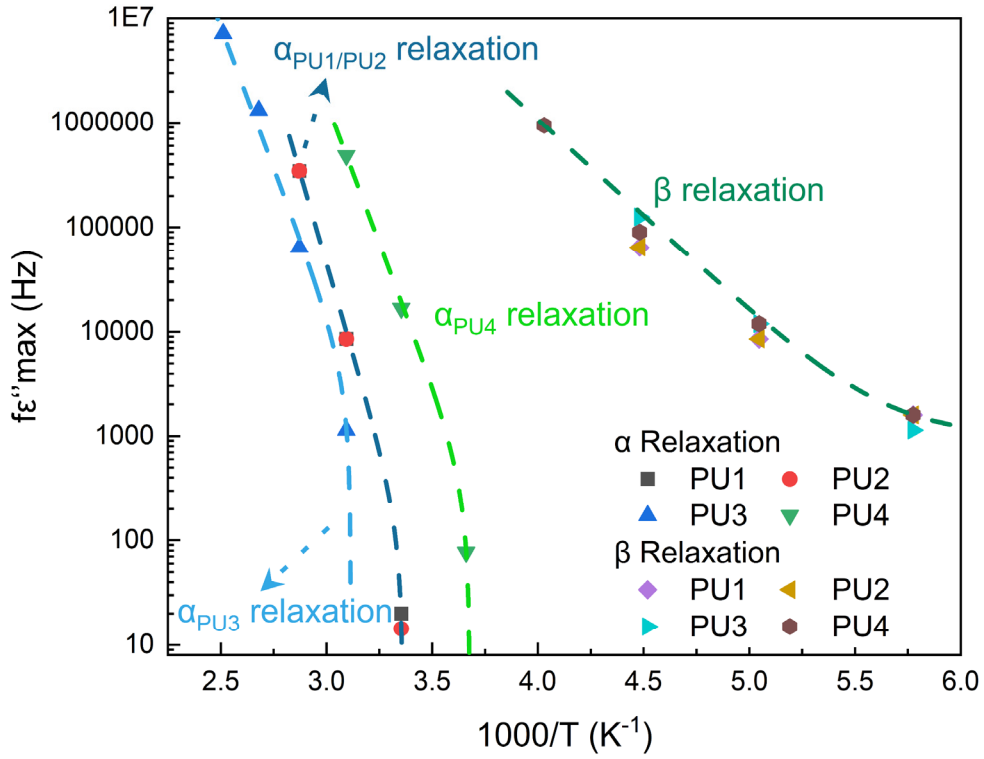

Figure 4-7: Arrhenius plots for the α-relaxation and β-relaxation of the designed PUs.

4.5.2 TSDC Results

Thermal stimulation depolarization current (TSDC) method has been widely used to evaluate various relaxation behaviours and reveal its micro parameters in solid dielectrics [182], [183]. During the heating measurement process, the trapped charges in the material are excited to form depolarization currents at different temperatures according to their different activation energy [171]. However, since the measured TSDC curve is often coupled with multiple current peaks, it is necessary to define and analyse different relaxation behaviours by using reasonable peak fitting methods [170]. Based on the DSC results, Peak 1 comes from the α relaxation process near the glass transition temperature of PUs. Peak 2 is generally considered to be a Maxwell-Wagner-Sillars (MWS) interfacial relaxation that exists in the interface between the SS and HS, in the microphase separated PUs [106, 177]. To quantitatively study the peak shape parameters for different relaxations, the peaks in each curve are fitted using two Gaussian functions. The original TSDC curve and fitted peaks are presented in Figure 4-8.

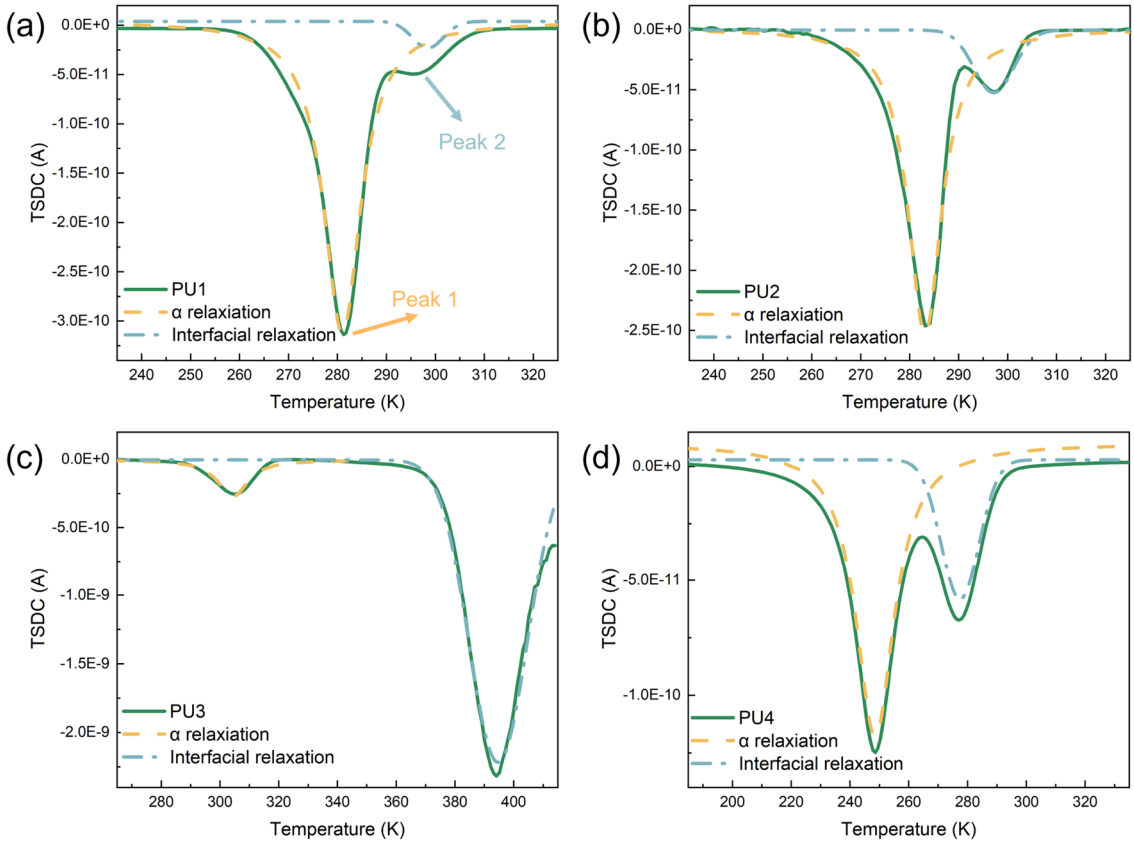

Figure 4-8: TSDC spectrum and peak fitting results of (a) PU1, (b) PU2, (c) PU3, and (d) PU4.

Each discrete current peak can be described by the first order kinetic equation of TSDC [184], in which case the corresponding activation energy and charge density can be obtained from any three points on the peaks (Section 3.3.10, Eq. **(3.5)**). In the practical analysis of TSDC results, the activation energy is positively correlated with the centre temperature of each discrete peak and negatively correlated with its full width at half maximum. The activation energy of higher and narrower peaks is higher than that of lower and wider peaks at the same centre temperature. The charge density of each relaxation is the area of each discrete peak, the integral of the current density over the temperature. The ratio of the discrete peak area caused by different relaxations to the whole TSDC peak area is defined as the ratio of the charge of that relaxation to the total charge, which reflects the effect degree of that relaxation behaviour on the overall relaxation behaviour of that material. The calculation results of quantity of charge and activation energy corresponding to each relaxation type are listed in Table 4-3. The TSDC curves of PU1 and PU2 are very similar due to their similar synthetic formulations. The difference is that there are no HS regions formed by reaction of BDO and isocyanate

in PU1, which leads to a very low proportion of charge associated with interface relaxation, only 4.4%. In contrast, the microphase-separated structure of PU2 brings an obvious interface polarization effect, while some traps with deeper energy levels are introduced into PU2. The activation energies of α relaxation and interface relaxation in PU2 are increased to 0.72 eV and 1.79 eV, respectively, with the proportion of interface relaxation charge being 6.32%. With the further growth of the HS content, the HS in PU3 is reversed into a continuous phase, and the degree of phase separation is further increased. The α relaxation in PU3 is dominated by the HS and its activation energy increases to 1.8 eV but the proportion of charge decreases to 8.8%. The soft/hard interfacial state of PU3 is similar as that of PU2, so the activation energy of interface relaxation in PU3 has not been significantly improved. However, the interfacial charge proportion of PU3 has surged to 91.2%. Due to the use of longer PPG chain segments, the glass transition temperature of PU4 is reduced, and the activation energies of α relaxation and interface relaxation are decreased. However, it is worth noting that PU4 still has a significant interface polarization effect, with an interface charge proportion of 23.3%. Due to the interface polarization behaviour between soft and hard segments in phase-separated PU, some traps with deeper energy levels will be introduced into PUs. With the increase of phase separation degree, the charge density of the deeper traps is also enhanced. Traps with deeper energy levels are usually considered unfavourable for charge transport in polymer dielectrics [185]. The TSDC results explain well from the perspective of dielectric relaxation behaviour why PU2 and PU3 have lower electrical conductivity and robust dielectric strength. The increase in phase separation implies an increase in the percentage of interfacial charge occupying the deeper energy levels, thus hindering charge transport. Meanwhile the activation energies for α relaxation and interfacial relaxation of PUs composed of longer, more flexible polyol chains are lower than those of PUs composed of short-chain polyols.

Table 4-3: Calculation results of charge and activation energy in different relaxation behaviours.

Sample code	Relaxation peak	Charge (nC)	Ratio of total charge (%)	Activation energy (eV)
PU1	α relaxation	55.14	95.6	0.71
	Interfacial relaxation	2.55	4.4	1.63
PU2	α relaxation	39.96	86.3	0.72
	Interfacial relaxation	6.32	13.7	1.79
PU3	α relaxation	63.36	8.8	1.80
	Interfacial relaxation	658.8	91.2	1.82
PU4	α relaxation	38.63	76.7	0.63
	Interfacial relaxation	11.76	23.3	1.39

4.6 Electronic Energy Structures

To understand the electronic structure of PU molecules and their potential impact on electrical properties, a repeating unit of PU2 segments (Figure 3-4) was constructed in first principle DFT model, where SS fragments composed of PPG (MW=400) and MDI, and HS fragments composed of BDO and MDI assemble the PU segment. The electrostatic potential distribution and optimized conformation of the typical PU unit is shown in Figure 4-9. The electrostatic potential at a point around a molecule is usually defined as the work required to move a unit of positive charge from infinity to this point. The electrostatic potential reflects the electron density, whose value is not directly proportional to the electron density. The electrostatic potential is directly determined by the system charge distribution, the uneven distribution of charge in the molecule will be reflected in the electrostatic potential distribution on the surface of the molecule. Therefore, it is meaningless to focus on the absolute value of the electrostatic potential on the surface of the molecule, and the distribution of its positive and negative charges is the key to characterise the intermolecular electrostatic interactions and polarity. There are prominent regions of negative charge aggregation in the individual carbamate groups

of the PU molecular chain, which can become critical nodes in the charge transport process of PUs. A quantitative result is reflected from the extracted total density of states (TDOS) of the molecular orbitals and the partial DOS (PDOS) of different molecular fragments, as exhibited in Figure 4-10. The energy level of highest occupied molecular orbital (HOMO) of PU unit is -5.8382 eV. It can be seen that the main contribution to HOMO comes from the carbamate generated by the reaction between PPG/MDI on SS fragments. Carbamate group generated by BDO and MDI on the HS fragments is the main contributor to the HOMO-1 orbital, whose orbital energy level is -6.0298 eV, and the energy gap between this and HOMO is 0.1916 eV. In solid band theory, HOMO is considered to be the energy level most likely to be excited by heat or electric field to form conduction current across the bandgap barrier [186]. However, there is an energy barrier of 0.1916 eV between the SS and the HS of phase-separated PUs, which formed "walls" that hinders charge transportation along the PU chain, thereby, enhancing insulation performance of the materials. The addition of the chain extender of the short diol allows the urethane in the PU to exist in two non-aligned energy levels, where the energy gap between them is an important contributor to the interfacial relaxation with deeper energy level seen in the TSDC results. Furthermore, it can be concluded that the orbital energy level of the urethane groups formed with MDI and the longer polyol molecular chains are closer to those of the LUMO, and therefore the narrower bandgap barrier led to a rapid decrease in their insulating properties. The results of the quantum chemical simulations are in good correlation with previous experimental work together explaining the mechanism by which the phase-separated structure affects the electrical properties of PUs.

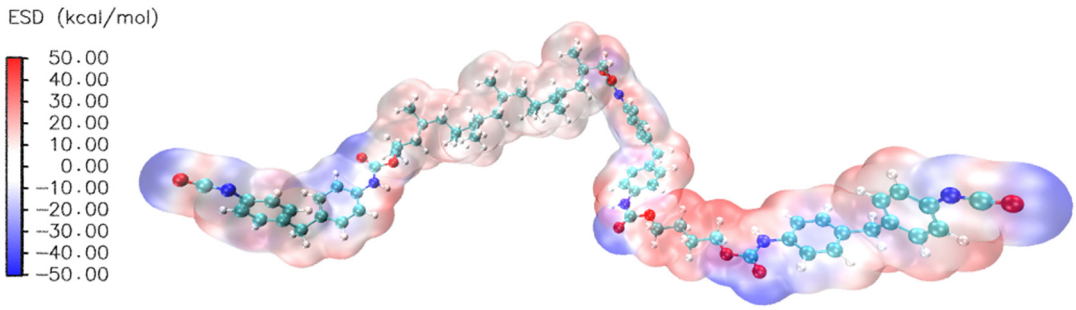

Figure 4-9: The electrostatic potential mapping on the molecular surface of the repetitive PU unit. Red and blue colours represent positive and negative potentials, respectively.

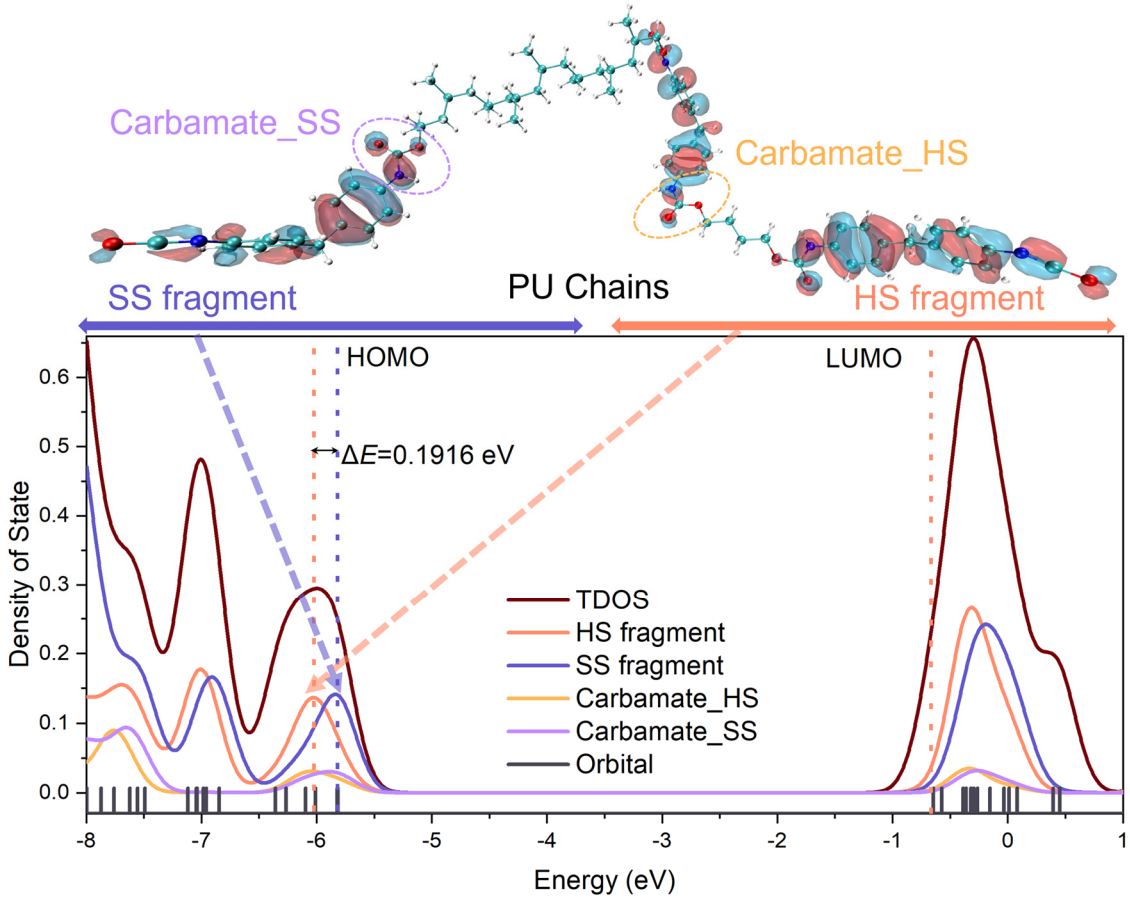

Figure 4-10: Electron density distribution of the optimized molecular structure of PUs repeating units and its molecular orbitals, including the total density of state (TDOS) and partial molecular fragments DOS (PDOS).

4.7 Thermal and Mechanical Performance

The DSC test is a useful method to assist in analysing the various relaxation behaviour of PUs and to obtain their thermal properties. Figure 4-11 presents the DSC traces of designed PUs after erasing their thermal history. The glass transition temperature (T_g) of PU1 is found to be 284.6 K, which is very close to be 286.1 K of PU2. With the increase in the content of HS, T_g of PU3 was increased to 315.7 K due to the crosslinking via hydrogen bonds between the SS and HS was strengthened. The T_g 256.7 K of PU4 with more flexible SS is much lower than those of other PUs.

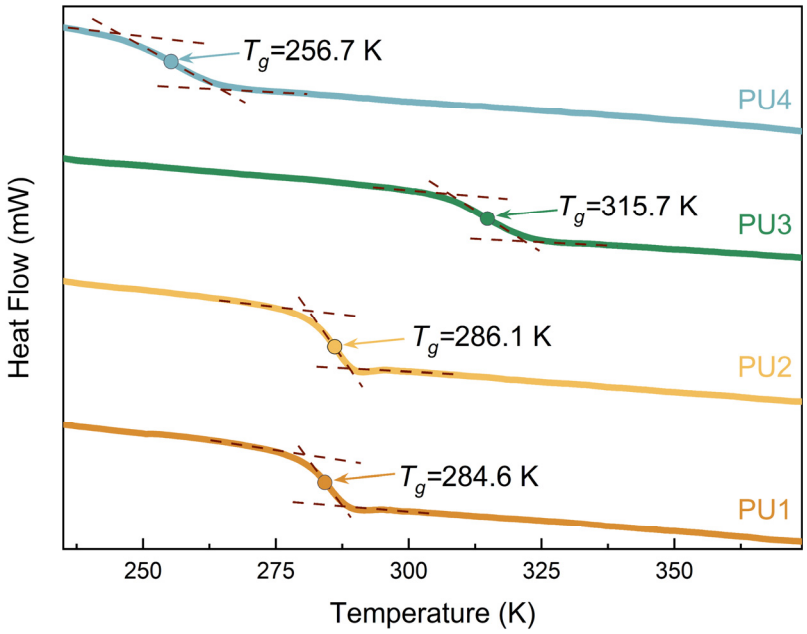

Figure 4-11: DSC thermogram glass transition temperature (T_g) of designed PUs.

Table 4-4 reveals the mechanical properties of designed PUs in tensile tests. Similarly, silicone rubber commonly used in engineering have been tested to provide a visual comparison.

Table 4-4: Tensile strength and elongation at break of designed PUs.

Sample code	Tensile Strength (MPa)		Elongation at break (%)	
	Average	Standard deviation	Average	Standard deviation
PU1	1.25	0.12	2854.3	127.3
PU2	3.71	0.14	1466.7	106.1
PU3	28.03	0.72	803.6	97.4
PU4	9.38	0.23	954.8	134.2
Si-R	5.31	0.17	764.8	101.5

All PUs with phase-separated structures, PU1, PU2 and PU3, displayed higher tensile strength and elongation at break than Si-R. The tensile strength of PU2 with its phase-separated structure is increased by 261% compared to PU1, although its corresponding elongation at break is also reduced by 51%. It can be clearly seen that two-phase structure with SS and HS greatly enhances the mechanical properties of the PUs, and with the

increase in the proportion of HS, PU3 becomes harder, exhibiting a tensile strength of 28.03 MPa. The tensile strength and elongation at break of PU4 are 9.38 MPa and 764.8%, respectively.

4.8 Summary and Conclusions

In this chapter, the interrelationship between micro-structure and macro-performance of PU elastomers was comprehensively investigated.

The chemical composition of designed PUs and their hydrogen bonding crosslinking status were obtained by deconvoluted FTIR in section 4.2. The designed polyurethane was orderly synthesised with no significant by-products. The hydrogen bonding structure was measured in all designed PU, which is the intrinsic driver for achieving self-healing. Subsequent section 4.3 indicated the microphase separating morphology of designed PUs by AFM. Clear phase separation structures were observed in PU2, PU3 and PU4 due to the formation of the HS domain constructed by isocyanate and short diols. The hard domain switched from a sporadic dotted distribution to a continuous banded distribution with the rise of HS%. The actual HS% observed by AFM is close to the revised HS%, which can be used to describe the degree of phase separation.

In section 4.4, PU2 and PU3 showed better insulation properties than conventional dielectric elastomers (silicone rubber) by means of DC conductivity tests and DC breakdown tests. The phase-separated structure greatly improves the insulating properties of PUs, including electrical conductivity and breakdown strength, as well as the higher the HS%, the more pronounced this improvement gets. In contrast, the insulating properties of some PU consisting of longer and more flexible polyol chains were significantly reduced.

The structure-property relationship of microphase separated PUs were characterized from two aspects: dielectric relaxation behaviour and quantum chemical calculation, as revealed in section 4.5 and section 4.6, respectively. There are three distinct relaxation behaviours in phase-separated PUs, β-relaxation, α-relaxation, and interfacial relaxation between the microphase interfaces, analysed from DRS and TSDC, where β-relaxation is independent of the phase-separating degree and α-relaxation is related to the glass

transition of the continuous phase in the PUs. The interfacial polarisation originates from the interface between the soft and hard domains within the phase-separated PU, which has a deeper activation energy and is not conducive to charge transport. As the degree of phase separation increases, the content of interfacial charges grows increasing the proportion of more deep traps and the insulation properties of PU3. The deeper reason for this phenomenon lies in the inconsistency of the energy levels of the molecular orbitals between the urethane in the soft segment and the urethane in the hard segment. There is an energy barrier of 0.1916 eV between the SS and the HS of phase-separated PUs, which formed "walls" that hinders charge transportation along the PU chain, thereby, enhancing insulation performance of the materials. In contrast, polyurethane formed from longer polyol chains have a narrower forbidden band width. As a result, the insulating properties of the material, such as PU4, are lower. The thermal and mechanical properties of designed PUs are supplemented in Section 4.7.

The structure-activity relationships of phase-separated PUs were systematically analysed, which play a significant role in instructing the preparation of high-performance PU materials. Phase separated PUs with shorter polyols have better dielectric strength are suitable for application on HV insulation. The insulating properties are improved with the increase of phase separation degree. Furthermore, PU2 and PU3 with excellent dielectric strength and mechanical properties are selected to verify their self-healing performance under electrical damage.

Chapter 5 Characterization and Evaluation of Self-healing PU under Electrical Damage

5.1 Introduction

Chapter 5 characterizes the self-healing mechanisms of the designed PUs and evaluates its self-healing performance under electrical damage. The self-healing mechanism of PUs was investigated in terms of reversible hydrogen bonding network and shape memory effect, as revealed in section 5.2 and section 5.3, separately. The self-healing performance of screened PU samples for electrical damage was examined both macroscopically and microscopically in section 5.4, with the recovery of electrical properties investigated. The electrical damage was carried out using the general method of electrical tree ageing, where samples containing needle plane electrode structures were prepared for accelerated ageing experiments, allowing electrical tree branches to grow in a relatively short period of time. The characterisation of the self-healing effect consists of two aspects, the visual observation of internal defects in the material from multiple scales and the measurement of the state of recovery of the insulating properties of the material. Confirmation of the self-healing capability of the designed PU and the elucidation of its repair principles is a key part of the development of smart materials for the next generation electrical insulation.

5.2 Reversibility of Hydrogen Bonding Networks

The hydrogen-bonded structure of the designed PUs was confirmed by deconvolution FTIR in section 4.2, while the reversibility of this hydrogen-bonded structure, the two states of opening and reconfiguration at different temperatures, needs to be further investigated in this section. *In situ* FTIR spectroscopy is the usual methodology for investigating the status of hydrogen bonding at various temperatures [187, 188]. Two thermal cycles were conducted in PU2 and PU3, where FTIR is measured every 10 ℃ in the heating process. Based on the previous study on PU's FTIR spectroscopy, the carbonyl region from 1780 to 1640 cm^{-1} was mainly demonstrated, as shown in Figure 5-1. The maximum absorbances of each curve were normalized to 1. The content of

hydrogen bonding carbonyl of PU2 decreases when the temperature was above 50 ℃, and the hydrogen bonding crosslinking for PU network is weakened. The content of hydrogen bonding carbonyl of PU2 returns to the initial level when the temperature is reduced to 30 ℃. The hydrogen bonding crosslinking network of PU2 shows excellent reversibility in two thermal cycles from 30-70 ℃, while for PU3, the re-crosslinking of hydrogen bonds can only occur above 100 ℃.

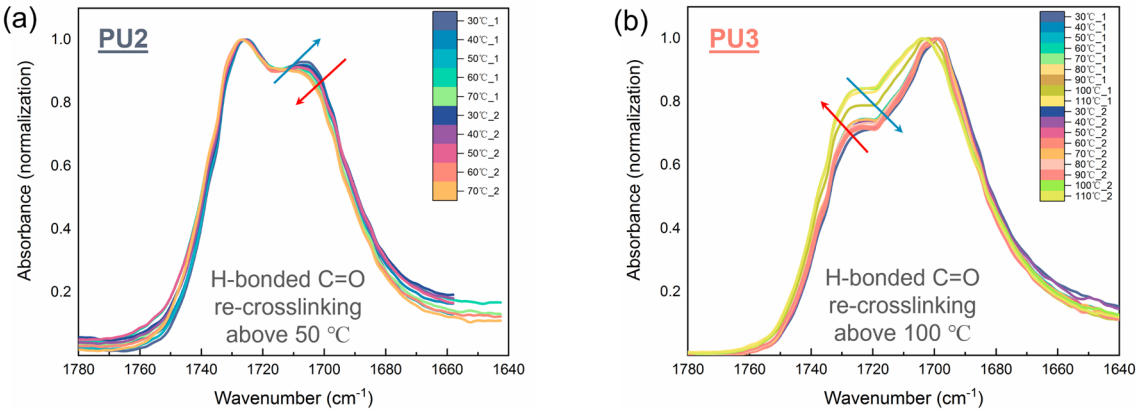

Figure 5-1: *In situ* FTIR results at 30-70 ℃ for PU2 (a), and 30-110 ℃ for PU3 (b), with a heating rate of 5 ℃/min and a hold time of 10 min per point. The trajectory in heating and cooling is indicated by the red and blue arrows, respectively.

5.3 Shape Memory Effects Evaluated by Conformational Entropy

Shape recovery in shape memory PUs is driven by the recuperation of conformational entropy following deformation, which can be fundamentally described in terms of thermodynamics and statistical mechanics [90]. A single dynamic mechanical analysis (DMA) experiment allows us to quantify the shape memory effect in terms of stored and released energy densities and their relationship with the shape memory efficiency [89]. The test was performed for tensile tests (Q800 TA Instrument) of PU samples at a heating rate of 2 ℃/min from -50 ℃ to 100 ℃. The DMA output of PU2 and PU3 is illustrated in Figure 5-2. As the temperature increases from -60 to 110 ℃, PU softens while it transitions through the glassy, glass transition, and rubbery plateau regions of viscoelasticity. The glass transition temperature (T_g) of PU2 and PU3 is 15.4 ℃ and 42.2 ℃, respectively. It is worth noting that the T_g obtained by DMA and DSC will differ slightly due to the different test principles.

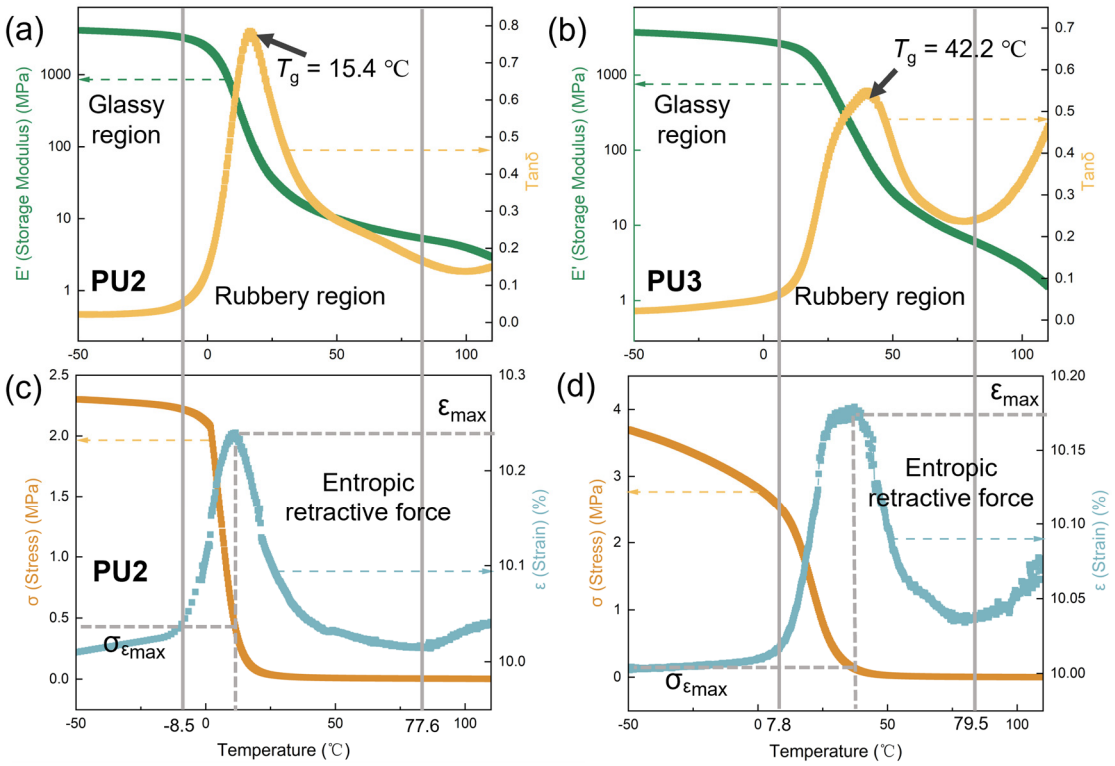

Figure 5-2: DMA results of PU2 and PU3. (a and b) The storage modulus (*E'*) and loss factor (tan δ) of PU2 and PU3 plotted as a function of temperature. (c and d) The stress (σ) and strain (*ε*) of PU2 and PU3 plotted as a function of temperature as obtained by DMA.

The strain (*ε*) increases at the onset of the glass transition and subsequently decreases as temperature increases. The length increase is considered as a result of the molecular architecture and viscoelastic changes of a polymer, while the length retraction is attributed to conformational entropy and the shape memory effect. According to the thermodynamics of molecular networks and the theory of rubber elasticity, the chain order increases, resulting in a decrease of the conformational entropy expressed per volume (ΔS, kJ/m^3) as [189]:

$$\Delta S = -\frac{\rho R}{2M_j}[\alpha^2 + \frac{2}{\alpha} - 3] \tag{5.1}$$

Where α is the extension ratio L/L_0, ρ is density, R is the gas constant, and M_j is the molecular weight between crosslinks/entanglements. In stretching, the decrease in entropy also generates an associated retraction force, and the resulting retraction stress (σ_R) can be expressed as:

$$\sigma_R = \frac{\rho RT}{M_j}[\alpha - \frac{1}{\alpha^2}] \tag{5.2}$$

Where T is temperature. As will be seen, equation (5.1) and (5.2) were utilized to determine stored entropy (ΔS_s) and stress at the maximum strain ($\sigma_{\varepsilon_{max}}$) respectively during a DMA experiment, ultimately leading to quantitative assessments of shape memory effect.

The quantitative correlation between ε_{max} values and $\sigma_{\varepsilon_{max}}$ as a function of the crosslink/entanglement density (V_j=ρ/ M_j) and $\tan\delta_{max}$ was indicated in Figure 5-3 [190]. This relationship correlates the stored energy to strain at maximum and stress values. Hence, linear relationships were obtained as:

$$\begin{aligned} \varepsilon_{max} &= 55.791 \frac{\tan\delta_{max}}{\ln(\rho / M_j)} \\ \sigma_{\varepsilon_{max}} &= 0.00516(\tan\delta_{max})(\rho / M_j)^{0.6613} \end{aligned} \tag{5.3}$$

ΔS_s is expected to be proportional to the product of the maximum strain (ε_{max}), and stress at maximum strain ($\sigma_{\varepsilon_{max}}$) and is expressed as:

$$\Delta S_s = 5.2819 \times \varepsilon_{max} \times \sigma_{\varepsilon max} \tag{5.4}$$

In order for a polymer to exhibit high efficiency shape memory effect, the ΔS_s must be high, which means the ε_{max} and $\sigma_{\varepsilon_{max}}$ should have the highest values. Stored entropic energy density allows quantitative assessments of the shape-memory effect and can be utilized in any material that exhibits a glass-transition temperature and a rubbery plateau. In this research, the calculated stored entropic energy density of PU2 and PU3 is 41.13 and 14.18 kJ/m^3, separately, thus indicating that PU2 has more efficient shape memory capability in the rubbery plateau region.

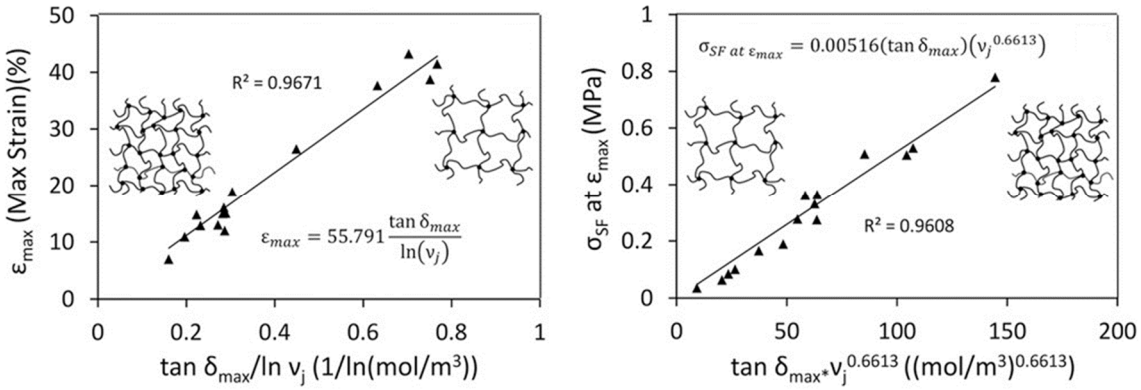

Figure 5-3: Quantitative correlation of the ε_{max}, $\sigma_{\varepsilon max}$, ΔS_S values with the crosslink/entanglement density v_j and $\tan\delta_{max}$ of thermoplastic and thermosetting polymers [190].

5.4 Self-healing Performance of PUs under Electrical Damage

Insulation degradation, especially electrical dendrite damage, has always been the biggest problem with polymeric insulation materials in applications. Inevitably, there are weak points in the manufacture of polymeric dielectrics which become electrical stress concentrations during long term operation and cause electrical treeing ageing. The defects are often internal to the material and are difficult to detect. The ability of equipment to maintain adequate overall insulation performance for a period despite the presence of these local defects can conceal their presence before they lead to irreversible failure and economic loss. There are several ways to detect defects in the material, such as partial discharge testing and it is possible to detect defects in the material that occur during the preparation process or during operation, including the detection of defects such as electrical treeing. However, this method of testing can only determine whether the material or equipment meets the factory requirements or is suitable for further use. If it is confirmed that the equipment has serious latent defects and is no longer fit for use, it can only be scrapped, resulting in a huge waste of resources and economic loss.

In the previous two sections, the reversible hydrogen bond network and excellent shape memory capabilities of PU2 were confirmed, which are expected to provide the ability to repair internal micro-defects in the material. In this section, the self-healing performance of PU2 has been characterized, including the recovery of insulation properties and the repair of damaged channels through the deliberate introduction of electrical damage.

5.4.1 Construction of Electrical Damage Initiation and *In-situ* Observation Platform

An *in situ* electrical ageing observation platform was established to monitor the ageing and healing process in real time, as indicated in Figure 5-4 (a). The HV AC power supply consists of a Trek power amplifier with a signal generator that can generate sine, square and pulse waves up to 50 kV as requested, while an oscilloscope is used to monitor the output waveform. An optical microscope (Nikon DS-Ri2) connected to a computer is used to display of real time images showing the growth or repair process of the electric tree. The sample platform contains two parts, a test electrode as shown in Figure 5-4 (b), and a petri dish filled with silicone oil. The test electrodes are placed integrally in the petri dish, which is made of plastic to provide support and electrical insulation for the electrodes, while the silicone oil is effective in preventing partial discharges that may occur at the high-voltage connection points. A needle-plane electrode system was used to initiate electrical trees and the distance between electrodes was 3 mm. Self-healing PU samples are treated using the cold nesting method, whereby the assembled electrodes were encapsulated by an epoxy resin that generates only a small amount of heat during the curing process. The reason for using this method is that silicone oil may penetrate inside the sample through the pinholes in the sample and thus affect the healing process. In addition, the epoxy resin housing is a good safeguard against the position of the needle electrode being shifted, thus destroying the consistency of subsequent continuous measurements. A flexible heating film is placed underneath the Petri dish to provide the sample with a moderate thermal stimulus to trigger the self-healing process.

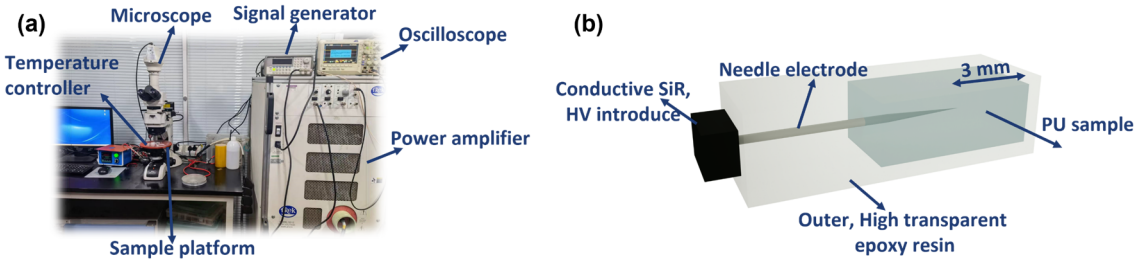

Figure 5-4: (a) In-situ observation platform of electrical damage. (b) Testing electrode for initiating electrical tree.

An AC voltage of 15 kV/50 Hz was applied to the needle electrode and an area of dendritic damage was formed within approximately 30 minutes. The voltage was then withdrawn so that the defect no longer developed and self-repair of the electrical dendritic damage in the PU began to be achieved. The healing temperature was set to

50 °C for about two days, depending on the reconstitution temperature of the hydrogen bonding network in the section 5.2. Throughout the ageing and repair process, the same PU samples were removed at specific time points without further thermal treatment for tests such as partial discharge and 3D-CT, which are described in detail in the corresponding sections.

5.4.2 Repair of Dendritic Damage

Figure 5-5 shows the optical images of electrical tree development taken from the self-healing PU2 samples at different aging or healing stages. After the voltage had been applied for 30 minutes, the electrical damage developed into a dendritic defect with about 250 × 250 μm area. The hollow channels caused by continuous partial discharge is the most common type of electrical damage, the continued development of which inevitably leads to a complete breakdown of the insulation properties of the material. Fortunately, the developed PU2 exhibited the expected capability to self-healing under electrical damage. Within 30 min after voltage withdrawal, it can be obviously observed from the 2D image as obtained by optical microscope that the terminal dendritic channels of PU2 was closed at room temperature due to the shape memory effect. The shape memory effect of PU stems from the ability of its soft segments to maintain deformation-induced segment orientation by vitrification transition, i.e., to recover their original shape after deformation [191, 192]. Therefore, for slight damage of PU2, such as the ends of discharge channels or small branches of electric trees, it can be completely or mostly healed within a short time (30 min) without any external thermal stimulation. Treatment at elevated temperatures is required to promote re-formation of the reversible hydrogen bond network for healing major dendritic channels. There are only a few main branches in PU2 observed by optical microscope after 24 hours of heating healing at 50 ℃. After 48 hours, the healing of PU2 has reached its limits. Most of the hollow channels of PU2 were healed. Some scattered black material is visible and is thought to be carbon deposits from the discharge, dispersed in the polymer matrix after the discharge channels have been repaired. In contrast, the PU3 does not demonstrate the self-healing function, as shown in Figure 5-6. The critical factor in the difference in self-healing capability is that there are different degrees of phase separation between PU2 and PU3. The DMA results show that the softening temperatures (about 70 °C) of PU2 and PU3 are close, while the

repair temperature must be lower than the softening temperature of the material. The continuous phase of PU2 is soft domains and the hydrogen bonding between the hard and soft segments undergoes re-crosslinking at a heat treatment of 50 °C, while the HS do not undergo a phase change at this temperature, maintaining the overall shape and strength of the material to some extent. In comparison, the continuous phase of PU3 is hard domains which requires a temperature above 100 °C to reconfigure the molecular network, at which point the phase change in the hard domain results in the overall strength of the material not being maintained. Self-healing materials require that a part of the frame structure within the material remains unchanged when a part of the material's structure is reconfigured. Therefore, PU3 is not suitable as a self-healing dielectric material.

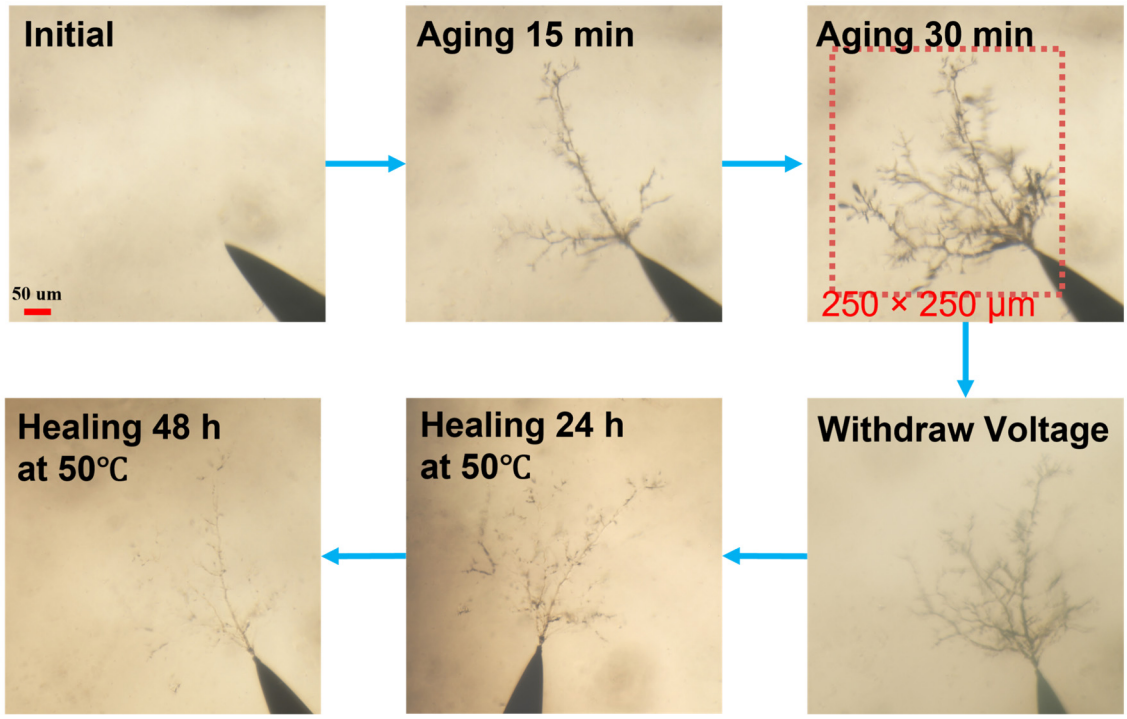

Figure 5-5: 2D optical images were taken from the self-healing PU2 samples at different aging/healing stages.

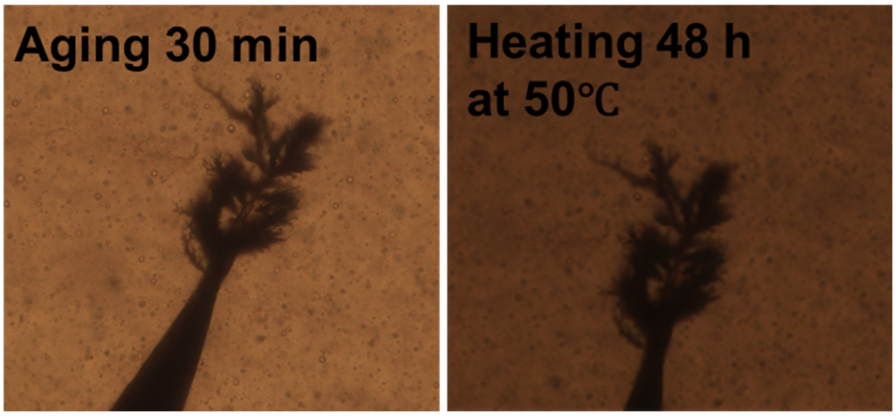

Figure 5-6: PU3 cannot achieve self-healing of electrical damage.

Besides the optical microscope being used to observe the development of electric trees, The 3D topographic features of the electrical tree channel before and after healing were measured using a 3D X-ray micro-CT (3D-CT, Xradia micro-XCT-500, Carl Zeiss XRM, Germany) to complement those details missed by the 2D images as well as for a quantitative analysis of channel healing efficiency. Samples were mounted on the holder with an aluminium tube as the adapter and rotated horizontally, pausing at discrete angles to collect 2D projection images, which were then combined to produce a 3D reconstruction of the sample's volume dataset. The 3D morphological feature of PU2 was characterized by 3D-CT with a voxel of 0.6 μm. Figure 5-7 (a) and (b) are PU2 samples after aging for 30 min and healing for 48 hours, which is consistent with the samples observed by optical microscope in Figure 5-5. The imaging principle of 3D-CT is that X-rays have different transmittance for materials of different densities, so the inspection method is very sensitive to hollow channels in the material and ignores carbon deposits within the material. The 3D-CT results confirmed that the dendritic hollow channels of PU2 were completely healed, with a good enough self-healing efficiency of 99 % in terms of the defect volume. The self-healing efficiency was defined as the ratio of the volume of the repaired non-hollow region to the initial volume. Figure 5-8 is supplemented with scanning electron microscope (SEM, Hitachi SU8010) images of these channels before and after healing. There are two SEM images as obtained from two different aged and healed samples since the sample preparation for cross-sectional SEM is destructive. The SEM images of the cross-sections of the samples reflect that the holes and channels around the damaged region in PU2 are refilled after heat-healing. The

ability of PU2 to cure dendritic channels or defects created by the discharge was confirmed by various microscopic images.

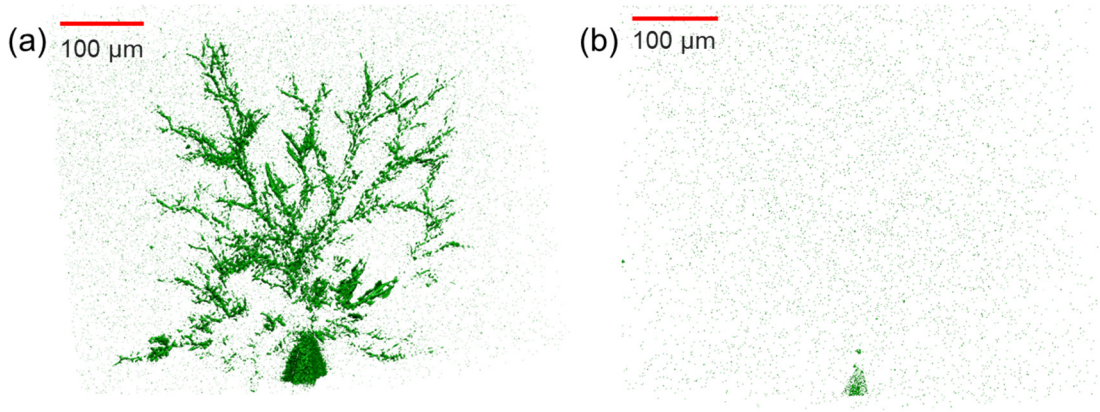

Figure 5-7: The 3D reconstruction image of electrical damage in PU2 by 3D-CT at the aging (a) and healing stages (b).

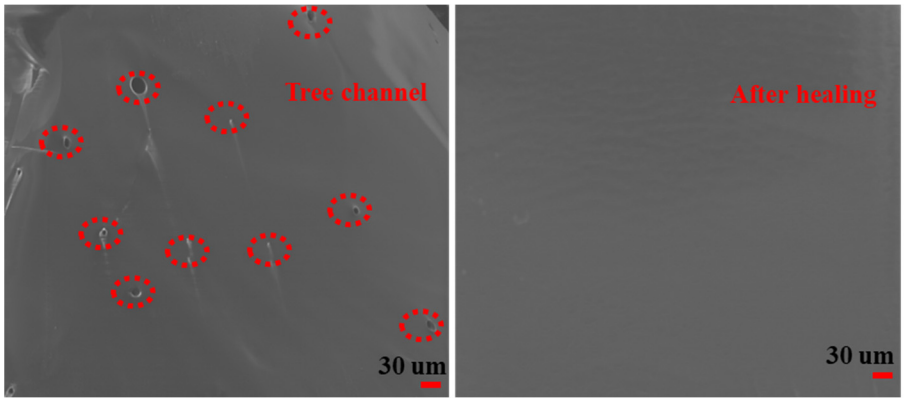

Figure 5-8: SEM images of before and after self-healing of PU2.

5.4.3 Restoration of Insulating Properties Evaluated by Partial Discharge

Although in the previous section it was demonstrated that PU2 is up to 99% efficient in repairing its electrically damaged channels, it is important to verify that these newly repaired areas have comparable insulating performance to the initial material. A meaningful self-healing material cannot only include wound closure, it must also satisfy performance recovery. However, some general methods for testing macroscopic electrical properties, such as leakage currents, may not be suitable for detecting internal micro-defects in the material. When the size of the defect is not large enough, the defect does not cause a change in the macroscopic insulation characteristics within a short period of time. Partial discharge (PD) testing is widely used to examine the reliability of

insulated equipment and to determine defects or air gaps within the equipment. PD in polymers is thought to be a major origin of electrical damage, and the size of the dendritic damage is positively correlated with the maximum apparent discharge magnitude (Q_m) [18]. Consequently, the insulation performance of PU samples at different stages of the self-healing and ageing process is well suited to be assessed by measuring the magnitude of the PD. A multi-channel digital PD analyser (TWPD-2E, Baoding Tianwei, China) was used to detect the maximum apparent discharge amplitude (Q_m) under an applied voltage of 3 kV at different stages of tree formation and healing to characterize the degree of electrical aging. The error bars represent the maximum and minimum of these sample Q_m values in each PD test. The following PD test is performed at a voltage of only 3 kV/ 50 Hz and the test time is short. It is therefore considered a non-destructive test and does not further extend the electrical damage of the sample in every PD test. Meanwhile, the same needle-plate electrodes were retained in order to compare partial discharge data for PU samples at different stages of the aging-healing process. PD tests were carried out at six different stages, initial state, ageing for 15 min, ageing for 30 min, stopping ageing, self-healing for 24 h, self-healing for 48 h. The time points of the sample measured were chosen to coincide with the PU samples shown in Figure 5-5 and Figure 5-6, where changes in performance were successfully matched to the morphology of the damaged areas.

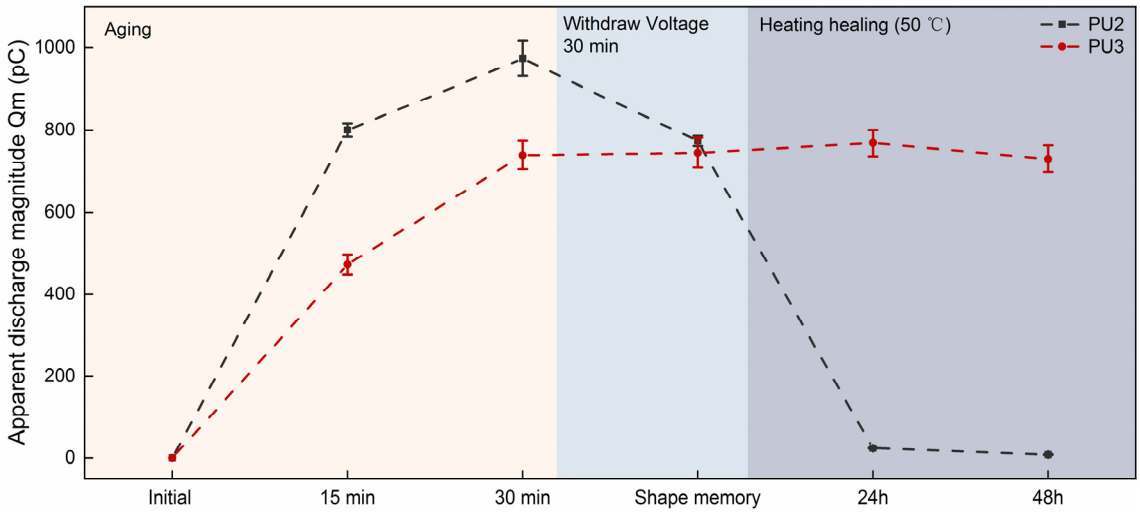

Figure 5-9: Insulation properties recovery of self-healing PU. The maximum apparent discharge magnitude (Q_m) of the PU2 and PU3 that was electrically aged for 30 min and then heated to heal for 48 hours, where Q_m value and the max-min error bars were measured in the PD tests.

Figure 5-9 visually shows the self-healing capability of PU2 against electrical damage, where the value of maximum apparent discharge magnitude (Q_m) of the PU2 and PU3 at different stages is indicated in Table 5-1. With the increase of aging time, the Q_m of PU2 and PU3 also continue to rise, which corresponds to the expansion of the volume of dendritic channels, while the Q_m (472.1 pC) of PU3 is lower than that of PU2 (974.34 pC) due to PU3's more robust insulation properties. In the shape memory region, when the applied voltage is removed, the insulation strength of PU2 increases and the Q_m of PU2 decreases to the same level as that of PU3. After 24 hours of heat treatment, the healing effect of PU2 became increasingly evident, with the Q_m dropping sharply to around 20 pC, close to the level of the initial sample. On the contrary, the Q_m of PU3 has remained high due to the presence of damage channels. After 48h of self-healing, the Q_m of the PU2 was close to zero, which attests the complete recovery of the insulation properties of PU2. The series of experiments confirmed the efficient self-healing capability of PU2, including the repair of damaged structures and the recovery of insulation performance. PU2 is considered as a successful self-healing insulating material because it retains excellent self-healing capabilities for electrical damage while providing robust dielectric strength.

Table 5-1: The maximum apparent discharge magnitude (Q_m) of the PU2 and PU3 at different stages

Stage	Maximum apparent discharge amplitude (Q_m) ± error (pC)	
	PU2	PU3
Initial	0	0
Ageing 15 min	800.14±16.8	472.1±24.3
Ageing 30 min	974.37±42.04	739.63±34.38
Shape memory	773.48±12.4	745.2+36
Healing 24 h	23.625±0.775	768.7±32
Healing 48 h	7.8275±0.95	730.5±32.6

5.5 Self-Healing Mechanism of PU

So far, we have a clear and comprehensive understanding of the self-healing behaviour of PUs to electrical damage. When the discharge channel is generated, the terminal microcracks will actively close due to the shape memory effect driven by high conformation entropy from the phase separation structure of PU2, preventing further deterioration of electrical properties. Re-formation of hydrogen bonding networks occurs under an external stimulus of 50 ℃ to achieve complete healing of electrical damaged area, while restoring its electrical properties. Figure 5-10 exhibits the self-healing mechanism in PUs. For PU3, the HS domain has become a continuous phase at 55% HS, which severely restricts the flow of SS. A temperature of up to 100 ℃ for hydrogen bond recombination is higher that the softening point temperature of PU3, which means that the material is unable to maintain its structural strength at the healing temperature.

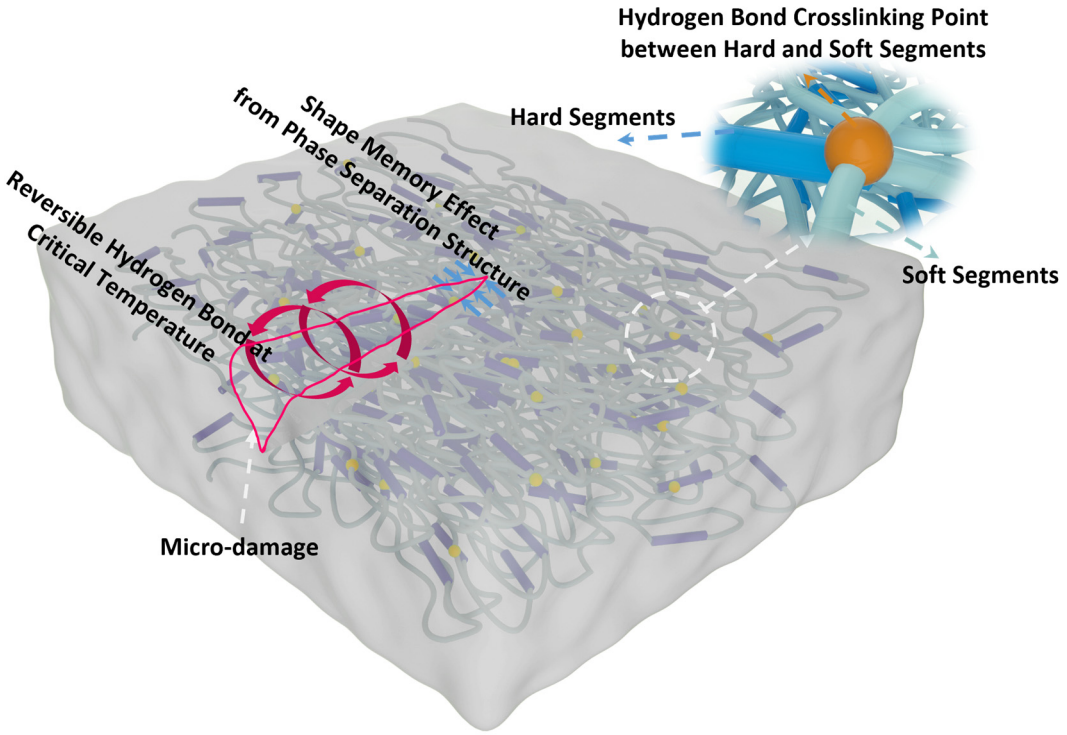

Figure 5-10: Schematic of self-healing mechanisms in PUs utilizing hydrogen bonding networks and shape memory effect.

5.6 Conclusions

In this chapter, A self-healing PU elastomer with robust dielectric strength utilizing hydrogen bonding crosslinking networks with shape memory effect was characterized and implemented.

Section 5.2 verified the reversibility of the hydrogen bonding crosslinking networks of PU2 by variable temperature FTIR. The hydrogen bonding crosslinking networks of PU2 are weakened when the temperature is above 50 ℃, and the content of hydrogen bonding carbonyl returns to the initial level when the temperature is reduced to 30 ℃. In contrast, the reconfiguration of the hydrogen bonding network of PU3 appears above 100 ℃. The calculation results from DMA show that PU2 has higher conformational entropy compared to that of PU3, as revealed in section 5.3. Stored entropic energy density allows quantitative assessments of the shape-memory effect. PUs with higher conformational entropy exhibits more efficient shape memory effects at plateaus above the glass transition temperature, which can have a positive effect on self-healing. The DMA results also demonstrate the softening point temperature of 77.6 ℃ and 79.5 ℃ for PU2 and PU3 respectively, meaning that PU2 retains this ability to reconfigure the hydrogen bonding network at 50 ℃ but maintains its overall strength.

The efficient self-healing capability under electrical damage of PU2, including the repair of damaged structures and the recovery of insulation performance, was confirmed in section 5.4. An *in situ* electrical ageing observation platform was established to monitor the ageing and healing process in real time. Self-healing PU samples were processed using the cold nesting method to prevent external disturbances during long-term ageing and healing. Observations from optical microscope and 3D-CT show that PU2 can fully heal the electrical damaged area at 50 ℃ while restoring its insulating performance. A comprehensive characterisation of the effective healing, with a healing efficiency of 99%, of dendritic discharge channels by PU2 under moderate thermal stimulation was obtained from 2D optical micrographs, 3D computed micro-X-ray tomography and cross-sectional SEM images. Additionally, the insulating performance evaluated in terms of the maximum discharge amplitude (Q_m) of the partial discharge within the material also confirms that the Q_m of PU2 can drop back to its initial level after the damaged channels were healed.

Section 5.5 summarized the self-healing mechanism of PU2. The efficient self-healing capability of PU2 is attributed to its shape memory effect driven by high conformational entropy and the reversibility of hydrogen bonds.

An efficient self-healing PU material with robust dielectric strength has been successfully designed and validated. In the next chapter, self-adaptive function will be organically integrated into this self-healing PU matrix.

Chapter 6 GO/PU Nanocomposites with Simultaneous Self-healable and Self-Adapting Dielectric Behaviours

6.1 Introduction

In chapter 6, A grafted GO/PU nanocomposite with simultaneous self-healable and self-adapting electrical and dielectric behaviour was designed and implemented. In section 6.2, a “bottom-up” synthesis strategy is applied by grafting methylene diphenyl diisocyanate (MDI) to the hydroxyl group on the sides of GO, followed by further polymerization of the polyols and diols with the isocyanate on the graft chain to obtain a reversible hydrogen-bonded polyurethane network with GO as the backbone. The chemical composition and morphological features of the material during synthesis are characterised accordingly. The nonlinear conductivity and dielectric properties of prepared GO/PU nanocomposites are investigated in section 6.3. The grafted GO/PU nanocomposites with 5 vol. % GO exhibit outstanding nonlinear conductivity and dielectric properties to meet the requirements of self-adaptive function for resistive or capacitive field grading. The interfacial interaction between the oxide layer on the GO surface and the matrix is essential for the construction of efficient conductive pathways. Hence, the interfacial transport behaviour from nanoscale to macroscale is studied in the section 6.3 by the combined EFM (electrostatic force microscopy) and KPFM (Kelvin probe force microscopy) techniques. Finally, the repeatable self-healing capabilities is confirmed in section 6.5, involving the recovery of its novel nonlinear electrical properties and structural restoration. due to the photothermal effect of GO, the repair pathways of the composites are extended to include moderate thermal stimulation and near-infrared (NIR) light stimulation. This is the first organic integration of electrical and dielectric self-adaptive and self-healing functions into an electrically insulating material.

6.2 Design and Preparation of Grafted GO/PU Nanocomposites

In this section, the precise design and synthesis of the target material is carried out from three aspects: theoretical analysis, preparation methods and characterisation of the underlying physicochemical properties.

6.2.1 Design of PU Grafted GO based on First Principle

The surface of the monolayer GO sheets prepared by the Hummers method contains a large number of oxygen-containing functional groups produced by the action of strong oxidizing agents [149]. The interface between the oxidized state of the GO surface and the polymer matrix constitutes an energy barrier preventing the effective transport of electrons along the GO network, even though the loading concentration of GO is sufficient to construct a percolation structure formed by physical connection [134]. To understand the electronic structure of PU grafted GO molecules and their potential impact on electrical properties, a repeating unit of PU grafted GO, including typical PU chains composed of hard segment (HS) and soft segment (SS), and GO sheet connected to PU via carbamate bond, was constructed in a density functional theory (DFT) model. As shown in Figure 6-1 (b), the electrostatic potential distribution of PU grafted GO demonstrates that the oxygen defect in the surface of GO has a predominant positive electrostatic potential region which is prone to form a hole trap to attract negative charge carriers [193], while the grafted urethane group on the GO surface is located in negative electrostatic potential regions. A clearer result is reflected from the extracted total density of states (TDOS) of all molecular orbitals and the partial DOS (PDOS) of different molecular fragments, as presented in Figure 6-1 (b). The energy levels of the highest occupied molecular orbital (HOMO) and the lowest unoccupied molecular orbital (LUMO) of the entire unit are -3.72 eV and -3.54 eV from the contribution of graphene molecules. The oxygen defect of GO has only one unoccupied orbital. The energy gap between its orbital energy level and that of LUMO is 4.72 eV, while for the urethane group grafted with GO the energy gap between its most adjacent orbital and that of HOMO decreases to 2.22 eV. Its band gap is slightly higher than that of SS fragment and lower than that of HS fragment. In solid band theory, HOMO and LUMO are considered to be the energy levels most likely to be excited by heat or electric field to form

conduction currents across the bandgap barrier [186]. The oxide layer on the untreated GO surface has a high interfacial barrier, thus, hindering the formation of efficient conductive pathways. After grafting, the interface barrier between GO and PU chains chemically connected by carbamate groups decreases significantly. Hence, we can infer that the grafting method can effectively regulate the interfacial state between GO and PU to obtain an excellent nonlinear electrical and dielectric response.

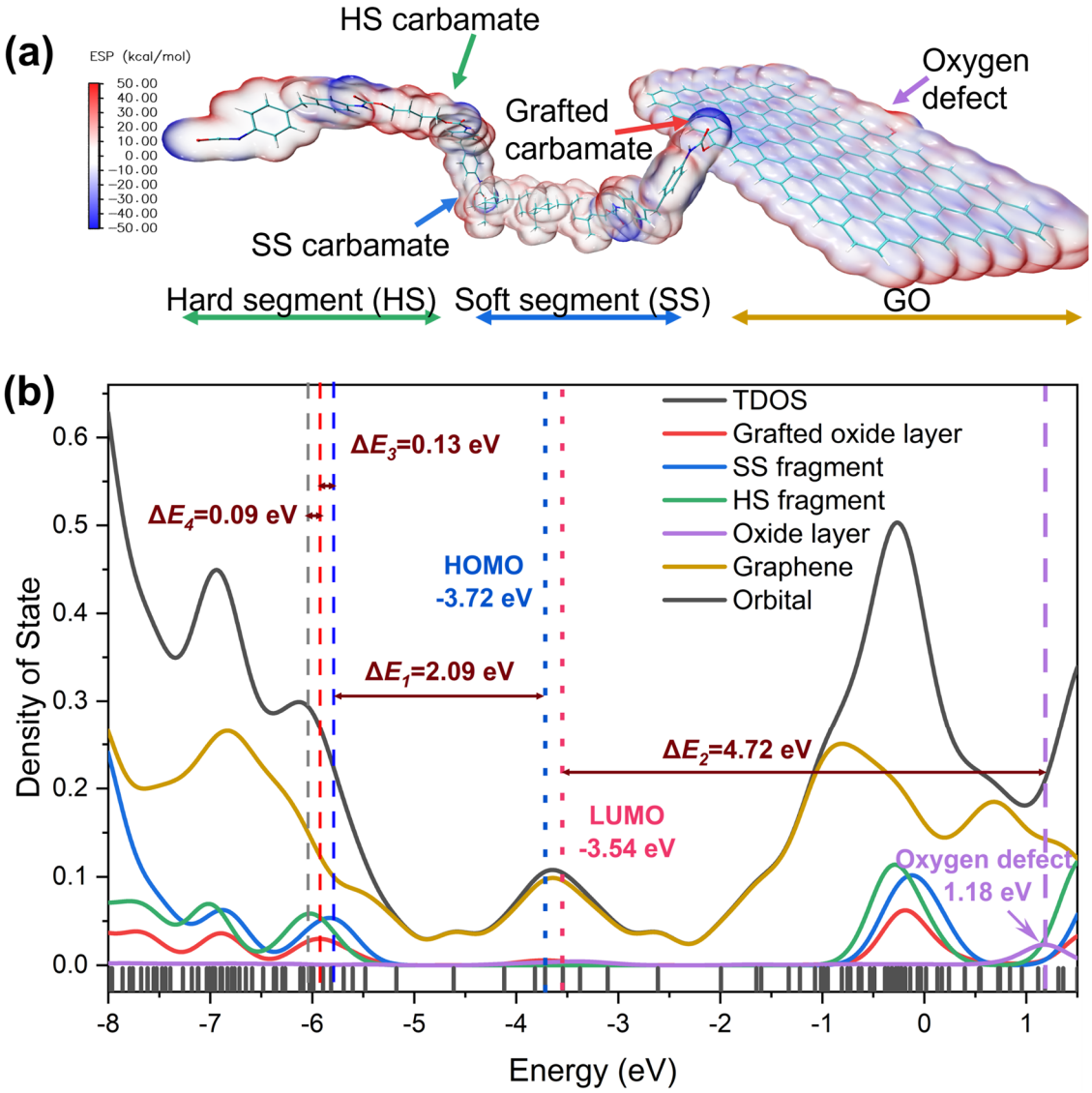

Figure 6-1: Quantum chemical calculations of grafted GO/PU nanocomposites. (a) The electrostatic potential mapping on the molecular surface of the repetitive unit obtained by quantum chemical calculations with a typical PU grafted GO fragment optimized in the minimum energy configuration. Red and blue colours represent positive and negative potentials, respectively. (b) Electron density distribution of the optimized molecular structure of PU/GO repeating units, including the total density of state (TDOS) and partial molecular fragments DOS.

6.2.2 Preparation of PU/GO Nanocomposites

In the schematic shown in Figure 6-2, monolayer GO nanosheets terminated with isocyanate groups are formed by the grafting reaction of hydroxyl groups with isocyanate group of MDI, followed by further polymerization of polyol to obtain a PU crosslinked molecular network with GO as the backbone. The first step requires the synthesis of isocyanate-grafted GO nanosheets. Graphene oxide (GO, obtained from Ashine) powder was firstly fed into dimethylformamide (DMF, anhydrous, obtained from Sigma-Aldrich) solution. The mixture was then stirred (2 hours) and ultrasonically dispersed (1 hours) to ensure that a well dispersed colloid was obtained, in which the GO nanosheets was effectively dispersed and unfolded. The GO dispersion was injected into a four-necked round-bottom flask (Figure 3-2 b) equipped with an anchor propeller stirrer, a funnel and a nitrogen inlet in an oil bath heated to 70 °C, followed by a slow addition of 4,4'-methylene diphenyl diisocyanate (MDI, obtained from Covestro) during the stirring process. The isocyanate-grafted GO dispersions (IGO) were produced after stirring under nitrogen atmosphere for 3 hours.

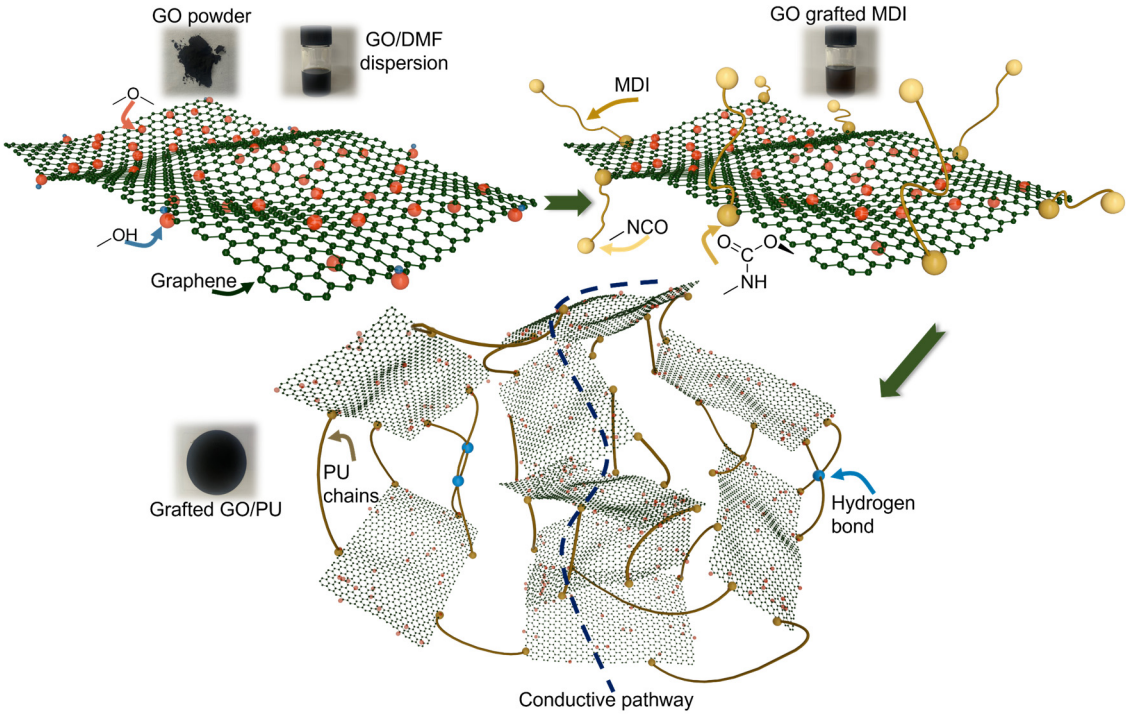

Figure 6-2: Schematic illustration shows the grafting reaction between GO and diisocyanate, where the GO surface reacts to produce MDI chain segments terminated with isocyanate groups, followed by further polymerization of polyol to obtain a PU crosslinked molecular network with GO as the backbone.

The previously designed PU2 is used as the self-healing polymeric matrix, referring to the preparation as described in section 3.2. In parallel to the grafted GO/PU nanocomposites to be synthesised, conventional blended GO/PU composites are also be synthesised for control experiments. For the solution blended GO/PU nanocomposites, the PU matrix was firstly dissolved by adding DMF solution. Then, A quantitative amount of GO/DMF dispersion was added to the prepared DMF/PU solution and further stirred for 1 hour and ultrasonically dispersed for 30 min to get a well-dispersed mixed solution. With grafted GO/PU nanocomposites, the polymerization reaction commences with the isocyanate-grafted GO nanosheets. The same equivalents of MDI as for the blending were used for the GO grafting reaction, followed by the addition of the corresponding equivalent of PPG to the flask and stirring at 400 rpm for 2 hours at 70 ℃. Immediately afterwards BDO was added dropwise to complete the chain extension reaction. Finally, same evaporation conditions and the sample hot-pressing techniques, as same as section 3.2, were applied to that grafted GO/PU solution and blended GO/PU solution to obtain thin film samples. A series of GO/PU nanocomposites doped with different volume fractions GO were prepared by solution blending and grafting, respectively. The PU matrix for both grafted and blended composites used same synthetic formulation of PU2 and the same amount of GO doping, where the GO doping is expressed as a volume fraction. For example, GGO_5 and BGO_5 refer to GO/PU nanocomposites doped by 5% volume fraction synthesized by grafting or solution blending, respectively. In this chapter, a series of GO/PU nanocomposites with different GO concentration and synthesis methods are prepared, such as GGO_0.25, GGO_1, GGO_5, BGO_0.25, BGO_1, and BGO_5.

The ordered evolution of the chemical composition of the material during the synthesis and the unfolding state of GO are determined in the next section.

6.2.3 Basic characterisation of PU/GO Nanocomposites

The first step in the synthesis of the desired composite is that it is necessary to demonstrate that the grafting reaction has been successfully carried out. The urethane generated by the reaction of the isocyanate with the hydroxyl group is a characteristic group in the FTIR spectrum to identify that the grafting reaction has produce the required product. However, as the final product GO/PU composites contain a large amount of

carbamate, isocyanate-grafted GO (IGO) as an intermediate product becomes critical in determining the success of the grafting reaction. As indicated in Figure 6-3, GO exhibits a distinct hydroxyl vibrational region from 3650 cm^{-1} to 2950 cm^{-1}. After the grafting reaction of GO with MDI, the content of isocyanate at 2260 cm^{-1} decreased, while the sample newly generated carbamate group with two characteristic regions, -NH at 3300 cm^{-1} and -C=O at 1700 cm^{-1}, proving that the isocyanate was effectively grafted onto GO nanosheets. There were not obvious difference of the blended/grafted GO/PU nanocomposites and pure PU in the FTIR spectrum. All three had significant convolution peaks of hydrogen-bonded carbonyl groups at 1705 cm^{-1}. The chemical composition of GO/PU nanocomposites is very similar to that of pure PU, both forming a distinct hydrogen bonding network, which facilitates the efficient self-healing capability of PU2 to be maintained in the composite.

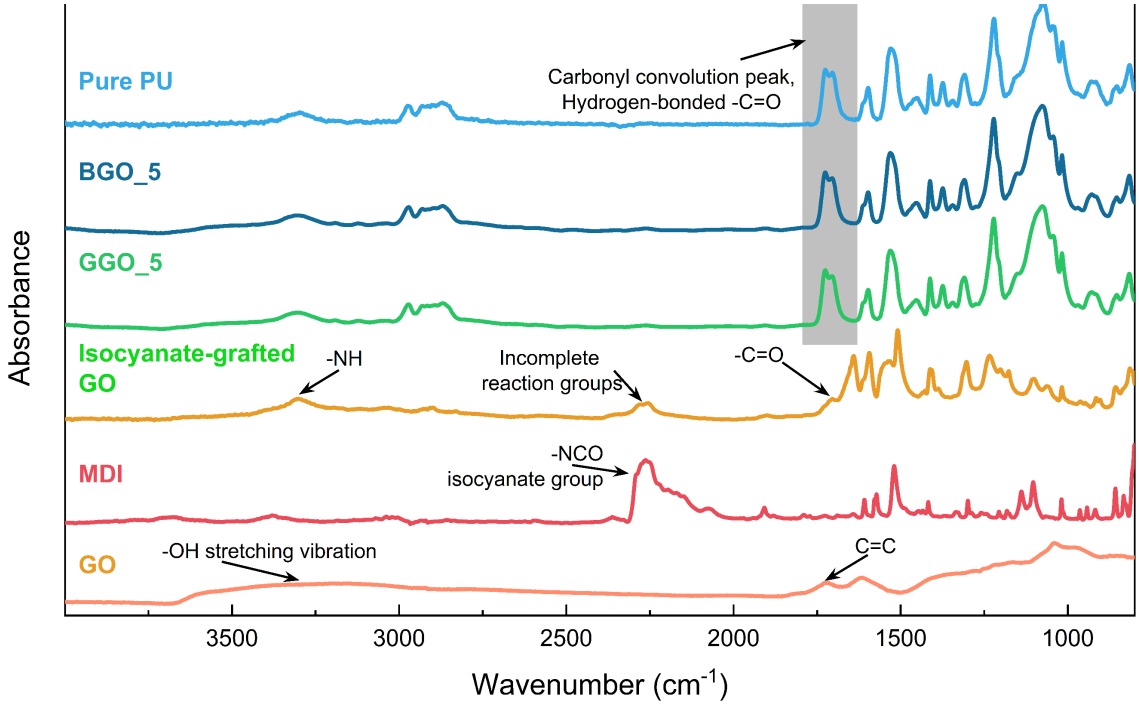

Figure 6-3: FTIR spectra of GO/PU nanocomposites during synthesis.

Another essential point is that the unfolded state of the GO nanosheets needs to prove identical in both grafted and hybrid GO/PU composites. In theory, GO is supposed to be a two-dimensional material that is fully extended in the polymer for optimum performance. However, in practice, GO easily forms collapses, folds, and other morphological changes within polymers due to its softness, ultra-high specific surface area, and the intermolecular forces. This multi-folded morphology is seen as a structural

defect in GO [194]. Although the same dispersion method was used for the mixed and grafted composites, it still needs to be verified experimentally whether the two composites have the same unfolding state. The same drop coating and heat treatment methods as in section 3.3.3 were employed to fabricate the ultra-thin film samples for AFM observation. The unfolding states of GO nanosheets in grafted and blended nanocomposites is shown in Figure 6-4. Due to the special characteristics of 2D materials, the morphology of GO in 3D matrix cannot be directly observed by conventional methods. Therefore, by using the same ultra-thin film preparation techniques, AFM can reflect the unfolding state of GO in grafted and blended GO/PU to some extent. It can be assumed that GO is well dispersed and unfolded under this preparation technique if no obvious folding, wrinkling, and agglomeration of GO sheets are observed in the AFM images. It is clear that the GOs of the grafted and blended materials possess similar areas of unfolding in the AFM graph. This section confirms that the nanoparticle dispersion methods used are effective and that the GO dispersion states of the blended and grafted GO/PU nanocomposites are similar, the only difference being the interfacial state between the GO sheets and the PU matrix.

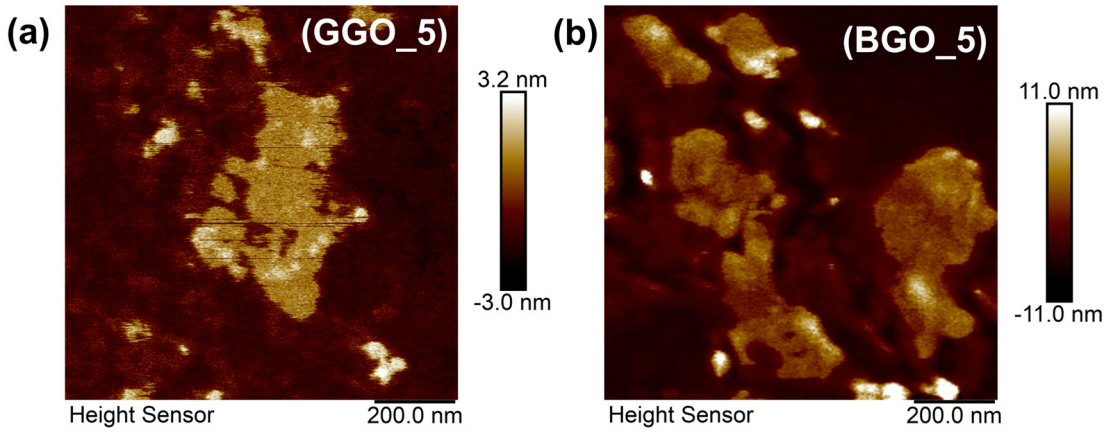

Figure 6-4: The unfolding states of GO nanosheets in grafted (a) and blended (b) composites obtained by AFM, respectively.

6.3 Nonlinear Electrical and Dielectric Behaviour of GO/PU Nanocomposites

Nonlinear electrical and dielectric behaviour is critical to achieve self-adaptive function for resistive or capacitive field grading. This section examines detailed

characteristics of grafted and blended samples and compares the differences between the two.

6.3.1 Nonlinear Electrical Behaviour

Same conductivity testing system as described in section 3.3.6 was used for measuring the nonlinear electrical conductivity of GO/PU nanocomposites. The measurements were performed on the samples with a thickness of 200 μm and with 0.5-15 kV/mm DC electric field applied. The interval of electric field for each measurement was 0.5 kV/mm.

The measurement result of the nonlinear current characteristics of GGO_5 is shown in Figure 6-5. When the field strength exceeds 2kV/mm, the current growth rate of GGO_5 slows down significantly and gradually approaches the saturation current. When the applied field strength is high enough to help the charge to overcome the interfacial barrier between the GO nanosheets, the conduction current of GO/PU nanocomposites reaches saturation. The field strength-current measurements of GGO_5 at 0-3 kV/mm are sufficient to describe the nonlinear current characteristics of the material, so the current response of the material at more than 3kV/mm will not be further measured.

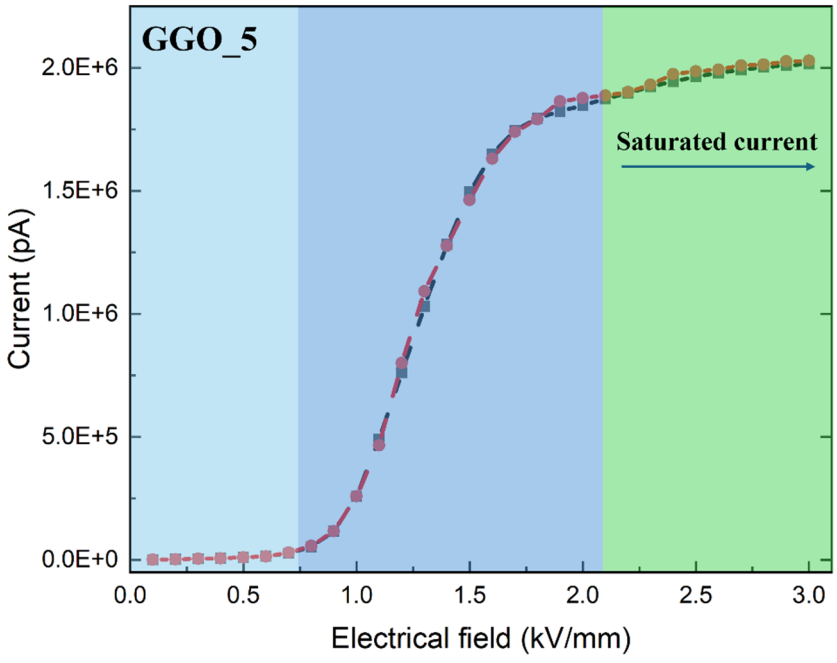

Figure 6-5: Nonlinear current properties of GGO_5.

Figure 6-6 (a) shows the curves of the current density (*J*) of the composites as a function of electrical field strength (*E*). When the concentration of GO is below the percolation threshold [134], the composites do not exhibit nonlinear conductivity characteristics and the conductivity is lower than that of pure PU, which may be related to the "deep trap" effect introduced by GO. Both BGO_5 and GGO_5 display significant nonlinear conductivity characteristics. E_b and nonlinear coefficient α are the most important parameters for GO/PU nanocomposites' nonlinear performance. E_b is defined as the switching above which the material begins to show a rapidly changing conductivity or permittivity. In terms of the nonlinear coefficient α, it is the slope of *J(E)* curve (in logarithmic coordinate) and reflects the degree of effect of electric field on material parameters. Compared with the nonlinear electrical behaviour of BGO_5, the saturation current of GGO_5 increased by 2000% from 3.1E-10 A/cm^2 to 6.3E-9 A/cm^2, the nonlinear coefficient (α) improved by 200% from 2.3 to 4.7, and the switch field decreased from 8.5 kV/mm to 0.7 kV/mm. The nonlinear electrical properties of grafted GO/PU nanocomposites are much better than those of blended nanocomposites. Theoretically, the saturation current of composites is determined by the percolation channels constructed by GO, but the nonlinear conductivity response depends on the oxidation state of GO and its interfacial state with the matrix. The *J(E)* characteristics of the composites at different temperatures are reflected in Figure 6-6 (b). Increasing temperature can effectively increase the probability of the carriers to hop over a certain height of the potential barrier. Since the current increase of pure PU under the same thermal stimulation is not distinct, it can be confirmed that the on-state current measured of BGO_5_45 ℃ is contributed by the percolation pathways established by GO. Consequently, the interfacial state between GO and polymer matrix plays a critical role in the nonlinear electrical performance of the composites under similar construction of the percolation channels.

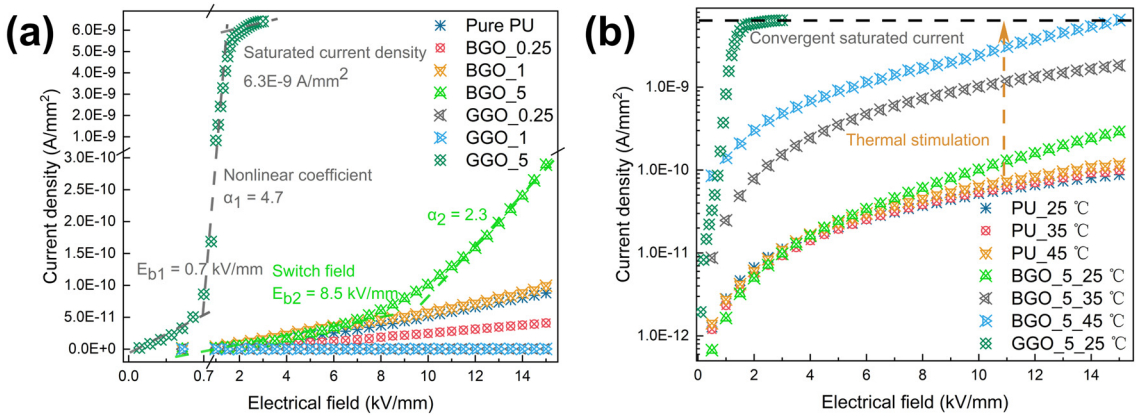

Figure 6-6: (a) Nonlinear current density *J* (versus electrical field, *E*) characteristics of GO/PU nanocomposites with different concentrations of GO prepared by solution blending or grafting. (b) *J(E)* characteristics of blending 5 vol. % GO/PU and pure PU with increasing temperature.

6.3.2 Nonlinear Dielectric Behaviour

A vertically biased electric field was incorporated into the Novocontrol DRS measurement system described in Section 3.3.7 to investigate the non-linear dielectric response of the composite material under electric field induction. The measurements were carried out at three temperature points of 0, 25, and 50 ℃ with the frequency from 1 Hz to 10^4 Hz, while a bias voltage from 0 to 1 kV was applied at each measurement to reflect the nonlinear response of the materials. The thickness of the measured sample is 200 μm and the diameter of the measuring electrode is 2 cm.

GGO_5 exhibits nonlinear dielectric response at various temperatures that can be applied for capacitive field grading, as shown in Figure 6-7 (a) and (b). The dielectric constant of pure PU is generally higher than that of the blended composites and lower than that of the grafted composites. The interfacial interaction formed by the grafting method is helpful in enhancing the polarization ability of the composites, while blending GO will limit the polarization behaviour of the composites. Capacitive field grading is also based on the nonlinear permittivity properties of the material. When the applied field strength exceeds a certain threshold, the dielectric constant of the material undergoes a surge. Thus, the field strength in that region of the material is suppressed. Figure 6-7 illustrate that both temperature and field strength are ways to bring a material to threshold. At both low temperature, high field strength or high temperature, low field strength, the material achieves a nonlinear surge in permittivity. GGO_5 provides a large increase in

permittivity in the region of high field strength and low frequencies. The area of this nonlinear permittivity region expands continuously with increasing temperature. In contrast, there is no obvious nonlinear dielectric response of BGO_5 under low temperature, especially in the temperature interval below the glass transition temperature (T_g). In the high-temperature region, BGO_5 shows a high permittivity response in the low-frequency and high-field region because the increased thermal energy increases the probability of charge being successful in leaping over the interfacial barrier, which is similar to its nonlinear electrical behaviours.

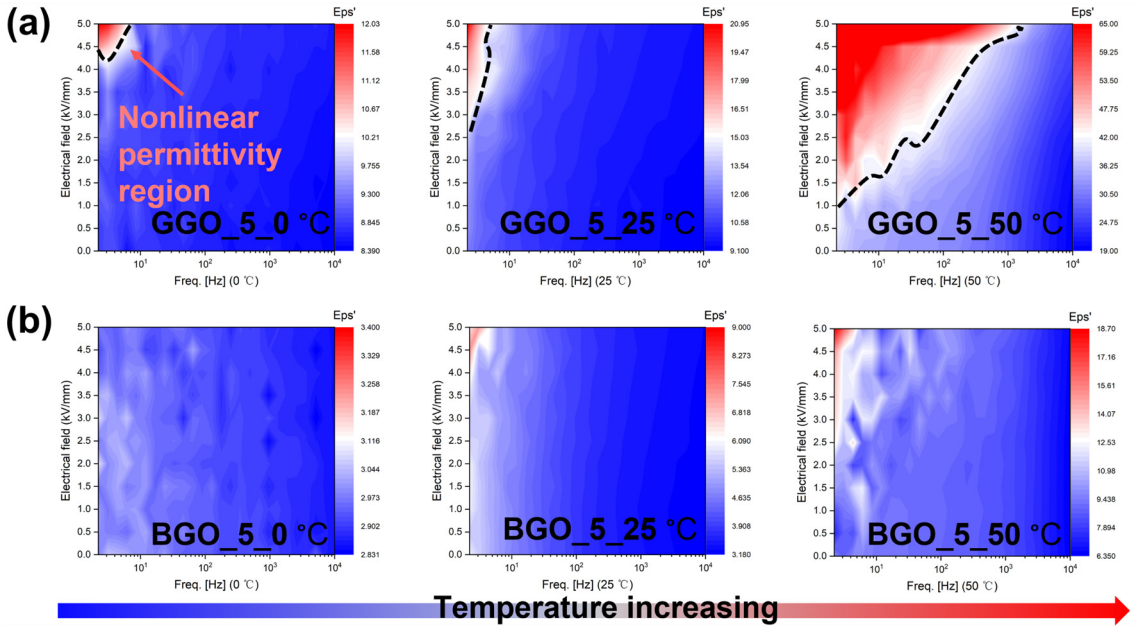

Figure 6-7: Mappings of permittivity of grafted (a) and blended (b) GO/PU nanocomposites with frequency and bias voltage at different temperatures, separately.

6.4 Charge Transport at the GO/PU Interface

The previous section demonstrated that the different interfacial states of the GO and PU matrices in the two materials are responsible for the large difference in electrical and dielectric performance between the grafted and blended GO/PU nanocomposites. In this section, the influence of the interfacial interaction of GO/PU on its charge transport behaviour will be investigated in detail from the nanoscale to the macroscale. In order to reveal the charge transport mechanism of GO/PU nanocomposites with nonlinear electrical properties, 5% concentrations of blended and grafted GO/PU nanocomposites were investigated in this section.

6.4.1 Interfacial Charge Transport at the Nanoscale

The combined EFM (electrostatic force microscopy) and KPFM (Kelvin probe force microscopy) techniques are widely used to construct nanoscale mapping of charge transport properties on material surfaces by measuring electrostatic interactions between AFM (atomic force microscopy) tip and the sample [195], [196]. Instead of the previous conventional AFM tests, in this combined EFM-KPFM test the sample requires to be as thin as possible to prevent the stacking of multiple layers of GO and then, the substrate must be conductive in order to ground one side of the sample. A 5 mg/mL sample solution was spin-coated onto a highly conductive gold-plated wafer on a spin-coater (Setcas KW4E) at 3000 rpm/s to obtain an ultra-thin film with a thickness of about 10 nm for EFM and KPFM measurements. The obtained GO/PU film is shown in Figure 6-8 (a). The bright speckles in a wide range of height images (Figure 6-8 b), the "bumps" of the surface, are generally identified as GO nanosheets. The corresponding dark areas are considered as the polymer matrix.

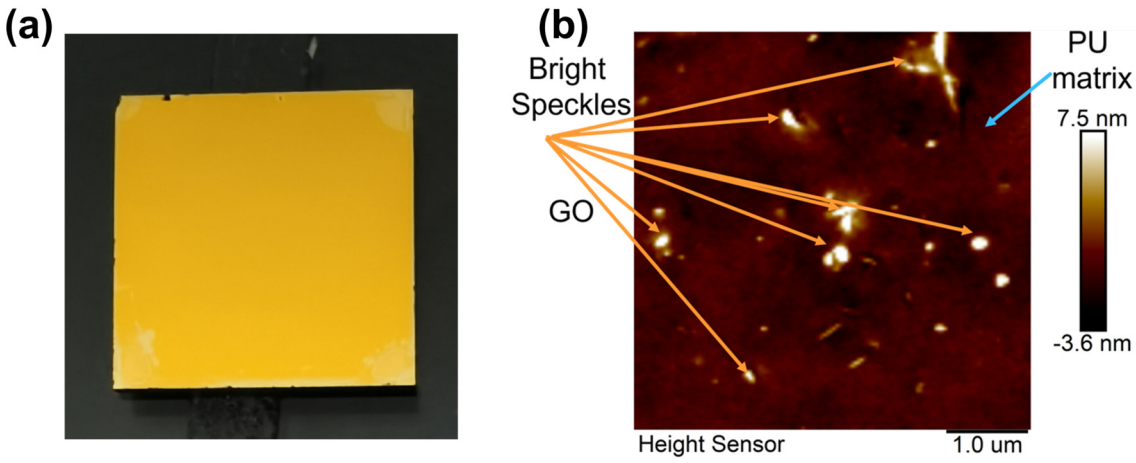

Figure 6-8: (a) Spin coating GO/PU film on conductive gold-plated wafer. (b) AFM height image of GO/PU nanocomposites at 5 × 5 µm size.

Two similar tested zones in BGO and GGO with adjacent GO sheets separated by about 200 nm were positioned respectively and scanned in a 2 × 2 µm region for height images, as indicated in Figure 6-9 (a-1,) (b-1). The initial surface potential distribution of the samples under the grounded surface is not visibly affected by its irregular morphology, as can be confirmed in Figure 6-9 (a-2) (b-2). Charge was injected into a highly conductive region of 200 × 200 nm on the one of GO sheet by applying a DC voltage of 10 V to AFM probe in contact mode. Subsequently, the voltage on the probe

was withdraw and switched to the tapping mode of KPFM to scan a wider range of surface potentials. The probe was scanned continuously at an average rate of 5 min for one potential mapping until the charge distribution tends to stabilize. The effect of the interface on charge transportation is investigated by observing the spontaneous migration and diffusion of charge. Since the scan time of a potential image is 5 min, Figure 6-9 (a-3) (b-3) are regarded as the initial surface charge distribution of the samples after charge injection. After 60 min of charge migration and diffusion, there are utterly different mapping of charge distribution for blended and grafted samples despite having the same charge injection conditions, as exhibited in Figure 6-9 (a-4) (b-4). In the case of BGO_5, the interface between the conductive graphene layer and the PU matrix appears to form a "wall" that traps the injected charge on the individual GO sheet. Conversely, the injected charge of GGO_5 crosses the interface between GO and matrix, while transporting charge in the direction of the adjacent GO sheets. On the condition of same test parameters, environment, and process, the interfacial charge transport behaviour of the blended GO/PU and grafted GO/PU nanocomposite showed significant differences. The charge transports from one GO sheet to another GO sheet in the GGO_5. However, BGO_5 significantly hindered the charge transport between GO sheets. The phenomenon is mainly attributed to the difference between interfacial barriers of the two samples. The tailored interfacial barrier of the grafted GO/PU nanocomposites facilitate charge transport between the adjacent GO sheets, the so-called percolation channels, while the high energy barrier of the blend composites hinders the transporting process.

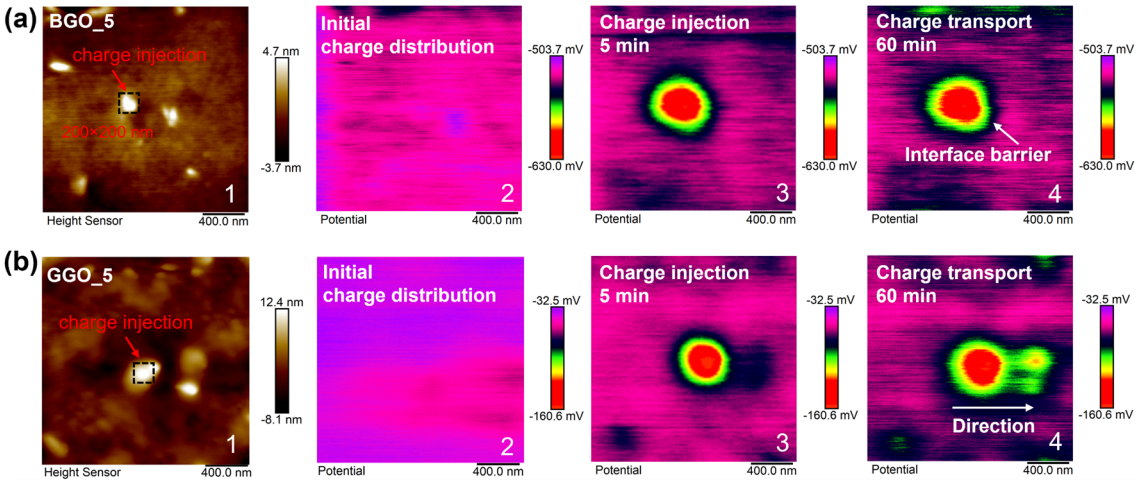

Figure 6-9: Characterization of GO-PU interfacial effects at mesoscopic scales. Height image in 2 × 2 µm region of GGO_5 (a-1) and BGO_5 (b-1) obtained by AFM. Initial surface potential mapping without charge injection of

GGO_5 (a-2) and BGO_5 (b-2) obtained by EFM-KPFM. (a-3,4) and (b-3,4) are the mapped charge distribution of the composites at 5 min and 60 min after charge injection through the conductive probe.

6.4.2 Macroscopic Interfacial Effects

The mechanism of interface on charge transport is not only characterized at the mesoscopic nanoscale, but also reflects the macroscopic interfacial effects in composites through thermal stimulation depolarization current (TSDC) method. DSC measurements were performed on the samples, and the results are shown in the Figure 6-10 to support the TSDC analysis of the composites.

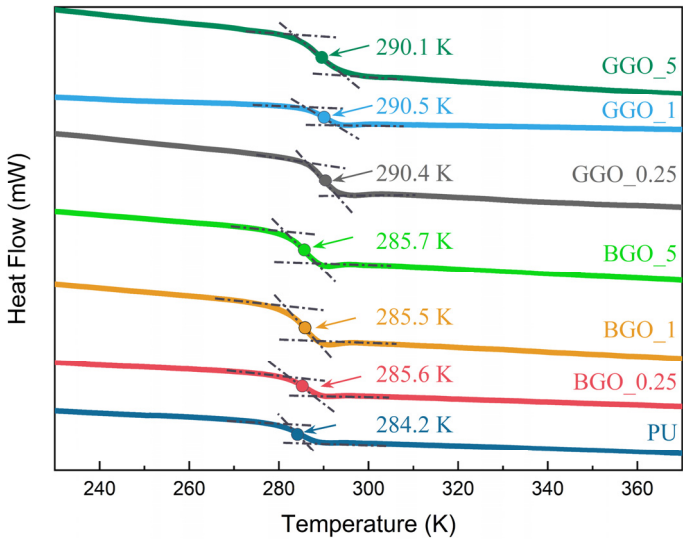

Figure 6-10: DSC results and labelled glass transition temperatures (T_g) of GO/PU nanocomposites.

The original TSDC curve and peaks fitted to two Gaussian functions are presented in Figure 6-11 (a), (b), and (c). The relaxation peak located near the glass transition temperature T_g is the α relaxation of the material. The second higher temperature peak is generally considered to be a Maxwell-Wagner-Sillars (MWS) interfacial relaxation, with the difference that the interfacial relaxation comes from the phase separation interface for pure PU while it mainly originated from the interface between the GO and polymer for composites. Each discrete current peak can again be described by the first order kinetic equation of TSDC, in which case the corresponding activation energy and charge density can be obtained from any three points on the peaks (equation 3.5). The calculation results of the quantity of charge and activation energy corresponding to each relaxation type are listed in each figure. There is not an obvious difference in the activation energy of α relaxation in pure PU and its composites, which is related to the

fact that the doping content of GO is only 5 vol. %. However, the doping of GO introduced a large amount of interfacial charge to the composites, with ratio of charge as high as 90%. At the same time, the energy level of interfacial relaxation is 1.08 eV for the blended materials, while that of the grafted materials is only 0.87 eV, which is closer to the energy level of α relaxation. Local states with deeper energy level are generally considered to be detrimental to charge transport in dielectrics [185]. The TSDC results are consistent with the macroscopic conductivity and KPFM results. By adjusting the interfacial energy barriers, GGO_5 obtains a superior nonlinear electrical response than that of BGO_5.

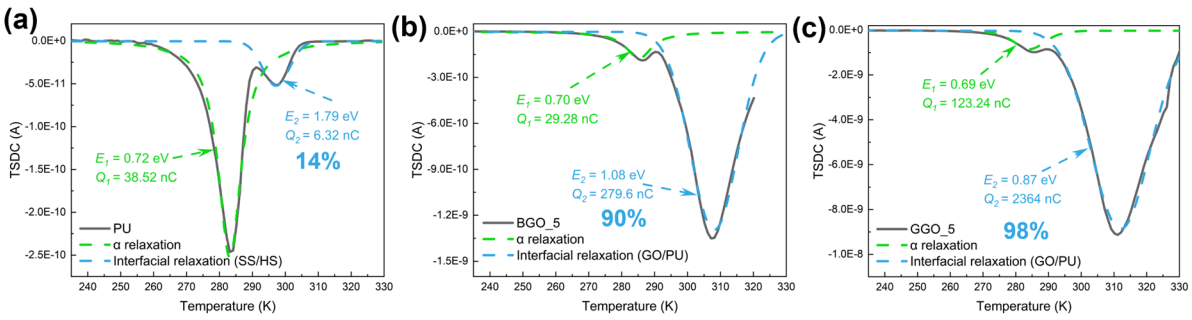

Figure 6-11: TSDC spectrum and peak fitting results of (a) pure PU, (b) BGO_5, and (c) GGO_5, where the calculated values of activation energy *E* and charge *Q* for each type of relaxation are listed.

The grafting method can autonomously pull down the energy level of the interfacial barrier to make it closer to the energy level of the main chains. This interfacial modulation approach has been shown to be an effective method for constructing efficient percolation channels from three aspects: simulation, mesoscopic, and macroscopic, thereby, achieving excellent nonlinear electrical and dielectric response of the grafted GO/PU nanocomposites.

6.5 Organic Integration of Self-healing and Self-adaptive Functions

In this section, the grafted GO/PU nanocomposites will be applied to an electrode structure with a typical distorted electric field for checking its self-adapting capability to electric field. Also, the expected self-healing capability of the composites will be verified under this structure, including the recovery of this novel electrical behaviours and the repair of the structure.

6.5.1 Self-Adapting Grafted GO/PU Nanocomposites Applied to Typical Distortion Electric Field at Triple Junction

In order to intuitively characterize the reversible capability of the nonlinear electrical behaviour of grafted GO/PU nanocomposites, meanwhile, simulating the potential application scenarios as much as possible, an electrode structure is designed with triple junction as shown in Figure 6-12. Triple junction, the interfacial junction between the electrodes and two or more dielectrics, is considered to be the critical structure that triggers the local field distortion, which is widely found in various electronics packaging [135], or power transmission apparatus [136]. Two copper electrodes are pressed parallel and tightly in the centre of the surface of a GGO_5 sample with a thickness of 1 mm, with a spacing of 10 mm between the electrodes. The triple junction is located at the junction of the electrodes, the air, and the sample, indicated in Figure 6-12. The external loop of the electrodes corresponds to the conductivity measurement system described in Figure 3-6. One electrode is connected to a high voltage power supply and the other electrode is connected to an electrometer to record the output current. The entire electrode system is placed in a thermostatic oven that is used to maintain the temperature during current testing and to provide the thermal stimulation required for healing. As shown on the right side of Figure 6-12, there are three stages in the self-healing test. In the initial stage, the E-I properties of the system are measured under an applied voltage of 0-4 kV. In the damage stage, the sample is cut by a knife to make a crack along the middle of the electrodes. In the subsequent healed phase, the crack of the sample closes after light or thermal stimulation, at which point the E-I properties of the sample are measured again. The measurement results of this GGO_5 sample after multiple damage-heal cycle are listed in the next section.

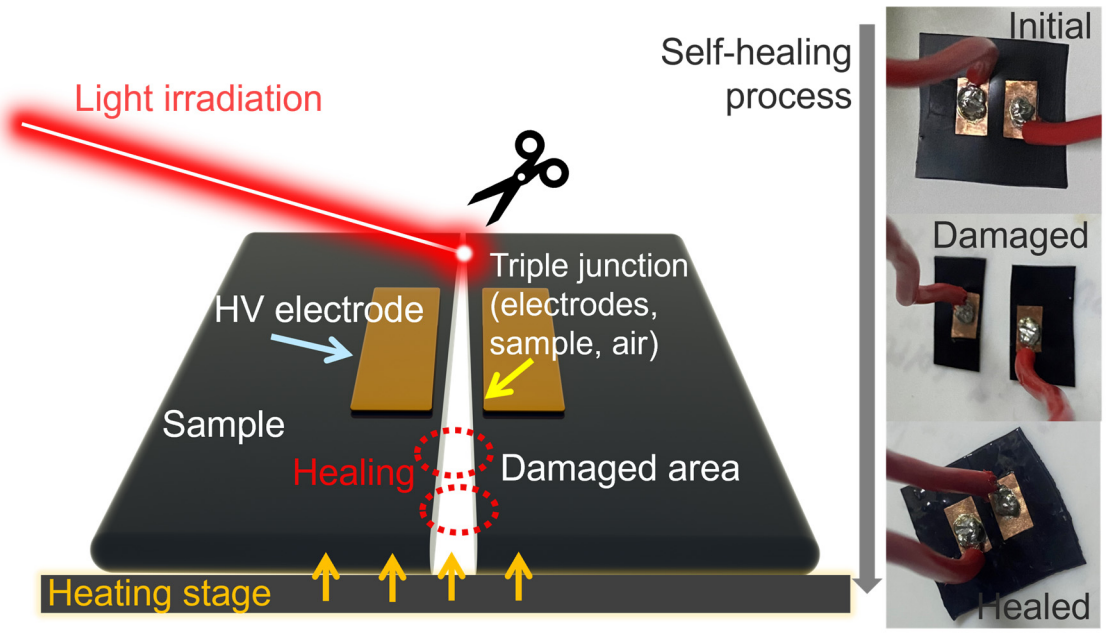

Figure 6-12: Schematic diagram of the designed electrode structure with triple junction and the self-healing process, in which two stimulation ways, thermal healing, and light irradiation, are carried out respectively.

A 3D axis-symmetric finite element model is set up to simulate the condition of the designed electrode structure. The electric field distributions in different conditions are discussed and the field grading effect of the nonlinear materials GGO_5 is illustrated. This electrode model is set up in COMSOL Multiphysics. The two plane electrodes, with a size of 10.0 mm×5 mm×0.055 mm (length, width and height), is put on the GO/PU sample and the system is put on a PTFE platform. The distance between the two electrode is 10 mm. The dimensions of the geometry constructed in the simulation model correspond to the dimensions of the actual electrodes in Figure 6-12. The conductivity of the plate electrodes and PTFE is set to 6.0×10^{7} S/m and $2.8\times1e^{-12}$ S/m, respectively. In order to better compare the results of the calculations, the fineness of the meshing is kept consistent.

The J-E curve of GGO_5 in Figure 6-6 (a) is the nonlinear conductivity data obtained from experiments, which is set as the conductivity parameter of the nonlinear sample in the simulation model. 1.75E-11 S/m is set as the conductivity parameter of the linear sample, which is used for the comparison of electric field distributions under the application of the model to the linear sample and the nonlinear material, respectively.

The result of electric field distribution is shown in Figure 6-13 (a), when 3.0 DC kV is applied to the left electrode and the electric potential of the other electrode is set as 0. The triple junction produces significant electric field distortions with maximum field strengths as high as 21.2 kV/mm in the case of applying the linear sample, as indicated in Figure 6-13 (b). In contrast, the application of the nonlinear material successfully reduces the maximum field strength at the triple junction to 4.4 kV/mm, with a suppression rate of 79.2%. The nonlinear electrical properties of GGO_5 show remarkable self-adaptive field grading capability, which effectively suppress the electric field distortion at the triple junction. In addition, the ability of the nonlinear material to suppress the electric field in space depends on whether the electric field strength in each direction reaches the switching field strength (E_b) of the material. Ideally, the larger electric field strength in a certain direction, the stronger the electric field suppression ability of the nonlinear material. The tangential electric field strength is significantly larger than the normal electric field in this simulation model. Hence, the tangential electric field strength of the electrodes can be decreased by this nonlinear material.

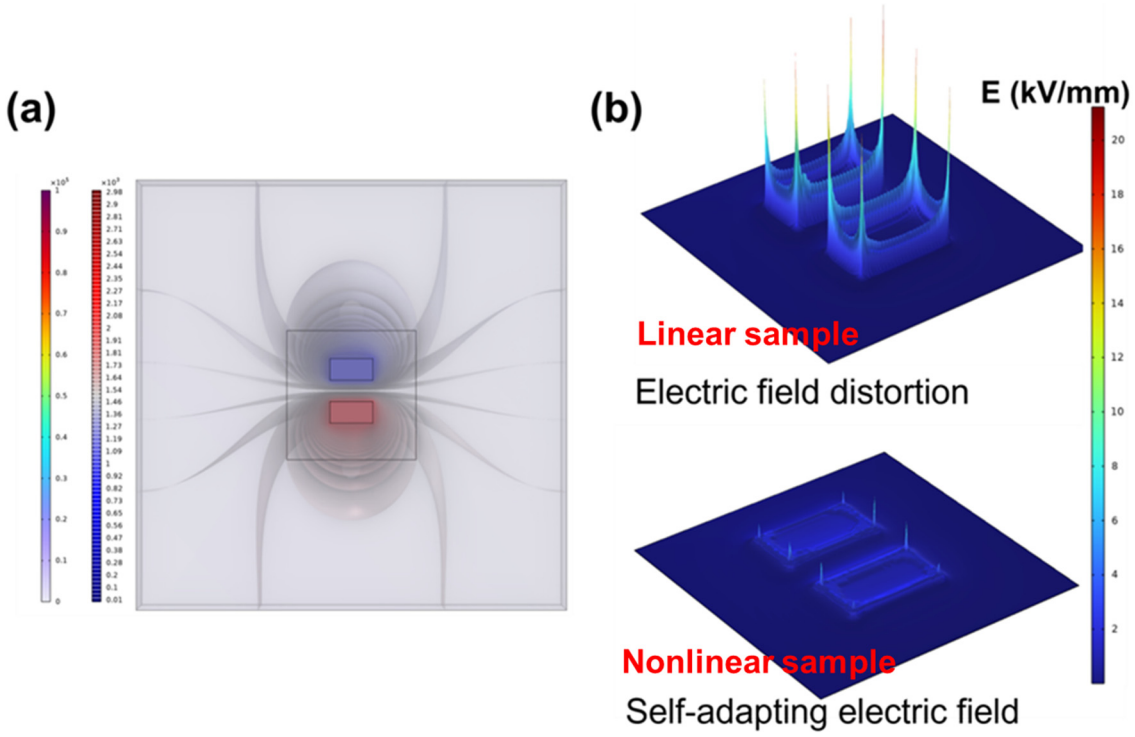

Figure 6-13: (a) Electric distribution of designed electrode structure. (b) Simulation results reflecting the self-adaptive ability of the nonlinear electrical behaviour of GGO_5 to a typical distorted electrical field.

6.5.2 Self-Healable Self-Adaptive Electrical Behaviours of GO/PU Nanocomposites

Based on this designed electrode structure, the self-healing ability of the GO/PU composite will be verified in this section.

Two different healing approaches, heating at 60 ℃ in a thermostatic oven for 60 min and NIR (near-infrared) light irradiation (2000DL-AL, Tengxing Photoelectric Technology) with 1 W/cm^2 at wavelength of 808 nm for 30 min, were used to repair a sheared-out crack located in the middle of two electrodes. The right side of Figure 6-12 indicates the photographs of the nanocomposite at different stages of the self-healing process. GO is known to possess excellent photothermal energy conversion capabilities, where the thermal energy converted by the absorption of NIR light can be applied as energy to drive the self-healing of the polymer matrix [197], [198], [199]. Figure 6-14 (a) demonstrates the conductivity characteristics of the grafted composites with different GO concentrations before and after crack healing obtained by two different repair methods. Here, the self-healing efficiencies can be defined as:

$$Healing\ effciency\ (\%) = \frac{Strength_{after\ \text{healing}}}{Strength_{initial}} \times 100\% \tag{6.1}$$

Where "strength" depends on the evaluation criteria, can be a non-linear coefficient, saturation current, etc.

The new light healing mechanism for composites introduced by GO allows just 0.25 vol.% of GO to surge the light-stimulated healing efficiency to nearly 80%. The light healing efficiency gradually increases with further growth of GO concentrations, approaching the heating healing efficiency (95%). Predictably, faster, and more targeted light healing can greatly broaden the application landscape of grafted GO/PU nanocomposites. The exciting nonlinear electrical behaviour of GGO_5 was restored well after healing. Additionally, a 5-time damage-healing cycle test was conducted to examine the repeated self-healing capability of the composite (Figure 6-14 b). The self-healing efficiency of GGO_5 evaluated by saturation current density remained higher than 92% after 5 cycles, evidencing that the percolation pathways connected by GO were well maintained after multiple healing cracks. The nonlinear coefficient of GGO_5 retains the healing efficiency of 86% after 5 thermal cycles, although this slight decline may be due to thermal aging of the sample.

The self-healing performance of the mechanical strength of the composites was also investigated. Cracks were caused by a knife in the centre of barbell samples of grafted GO/PU nanocomposites with different GO doping content. The healed samples were obtained after heating and lighting treatment, respectively. The images and stress-strain curves of different sample before and after self-healing are shown in Figure 6-15 (a) and (b). The grafted GO/PU composites all show good self-healing efficiency in terms of tensile strength, regardless of light irradiation or heating, of over 90%, similar to the results of the electrical property tests. The introduction of GO also improves the tensile strength of the composite to a certain extent, thereby extending the range of potential application scenarios.

Taking advantage of the excellent self-healing capacity of the PU2 matrix, as confirmed in section 5.5, the low concentration of 5 vol% of grafted GO nanosheets did not negatively affect the healing efficiency. On the contrary, a new means of light healing was also introduced in the GO/PU composites. So far, the smart dielectric with simultaneous self-healing and self-adapting capabilities was successfully synthesised and demonstrated.

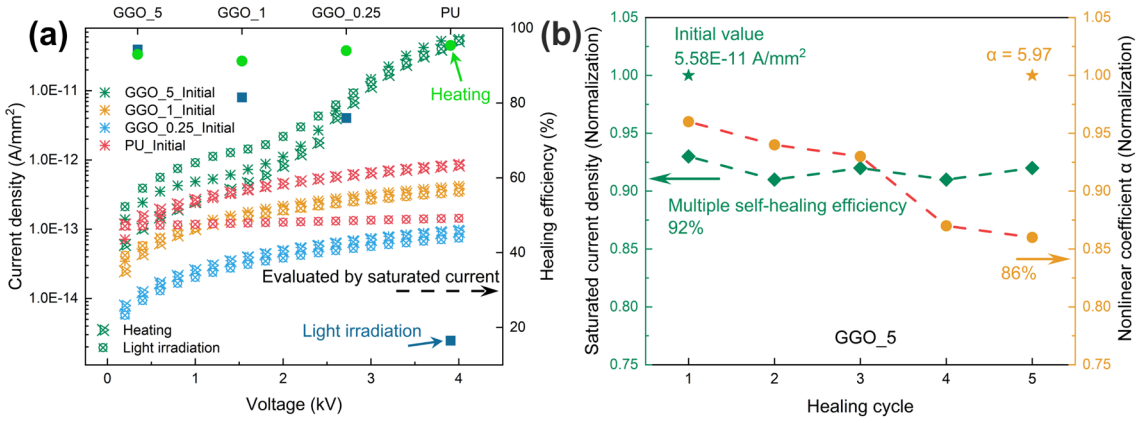

Figure 6-14: Self-healable nonlinear electrical response of GO/PU nanocomposites. (a) Current density curves with different applied voltages of the grafted GO/PU nanocomposites before and after healing by heating or light irradiation, separately, as well as the healing efficiency of different healing methods and different materials evaluated in terms of saturated current are also labelled in the figure. (b) Multiple self-healing capability of the nonlinear electrical properties of GGO_5 evaluated in terms of saturated current and nonlinear coefficient.

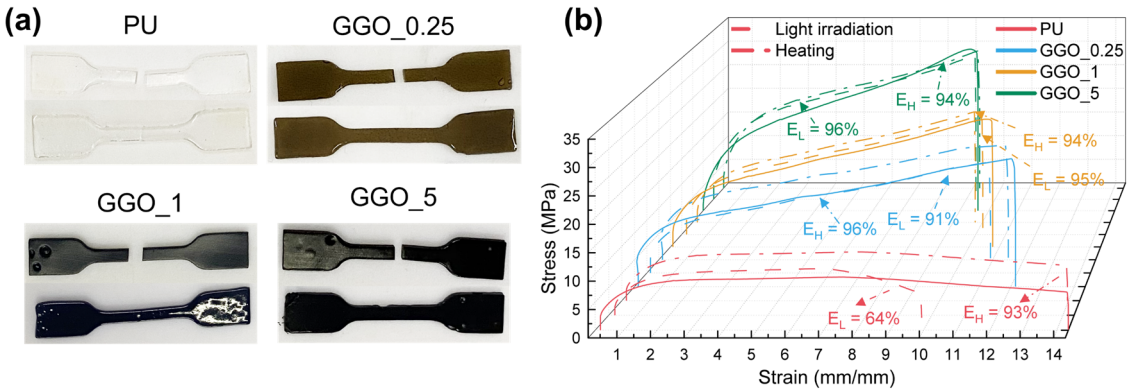

Figure 6-15: Structural self-healing of GO/PU composites characterized by tensile tests. (a) images of composites before and after healing. (b) Strain-stress curve before and after healing by heating or light irradiation, respectively.

6.6 Summary and Conclusions

A grafted GO/PU nanocomposite with simultaneous self-healable and self-adapting electrical and dielectric behaviours was successfully designed and implemented in this chapter.

In the section 6.2, a series of grafted and blended GO/PU nanocomposites with different concentrations were designed and prepared, while the correctness of the synthesis process was correspondingly characterized. Firstly, the interfacial barrier between the carbamate bonded GO and PU chains was significantly reduced after grafting, according to quantum chemical simulations. A “bottom-up” synthetic strategy was applied by grafting isocyanate to the hydroxyl group on the sides of GO, followed by further polymerization of the polyols and diols with the isocyanate on the graft chain to obtain a reversible hydrogen-bonded polyurethane network with GO as the backbone. A batch of blended GO/PU composites are also be synthesised for control experiments. The successful grafting reaction was verified by FTIR, whilst the similar unfolding state of GO nanosheets in the grafted and blended composites was also confirmed by AFM.

The nonlinear electrical and dielectric behaviour of grafted and blended GO/PU nanocomposites were investigated in the section 6.3, where the grafted composite with 5% volume fraction of GO exhibits superior nonlinear electrical behaviour with a switching field strength of 0.7 kV/mm, a nonlinear coefficient of 4.7, and a saturation

current of 6.3 nA/mm^2, which are much better than those of the blended composite with the same GO concentration and satisfy the demand for self-adaptive resistive field grading materials for most engineering applications. The grafted composite also features a nonlinear dielectric response that allows it to be utilized as a capacitive field grading material.

Section 6.4 illustrated the mechanism by which the interfacial state affects the charge transport behaviour of GO/PU nanocomposites. It is demonstrated by the combined EFM and KPFM techniques that the interface between the GO and the matrix of the blended composite forms a "wall" that blocks charge transport along the percolation channels connected by GO sheets. Conversely, the injected charge in the grafted material distinctly prefers to migrate between adjacent GO sheets. The interfacial barrier between GO and the matrix is considerably lowered to a level comparable to that of the polymer chains after grafting, thus reducing the energy dissipated by the charge flow through the GO percolation channel, as confirmed by both quantum chemical calculations and thermally stimulated current results. This improved nonlinear characteristic of the grafted composite is mainly attributed to the tailored interface between GO and PU matrix.

The self-healing and self-adaptive capabilities of organic integration in grafted GO/PU composites were demonstrated in section 6.5. An electrode structure with a typical distorted electric field was designed. Using finite element simulations, the maximum distortion field of the system at an applied voltage of 3 kV was reduced by 79.2% after the application of GGO_5 with good nonlinear electrical properties, thus achieving excellent adaptive electric field capability. Meanwhile, the grafted GO/PU nanocomposites reveal repeatable self-healing capabilities based on the reversible hydrogen bonding network, involving the recovery of its novel nonlinear electrical properties and structural restoration. A brand-new and more efficient light healing method for the composite caused by the photothermal effect of GO compared to heating healing broadens the application scenario of self-healing. This work is the first organic integration of electrical and dielectric self-adaptive and self-healing functions, promising to be designed and fabricated for next-generation electrical insulation. The functional material is expected to increase the reliability of HV insulation through the self-adaptive

function, reduce local electric field distortion, and extend the service life of equipment by healing the damage under suitable light or thermal stimulation conditions even after an obvious failure.

Chapter 7 Conclusions and Recommendations for Future Work

7.1 Summary and Conclusions

This thesis designed and demonstrated a bioinspired dielectric material with simultaneously self-healing and self-adapting electrical and dielectric behaviours for next-generation electrical insulation. A phase-separated polyurethane (PU) elastomer with robust dielectric strength was initially developed as the self-healing polymer matrix. The relationship between the microstructure and macro-properties of PUs was investigated in detail utilising quantum chemical simulation, chemical-physical structure characterisation and molecular relaxation behaviour to instruct the preparation of the desired PU materials. The significant origins of the self-healing capability of the designed PU were confirmed to be its reversible hydrogen bonding network and the efficient shape memory effect evaluated by conformational entropy. At the same time, the self-healing performance of the designed polyurethane under electrical damage was evaluated from several perspectives, including the structural healing of damaged areas in multiple dimensions and the recovery of its insulating properties. Subsequently, isocyanate grafted graphene oxide (GO) was introduced into the self-healing PU matrix with the purpose of enabling the nanocomposite to acquire self-adaptive capabilities. The interfacial barrier between GO and the matrix was considerably reduced to a level comparable to that of the polymer chains after grafting, resulting in superior nonlinear electrical and dielectric behaviour of the composites, as confirmed by both quantum chemical calculations, combined EFM and KPFM tests and TSDC. The application of this grafted GO/PU nanocomposite exhibited excellent self-adaptive field grading capability on the designed electrode structure with typical electric field distortion. The repeatable self-healing function of the grafted GO/PU nanocomposites, including the recovery of nonlinear electrical properties and structural restoration, was exhibited together. For the first time, self-adapting and self-healing functions were integrated organically into an insulating material, promising improved reliability, and lifetime for next-generation HV equipment.

Chapter 2 of this thesis reviewed self-healing and self-adapting dielectric materials in terms of the significance, principles, and their development in high voltage electrical insulation. Innovations in insulation materials are indispensable for manufacturing advanced power equipment. Smart dielectric materials, represented by self-healing and self-adaptive materials, contribute to the implementation of a next-generation power insulation system with higher reliability and longer lifespan (section 2.2). Two different approaches, extrinsic and intrinsic, were used to exquisitely design the self-healing functions in polymeric materials (section 2.3). Although a great deal of research has been carried out on self-healing polymers, the demand for robust dielectric strength and the special form of electrical tree damage are both challenges to the introduction of self-healing techniques into HV insulating materials (section 2.4). With the easy polycondensation process, tailorable characteristics, and suitable self-healing matrix, PU elastomers are well positioned to develop as self-healing dielectrics with robust electrical strength (section 2.5). The implementation of adaptive dielectric materials and their application in high voltage insulation is reviewed, where the key is the construction of percolation channels using functional fillers with excellent non-linear electrical response (section 2.6.1 & section 2.6.2). Two-dimension GO nanosheets are a potential option for the organic integration of self-adaptive and self-healing functions into a dielectric due to their extremely low percolation threshold and abundance of surface reactive groups (section 2.7). To the best of our knowledge, there is no research into organic integration of electrical and dielectric self-adaptive and self-healing functions into an electrically insulating material.

Chapter 3 presented the design and synthesis route of a series of PU elastomers with different phase-separated degree and the methodology widely used in this thesis. Four PU elastomers with different degrees of phase separation were developed by adjusting the molecular length and equivalent weight of the polyol in the synthesis process. PU film samples with certain thickness were obtained by hot pressing, ready for further various tests (section 3.2). The principles and operating procedures of the calculations and experiments commonly used in this thesis are listed, including electronic structure simulation of polymers based on quantum chemical calculations (section 3.3.1), FTIR to describe chemical composition (section 3.3.2), AFM to probe material morphology (section 3.3.3), comprehensive characterisation of electrical, thermal and mechanical

properties (section 3.3.4, 3.3.5, 3.3.6, and 3.3.9), and DRS and TSDC to model the dielectric relaxation behaviour of materials (section 3.3.7 & section 3.3.8).

Chapter 4 comprehensively investigated the structure-activity relationships of microphase-separated PU elastomers and screened out PU samples with robust dielectric strength for potential application in HV insulation. The chemical composition of PU samples and their hydrogen bonding status were characterized by deconvoluted FTIR spectroscopy (section 4.2). The order synthesis with no significant by-products of designed PUs and the hydrogen bonding structure was confirmed in this section, where the latter plays an important role in driving the self-healing behaviours of PUs. AFM results clearly exhibited the microphase separated topography of designed PUs (section 4.3). The hard domain switched from a sporadic dotted distribution to a continuous banded distribution with the increase of HS%. Microphase separated structure greatly improved the insulating properties of PU elastomers, including DC conductivity and DC breakdown strength, as well as the higher HS%, the more pronounced the improvement obtains (section 4.4). PU2 and PU3 with phase separated structures and shorter polyol chains shows better insulation performance than the common industrial silicone rubber. The interrelationship between the microstructure of PUs and their electrical properties were characterized in terms of the dielectric relaxation behaviours and quantum chemical simulation. The interfacial relaxation originating from the phase interface between the soft and hard domains of the PU features a deeper energy level and an elevated proportion of interfacial charge as the HS% rises (section 4.5). Similar results also indicated in the electronic structure simulation of typical PU repeating unit (section 4.6). With an energy barrier of 0.1916 eV between the SS and HS of the phase-separated PU, local states with deeper energy levels trap the free charge to the detrimental to charge transfer, thus enhancing their insulating properties. Combining the results of the thermal and mechanical properties, the phase separated PUs, PU2 and PU3, with shorter polyols, are suitable for application on HV insulation (section 4.7). These two PU samples with robust dielectric strength are selected to verify their self-healing performance under electrical damage in the chapter 5.

Chapter 5 characterized and evaluated the self-healing performance of microphase separated PU elastomers under electrical damage. The reversibility of the hydrogen

bonding networks of PUs was confirmed by variable temperature FTIR (section 5.2). The re-crosslinking temperature of PU2 and PU3 is 50 ℃ and 100 ℃, respectively. The shape memory effect was evaluated by conformational entropy obtained from DMA results (section 5.3). PU2 with higher conformational entropy tends to show more efficient shape memory effects at plateaus above the T_g, which is beneficial to self-healing. The DMA results also show that the softening temperatures (70 ℃) of PU2 and PU3 are close to each other, which means that PU2 is able to reconstruct its hydrogen bonding cross-linked network at 50 °C and preserve the overall strength of the material, whereas for PU3 the reconstitution temperature of 100°C is higher than its softening temperature and cannot be used as a self-healing material. PU2 exhibited efficient self-healing capability under electrical damage, containing the repair of dendritic channels and the recovery of insulating properties (section 5.4). An experimental platform was set up to induce electrical ageing, provide healing conditions and perform in situ microscopic observations (section 5.4.1). After 48 hours of repair at 50 °C, 2D optical micrographs, 3D computed micro-X-ray tomography, and cross-sectional SEM images all confirmed that the micro dendritic defects in PU2 had completely healed (section 5.4.2). Moreover, the insulating performance of PU2 assessed by the maximum discharge amplitude (Q_m) of the PD returned to normal with the damage area healed (section 5.4.3). The self-healing mechanism of PU2 is attributed to its shape memory effect driven by high conformational entropy and the reversibility of hydrogen bonds (Figure 5-10). PU2, a self-healing polymer with excellent dielectric strength, is an ideal smart matrix for further development through the introduction of a self-adapting function in the chapter 6.

Chapter 6 designed and implemented grafted GO/PU nanocomposites with simultaneous self-healable and self-adapting electrical and dielectric behaviours. In the material design phase, electronic structure simulations were first performed based on the established grafted GO/PU molecular model (section 6.2.1). The energy barrier of the GO oxide layer is significantly reduced after grafting, which may be beneficial for the construction of high-quality percolation channels. The preparation techniques of a series of grafted and solution blended GO/PU nanocomposites were described (section 6.2.2), while the reaction process and the unfolding state of GO are verified by FTIR and AFM (section 6.3.3), separately. The grafted composite with 5% volume fraction of GO

exhibits superior nonlinear dielectric and electrical behaviour with a switching field strength of 0.7 kV/mm, a nonlinear coefficient of 4.7, and a saturation current of 6.3 nA/mm^2, which are much better than those of the blended composite with the same GO concentration and satisfy the demand for self-adaptive resistive and capacitive field grading materials for most engineering applications (section 6.3). The improved nonlinear electrical behaviours of the grafted composites are mainly attributed to the tailored interfacial effects (section 6.4). The combination tests of EFM and KPFM showed the interesting phenomenon that the interface between the GO and the PU matrix of the blended composite forms a "wall" that blocks charge transport along the percolation channels connected by GO sheets. In contrast, the injected charge in the grafted material distinctly prefers to migrate between adjacent GO sheets (Figure 6-9). The TSDC results also demonstrate that the interfacial barrier of GO/PU is substantially narrowed after grafting, thereby reducing the energy dissipated by the charge flow through the GO percolation channel. The self-healing and self-adapting capabilities of grafted GO/PU nanocomposites were displayed in a designed electrode structure with typical distortion electric field (section 6.5). The maximum distortion field of the system at an applied voltage of 3 kV was reduced by 79.2% after the application of GGO_5 with good nonlinear electrical properties based on the simulation results (section 6.5.1). The grafted GO/PU nanocomposites reveal repeatable self-healing capabilities under the stimulation both of light irradiation and heating, involving the recovery of its novel nonlinear electrical properties and structural restoration (section 6.5.2). The brand-new light healing method for the composite introduced by the photothermal effect of GO achieved exceed 90% healing efficiency in five times of aging-healing cycles.

7.2 Recommendations for Future Work

With the bright vision of developing the next generation of advanced power and electronic equipment, this thesis has undertaken a great deal of research in the field of smart insulation materials. The self-adaptive and self-healing dielectrics developed in this thesis may be a significant step towards realising this vision. However, there are many addition aspects presented in this thesis that can be further explored and achieved:

- For the investigation of the structure-activity relationships of PU elastomers presented in chapter 4, more model PUs can be design and prepared to expand the sample size. For example, the mechanisms by which different types of isocyanates, polyols, or chain extenders affect the properties of model PUs are well worth exploring. A well-developed structure-property database would be very useful for designing versatile PUs for various applications.
- For the self-healing PU based on reversible hydrogen bonding networks described in chapter 5, the introduction of some new self-repair mechanisms, such as Diels-Alder reactions, disulfide bonding, siloxanes, etc., may help to construct PU with higher healing efficiency. The combined use of multiple self-healing mechanisms may result in better repair performance for more demanding application scenarios [200]. Additionally, the competing relationship between self-healing and ageing is a potential research focus. Currently, healing and ageing are considered to be incapable of occurring at the same time. However, the ideal practical application of self-healing materials is to continuously heal their micro damage during operation. Some materials that use thermal, optical, and free radicals generated during the aging process for healing may be promising for this purpose.
- In the chapter 6, we have chosen two-dimensional GO as a functional filler to integrate self-healing and self-adaptive functions. However, there are also some promising two-dimensional semi-conducting fillers, such as MXene [201], black phosphorus [202]. that are attractive. Compared to GO, these new low-dimensional materials still have a lot of new phenomena and functions to be discovered due to their more recent discovery. Look forward to developing brand-new nano-dielectrics with them to achieve some unique functionality.
- In practical engineering applications of self-healing dielectrics, a localised self-healing is undoubtedly more cost effective and less disruptive to the whole system if the material can autonomously report the damaged area, for example through colour changes or fluorescence to indicate the damage status. The organic integration of such a self-reporting capability into a self-healing and self-adaptive dielectric is both desirable and challenging. This self-reporting ability must be triggered by electrical damage, i.e., a small defect, while maintaining reversibility consistent with self-healing, i.e., no reporting after material healing. Conventional reversible

photochromism and thermochromism are not sufficient to be driven by slight electrical damage. Structural coloration, the vibrant colour of many biological systems, is produced by periodically ordered nanostructures, giving the opportunity to produce a colour response to small perturbations. The right-handed twisted CNC (Cellulose nanocrystals) with negatively charged sulphate half-ester groups tend to self-assemble into a nematic structure at a sufficient concentration, giving rise to an iridescent structural colour [203], [204]. CNC may be an attempted path to achieve this goal.

Reference

[1] "Energy – In Brief," *Dep. Business, Energy Ind. Strateg.*, Feb. 2022, doi: 10.1111/j.1467-6346.2022.10404.x.

[2] J. Nieto, H. Pollitt, P. E. Brockway, L. Clements, M. Sakai, and J. Barrett, "Socio-macroeconomic impacts of implementing different post-Brexit UK energy reduction targets to 2030," *Energy Policy*, vol. 158, no. December 2020, p. 112556, 2021, doi: 10.1016/j.enpol.2021.112556.

[3] Y. Zhou, S. Peng, J. Hu, and J. He, "Polymeric insulation materials for HVDC cables: Development, challenges and future perspective," *IEEE Trans. Dielectr. Electr. Insul.*, vol. 24, no. 3, pp. 1308–1318, 2017, doi: 10.1109/TDEI.2017.006205.

[4] Z. Li and B. Du, "Polymeric insulation for high-voltage dc extruded cables: Challenges and development directions," *IEEE Electr. Insul. Mag.*, vol. 34, no. 6, pp. 30–43, 2018, doi: 10.1109/MEI.2018.8507715.

[5] Z. Liu, F. Zhang, J. Yu, K. Gao, and W. Ma, "Research on key technologies in ±1100 kV ultra-high voltage DC transmission," *High Volt.*, vol. 3, no. 4, pp. 279–288, 2018, doi: 10.1049/hve.2018.5023.

[6] Y. Shu, Z. Zhang, J. Guo, and Z. Zhang, "Study on key factors and solution of renewable energy accommodation," *Proc. Chinese Soc. Electr. Eng.*, vol. 37, no. 1, pp. 1–8, 2017, doi: 10.13334/j.0258-8013.pcsee.162555.

[7] T. Christen, L. Donzel, and F. Greuter, "Nonlinear resistive electric field grading part 1: Theory and simulation," *IEEE Electr. Insul. Mag.*, vol. 26, no. 6, pp. 47–59, 2010, doi: 10.1109/MEI.2010.5599979.

[8] A. Can-Ortiz, L. Laudebat, Z. Valdez-Nava, and S. Diaham, "Nonlinear electrical conduction in polymer composites for field grading in high-voltage applications: A review," *Polymers*, vol. 13, no. 9, p. 1370, 2021.

[9] X. Yang, S. Wang, Z. Huang, X. Zhao, J. Hu, Q. Li, and J. He, “Surface treated ZnO whisker optimizing the comprehensive performance of the self-adaptive dielectrics,” *Compos. Sci. Technol.*, vol. 233, no. January, pp. 1–9, 2023, doi: 10.1016/j.compscitech.2023.109918.

[10] S. K. M. Haque, J. A. Ardila-Rey, Y. Umar, A. A. Mas’ud, F. Muhammad-Sukki, B. H. Jume, H. Rahman, and N. A. Bani, “Application and Suitability of Polymeric Materials as Insulators in Electrical Equipment,” *Energies*, vol. 14, no. 10. 2021. doi: 10.3390/en14102758.

[11] E. A. Cherney, “Nanodielectrics Applications — Today and Tomorrow,” *IEEE Electr. Insul. Mag.*, vol. 29, no. 6, pp. 59–65, 2013.

[12] H. Xu, C. Xie, B. Gou, R. Wang, J. Zhou, and L. Li, “Core-double-shell structured BT@TiO2@PDA and oriented BNNSs doped epoxy nanocomposites with field-dependent nonlinear electrical properties and enhancing breakdown strength,” *Compos. Sci. Technol.*, vol. 230, no. P1, p. 109777, 2022, doi: 10.1016/j.compscitech.2022.109777.

[13] L. Donzel, F. Greuter, and T. Christen, “Nonlinear resistive electric field grading part 2: Materials and applications,” *IEEE Electr. Insul. Mag.*, vol. 27, no. 2, pp. 18–29, 2011, doi: 10.1109/MEI.2011.5739419.

[14] X. Zhao, X. Yang, L. Gao, Q. Li, J. Hu, and J. He, “Tuning the potential distribution of AC cable terminals by stress cone of nonlinear conductivity material,” *IEEE Trans. Dielectr. Electr. Insul.*, vol. 24, no. 5, pp. 2686–2693, 2017, doi: 10.1109/TDEI.2017.006043.

[15] X. Zhao, X. Yang, J. Hu, H. Wang, H. Yang, Q. Li, J. He, Z. Xu, and X. Li, “Grading of electric field distribution of AC polymeric outdoor insulators using field grading material,” *IEEE Trans. Dielectr. Electr. Insul.*, vol. 26, no. 4, pp. 1253–1260, 2019, doi: 10.1109/TDEI.2019.007989.

[16] X. Chen, Q. Wang, X. Huang, M. Awais, A. Paramane, and N. Ren, “Investigation of Electrical and Thermal Properties of Epoxy Resin/Silicon Carbide Whisker

Composites for Electronic Packaging Materials," *IEEE Trans. Components, Packag. Manuf. Technol.*, vol. 12, no. 7, pp. 1109–1121, 2022, doi: 10.1109/TCPMT.2022.3178741.

[17] Mechen, Liu, Yunpeng, Liu, Yanda, Li, Ping, Zheng, Haoran, and Rui, "Growth and partial discharge characteristics of electrical tree in XLPE under AC-DC composite voltage," *IEEE Trans. Dielectr. Electr. Insul.*, vol. 24, no. 4, pp. 2282–2290, 2017.

[18] Chen, Xiangrong, Xu, Yang, Cao, Xiaolong, Dodd, S., Dissado, and L., "Effect of tree channel conductivity on electrical tree shape and breakdown in XLPE cable insulation samples.," *IEEE Trans. Dielectr. Electr. Insul.*, vol. 18, no. 3, pp. 847–860, 2011.

[19] H. Wutzel, M. Jarvid, J. M. Bjuggren, A. Johansson, V. Englund, S. Gubanski, and M. R. Andersson, "Thioxanthone derivatives as stabilizers against electrical breakdown in cross-linked polyethylene for high voltage cable applications," *Polym. Degrad. Stab.*, vol. 112, pp. 63–69, 2015.

[20] T. Tanaka, "Dielectric nanocomposites with insulating properties," *IEEE Trans. Dielectr. Electr. Insul.*, vol. 12, no. 5, pp. 914–928, 2005, doi: 10.1109/TDEI.2005.1522186.

[21] L. A. Dissado, "Theoretical basis for the statistics of dielectric breakdown," *J. Phys. D. Appl. Phys.*, vol. 23, no. 12, pp. 1582–1591, 1990.

[22] M. S. Ganewatta, Z. Wang, and C. Tang, "Chemical syntheses of bioinspired and biomimetic polymers toward biobased materials," *Nat. Rev. Chem.*, vol. 5, no. 11, pp. 753–772, 2021, doi: 10.1038/s41570-021-00325-x.

[23] D. Nepal, M. J. Buehler, P. V. Coveney, and K. Dayal, "Hierarchically structured bioinspired nanocomposites," *Nat. Mater.*, vol. 22, no. 1, pp. 18–35, 2023, doi: 10.1038/s41563-022-01384-1.

[24] D. Stuart-Fox and A. Moussalli, “Selection for Social Signalling Drives the Evolution of Chameleon Colour Change,” *PLOS Biol.*, vol. 6, no. 1, p. e25, Jan. 2008, doi: 10.1371/journal.pbio.0060025.

[25] J. R. Capadona, K. Shanmuganathan, D. J. Tyler, S. J. Rowan, and C. Weder, “Stimuli-responsive polymer nanocomposites inspired by the sea cucumber dermis,” *Science*, vol. 319, no. 5868, pp. 1370–1374, 2008, doi: 10.1126/science.1153307.

[26] Y. Zhou, L. Li, Z. Han, Q. Li, J. He, and Q. Wang, “Self-Healing Polymers for Electronics and Energy Devices,” *Chem. Rev.*, vol. 123, no. 2, pp. 558–612, 2023, doi: 10.1021/acs.chemrev.2c00231.

[27] M. Qi, R. Yang, Z. Wang, Y. Liu, Q. Zhang, B. He, K. Li, Q. Yang, L. Wei, C. Pan, and M. Chen, “Bioinspired Self-healing Soft Electronics,” *Adv. Funct. Mater.*, vol. 33, no. 17, p. 2214479, Apr. 2023, doi: 10.1002/adfm.202214479.

[28] X. Huang, L. Han, X. Yang, Z. Huang, J. Hu, Q. Li, and J. He, “Smart dielectric materials for next-generation electrical insulation,” *iEnergy*, vol. 1, no. 1, pp. 19–49, 2022, doi: 10.23919/ien.2022.0007.

[29] Z. Shen, Z. Jia, Y. Hao, Z. Xin, and X. Wang, “A fabrication method for adaptive dielectric gradient insulating components,” *High Volt.*, vol. 8, no. 1, pp. 59–69, 2023, doi: 10.1049/hve2.12211.

[30] C. Liu, Y. Zheng, B. Zhang, X. Zheng, S. Hu, and K. Han, “Review of Nonlinear Conductivity Theory Research of Modified Composite Materials,” *IEEE Access*, vol. 7, pp. 50536–50548, 2019, doi: 10.1109/ACCESS.2019.2906662.

[31] H. Xu, B. Gou, J. He, Y. Lu, H. Chen, L. Li, C. Xie, and X. M. Hu, “Tunable nonlinear conductive behavior without percolation threshold and high thermal conductivity of epoxy resin/SiC ceramic foam co-continuous phase composites,” *Compos. Sci. Technol.*, vol. 236, no. January, p. 109984, 2023, doi: 10.1016/j.compscitech.2023.109984.

[32] X. Zhao, X. Yang, Q. Li, J. He, and J. Hu, “Synergistic effect of ZnO microspherical varistors and carbon fibers on nonlinear conductivity and mechanical properties of the silicone rubber-based material,” *Compos. Sci. Technol.*, vol. 150, pp. 187–193, 2017, doi: 10.1016/j.compscitech.2017.07.025.

[33] X. Yang, J. Hu, S. Wang, P. Meng, X. Zhao, S. Peng, Z. Yuan, C. Yuan, Q. Li, and J. He, “A Dielectric Polymer/Metal Oxide Nanowire Composite for Self-Adaptive Charge Release,” *Nano Lett.*, vol. 22, no. 13, pp. 5167–5174, 2022, doi: 10.1021/acs.nanolett.2c00887.

[34] S. Ishibe, M. Mori, M. Kozako, and M. Hikita, “A New Concept Varistor With Epoxy/Microvaristor Composite,” *IEEE Trans. Power Deliv.*, vol. 29, no. 2, pp. 677–682, 2014, doi: 10.1109/TPWRD.2013.2281850.

[35] B. J. Blaiszik, S. L. B. Kramer, S. C. Olugebefola, J. S. Moore, N. R. Sottos, and S. R. White, “Self-Healing Polymers and Composites,” *Annu. Rev. Mater. Res.*, vol. 40, no. 1, pp. 179–211, Jun. 2010, doi: 10.1146/annurev-matsci-070909-104532.

[36] Y. Yang, J. He, Q. Li, L. Gao, J. Hu, R. Zeng, J. Qin, S. X. Wang, and Q. Wang, “Self-healing of electrical damage in polymers using superparamagnetic nanoparticles,” *Nat. Nanotechnol.*, vol. 14, no. 2, pp. 151–155, 2019.

[37] Y. Wang, Y. Li, Z. Zhang, and Y. Zhang, “Effect of doping microcapsules on typical electrical performances of self-healing polyethylene insulating composite,” *Appl. Sci.*, vol. 9, no. 15, p. 3039, 2019.

[38] L. Gao, Y. Yang, J. Xie, S. Zhang, J. Hu, R. Zeng, J. He, Q. Li, and Q. Wang, “Autonomous self-healing of electrical degradation in dielectric polymers using in situ electroluminescence,” *Matter*, vol. 2, no. 2, pp. 451–463, 2020.

[39] J. Xie, L. Gao, J. Hu, Q. Li, and J. He, “Self-healing of electrical damage in thermoset polymers: Via anionic polymerization,” *J. Mater. Chem. C*, vol. 8, no. 18, pp. 6025–6033, 2020, doi: 10.1039/c9tc06989e.

[40] J. Xie, L. Han, Z. Luo, Q. Li, and J. He, “Microcapsule-Based Autonomous Self-Healing of Electrical Damage in Dielectric Polymers Induced by In Situ Generated Radicals,” *ACS Appl. Mater. Interfaces*, vol. 15, no. 8, pp. 11185–11192, 2023, doi: 10.1021/acsami.3c00520.

[41] A. V Menon, G. Madras, and S. Bose, “Light weight, ultrathin, and ‘thermally-clickable’ self-healing MWNT patch as electromagnetic interference suppressor,” *Chem. Eng. J.*, vol. 366, pp. 72–82, 2019.

[42] J. Xie, M. Yang, J. Liang, J. Hu, Q. Li, and J. He, “Self-healing of internal damage in mechanically robust polymers utilizing a reversibly convertible molecular network,” *J. Mater. Chem. A*, vol. 9, no. 29, pp. 15975–15984, 2021, doi: 10.1039/d1ta03512f.

[43] J. F. Patrick, M. J. Robb, N. R. Sottos, J. S. Moore, and S. R. White, “Polymers with autonomous life-cycle control,” *Nature*, vol. 540, no. 7633, pp. 363–370, 2016, doi: 10.1038/nature21002.

[44] N. F. Mohd Sani, H. J. Yee, N. Othman, A. A. Talib, and R. K. Shuib, “Intrinsic self-healing rubber: A review and perspective of material and reinforcement,” *Polym. Test.*, vol. 111, p. 107598, 2022, doi: 10.1016/j.polymertesting.2022.107598.

[45] S. Qin, Y. Tu, S. Wang, Y. Cheng, B. Chen, C. Wang, and Y. Zhang, “Accelerated aging of fast thermal cycle effects on the behavior of space charge in polyimide,” *IEEE Trans. Dielectr. Electr. Insul.*, vol. 24, no. 5, pp. 3182–3190, 2017, doi: 10.1109/TDEI.2017.006483.

[46] G. C. Stone, I. Culbert, E. A. Boulter, and H. Dhirani, “Historical Development of Insulation Materials and Systems,” in *Electrical Insulation for Rotating Machines: Design, Evaluation, Aging, Testing, and Repair*, 2014, pp. 83–110. doi: 10.1002/9781118886663.ch3.

[47] I. Pleşa, P. V Noţingher, S. Schlögl, C. Sumereder, and M. Muhr, “Properties of Polymer Composites Used in High-Voltage Applications,” *Polymers*, vol. 8, no. 5, 2016, doi: 10.3390/polym8050173.

[48] S. Li, S. Yu, and Y. Feng, “Progress in and prospects for electrical insulating materials,” *High Volt.*, vol. 1, no. 3, pp. 122–129, Oct. 2016, doi: https://doi.org/10.1049/hve.2016.0034.

[49] T. J. Lewis, “Ageing-a perspective,” *IEEE Electr. Insul. Mag.*, vol. 17, no. 4, pp. 6–16, 2001, doi: 10.1109/57.948978.

[50] A. M. Pourrahimi, R. T. Olsson, and M. S. Hedenqvist, “The Role of Interfaces in Polyethylene/Metal-Oxide Nanocomposites for Ultrahigh-Voltage Insulating Materials,” *Adv. Mater.*, vol. 30, no. 4, pp. 1–25, 2018, doi: 10.1002/adma.201703624.

[51] D. Q. Tan, “The search for enhanced dielectric strength of polymer-based dielectrics: A focused review on polymer nanocomposites,” *J. Appl. Polym. Sci.*, vol. 137, no. 33, p. 49379, Sep. 2020, doi: 10.1002/app.49379.

[52] L. Zhang, M. Khani, T. M. Krentz, Y. Huang, Y. Zhou, B. C. Benicewicz, J. K. Nelson, and L. S. Schadler, “Suppression of space charge in crosslinked polyethylene filled with poly(stearyl methacrylate)-grafted SiO2 nanoparticles,” *Appl. Phys. Lett.*, vol. 110, p. 132903, 2017.

[53] K. Wu, J. Fang, J. Ma, R. Huang, S. Chai, F. Chen, and Q. Fu, “Achieving a Collapsible, Strong, and Highly Thermally Conductive Film Based on Oriented Functionalized Boron Nitride Nanosheets and Cellulose Nanofiber,” *ACS Appl. Mater. Interfaces*, vol. 9, no. 35, pp. 30035–30045, Sep. 2017, doi: 10.1021/acsami.7b08214.

[54] H. Kim, A. A. Abdala, and C. W. MacOsko, “Graphene/polymer nanocomposites,” *Macromolecules*, vol. 43, no. 16, pp. 6515–6530, 2010, doi: 10.1021/ma100572e.

[55] G. Junguo, Z. Jinmei, J. Quanquan, L. Jiayin, Z. Mingyan, and Z. Xiaohong, "Study on brekdown and paitial discharge of polyethylene/montmorillonite nanocomposites," in *2008 International Symposium on Electrical Insulating Materials (ISEIM 2008)*, 2008, pp. 597–600. doi: 10.1109/ISEIM.2008.4664479.

[56] T. Tanaka, A. Bulinski, J. Castellon, M. Frechette, S. Gubanski, J. Kindersberger, G. C. Montanari, M. Nagao, P. Morshuis, Y. Tanaka, S. Pelissou, A. Vaughan, Y. Ohki, C. W. Reed, S. Sutton, and S. J. Han, "Dielectric properties of XLPE/Sio2 nanocomposites based on CIGRE WG D1.24 cooperative test results," *IEEE Trans. Dielectr. Electr. Insul.*, vol. 18, no. 5, pp. 1482–1517, 2011, doi: 10.1109/TDEI.2011.6032819.

[57] E. and I. S. Department for Business, "Chapter 6: Renewable sources of energy Chart 6.1 Use of renewable fuels, 2021 (Table 6.4) *Including non-biodegradable waste," vol. 2021, 2022.

[58] C. Zhou, H. Yi, and X. Dong, "Review of recent research towards power cable life cycle management," *High Volt.*, vol. 2, no. 3, pp. 179–187, Sep. 2017, doi: 10.1049/hve.2017.0037.

[59] B. Mouawad, L. Yang, P. Agyakwa, M. Corfield, and C. M. Johnson, "Packaging degradation studies of High Temperature SiC MOSFET discrete packages," in *2020 32nd International Symposium on Power Semiconductor Devices and ICs (ISPSD)*, 2020, pp. 90–93. doi: 10.1109/ISPSD46842.2020.9170030.

[60] C. Li, Y. Yang, G. Xu, Y. Zhou, M. Jia, S. Zhong, Y. Gao, C. Park, Q. Liu, Y. Wang, S. Akram, X. Zeng, Y. Li, F. Liang, B. Cui, J. Fang, and L. Tang, "Insulating materials for realising carbon neutrality: Opportunities, remaining issues and challenges," *High Volt.*, vol. 7, no. 4, pp. 610–632, Aug. 2022, doi: 10.1049/hve2.12232.

[61] Y. Yang, X. Ding, and M. W. Urban, "Chemical and physical aspects of self-healing materials," *Prog. Polym. Sci.*, vol. 49, pp. 34–59, 2015.

[62] S. Wang and M. W. Urban, “Self-healing polymers,” *Nat. Rev. Mater.*, vol. 5, no. 8, pp. 562–583, 2020, doi: 10.1038/s41578-020-0202-4.

[63] S. R. White, N. R. Sottos, P. H. Geubelle, J. S. Moore, M. R. Kessler, S. R. Sriram, E. N. Brown, and S. Viswanathan, “Autonomic healing of polymer composites,” *Nature*, vol. 409, no. 6822, pp. 794–797, 2001, doi: 10.1038/35057232.

[64] E. N. Brown, S. R. White, and N. R. Sottos, “Retardation and repair of fatigue cracks in a microcapsule toughened epoxy composite – Part I: Manual infiltration,” *Compos. Sci. Technol.*, vol. 65, no. 15, pp. 2466–2473, 2005, doi: 10.1016/j.compscitech.2005.04.020.

[65] G. O. Wilson, J. S. Moore, S. R. White, N. R. Sottos, and H. M. Andersson, “Autonomic Healing of Epoxy Vinyl Esters via Ring Opening Metathesis Polymerization,” *Adv. Funct. Mater.*, vol. 18, no. 1, pp. 44–52, Jan. 2008, doi: 10.1002/adfm.200700419.

[66] H. Jin, G. M. Miller, N. R. Sottos, and S. R. White, “Fracture and fatigue response of a self-healing epoxy adhesive,” *Polymer (Guildf).*, vol. 52, no. 7, pp. 1628–1634, 2011, doi: 10.1016/j.polymer.2011.02.011.

[67] M. M. Caruso, B. J. Blaiszik, H. Jin, S. R. Schelkopf, D. S. Stradley, N. R. Sottos, S. R. White, and J. S. Moore, “Robust, Double-Walled Microcapsules for Self-Healing Polymeric Materials,” *ACS Appl. Mater. Interfaces*, vol. 2, no. 4, pp. 1195–1199, Apr. 2010, doi: 10.1021/am100084k.

[68] Y. C. Yuan, M. Z. Rong, M. Q. Zhang, J. Chen, G. C. Yang, and X. M. Li, “Self-Healing Polymeric Materials Using Epoxy/Mercaptan as the Healant,” *Macromolecules*, vol. 41, no. 14, pp. 5197–5202, Jul. 2008, doi: 10.1021/ma800028d.

[69] M. W. Keller, S. R. White, and N. R. Sottos, “A Self-Healing Poly(Dimethyl Siloxane) Elastomer,” *Adv. Funct. Mater.*, vol. 17, no. 14, pp. 2399–2404, Sep. 2007, doi: https://doi.org/10.1002/adfm.200700086.

[70] M. W. Keller, S. R. White, and N. R. Sottos, “Torsion fatigue response of self-healing poly(dimethylsiloxane) elastomers,” *Polymer (Guildf).*, vol. 49, no. 13, pp. 3136–3145, 2008, doi: 0.1016/j.polymer.2008.04.041.

[71] D. O. Grigoriev, K. Köhler, E. Skorb, D. G. Shchukin, and H. Möhwald, “Polyelectrolyte complexes as a ‘smart’ depot for self-healing anticorrosion coatings,” *Soft Matter*, vol. 5, no. 7, pp. 1426–1432, 2009, doi: 10.1039/B815147D.

[72] V. Sauvant-Moynot, S. Gonzalez, and J. Kittel, “Self-healing coatings: An alternative route for anticorrosion protection,” *Prog. Org. Coatings*, vol. 63, no. 3, pp. 307–315, 2008, doi: 10.1016/j.porgcoat.2008.03.004.

[73] A. M. Aragón, J. K. Wayer, P. H. Geubelle, D. E. Goldberg, and S. R. White, “Design of microvascular flow networks using multi-objective genetic algorithms,” *Comput. Methods Appl. Mech. Eng.*, vol. 197, no. 49, pp. 4399–4410, 2008, doi: 10.1016/j.cma.2008.05.025.

[74] H. R. Williams, R. S. Trask, and I. P. Bond, “Self-healing composite sandwich structures,” *Smart Mater. Struct.*, vol. 16, no. 4, p. 1198, 2007, doi: 10.1088/0964-1726/16/4/031.

[75] M. Q. Zhang and M. Z. Rong, “Intrinsic self-healing of covalent polymers through bond reconnection towards strength restoration,” *Polym. Chem.*, vol. 4, no. 18, pp. 4878–4884, 2013, doi: 10.1039/c3py00005b.

[76] A. V. Menon, G. Madras, and S. Bose, “The journey of self-healing and shape memory polyurethanes from bench to translational research,” *Polym. Chem.*, vol. 10, no. 32, pp. 4370–4388, 2019, doi: 10.1039/c9py00854c.

[77] I. L. Hia, V. Vahedi, and P. Pasbakhsh, “Self-Healing Polymer Composites: Prospects, Challenges, and Applications,” *Polym. Rev.*, vol. 56, no. 2, pp. 225–261, Apr. 2016, doi: 10.1080/15583724.2015.1106555.

[78] C.-M. Chung, Y.-S. Roh, S.-Y. Cho, and J.-G. Kim, “Crack Healing in Polymeric Materials via Photochemical [2+2] Cycloaddition,” *Chem. Mater.*, vol. 16, no. 21, pp. 3982–3984, Oct. 2004, doi: 10.1021/cm049394+.

[79] J. Ling, M. Z. Rong, and M. Q. Zhang, “Photo-stimulated self-healing polyurethane containing dihydroxyl coumarin derivatives,” *Polymer (Guildf).*, vol. 53, no. 13, pp. 2691–2698, 2012, doi: 10.1016/j.polymer.2012.04.016.

[80] Y. Pan, X. Yu, P. Yang, J. Li, D. Zhang, L. Liu, and Y. Wang, “The influence of furanyl monomer on the self-healing polyurethanes by reverse Diels-Alder cross-link,” *Polym. Adv. Technol.*, vol. 30, no. 3, pp. 804–807, Mar. 2019, doi: 10.1002/pat.4507.

[81] J. Canadell, H. Goossens, and B. Klumperman, “Self-Healing Materials Based on Disulfide Links,” *Macromolecules*, vol. 44, no. 8, pp. 2536–2541, Apr. 2011, doi: 10.1021/ma2001492.

[82] C. Yuan, M. Z. Rong, and M. Q. Zhang, “Self-healing polyurethane elastomer with thermally reversible alkoxyamines as crosslinkages,” *Polymer*, vol. 55, no. 7, pp. 1782–1791, 2014, doi: 10.1016/j.polymer.2014.02.033.

[83] K. Imato, M. Nishihara, T. Kanehara, Y. Amamoto, A. Takahara, and H. Otsuka, “Self-Healing of Chemical Gels Cross-Linked by Diarylbibenzofuranone-Based Trigger-Free Dynamic Covalent Bonds at Room Temperature,” *Angew. Chemie*, vol. 124, no. 5, pp. 1164–1168, 2012, doi: 10.1002/ange.201104069.

[84] J. Kang, D. Son, G.-J. N. Wang, Y. Liu, J. Lopez, Y. Kim, J. Y. Oh, T. Katsumata, J. Mun, Y. Lee, L. Jin, J. B.-H. Tok, and Z. Bao, “Tough and Water-Insensitive Self-Healing Elastomer for Robust Electronic Skin,” *Adv. Mater.*, vol. 30, no. 13, p. 1706846, Mar. 2018, doi: 10.1002/adma.201706846.

[85] Y.-L. Rao, A. Chortos, R. Pfattner, F. Lissel, Y.-C. Chiu, V. Feig, J. Xu, T. Kurosawa, X. Gu, C. Wang, M. He, J. W. Chung, and Z. Bao, “Stretchable Self-Healing Polymeric Dielectrics Cross-Linked Through Metal–Ligand

Coordination," *J. Am. Chem. Soc.*, vol. 138, no. 18, pp. 6020–6027, May 2016, doi: 10.1021/jacs.6b02428.

[86] S. Burattini, B. W. Greenland, W. Hayes, M. E. Mackay, S. J. Rowan, and H. M. Colquhoun, "A Supramolecular Polymer Based on Tweezer-Type π−π Stacking Interactions: Molecular Design for Healability and Enhanced Toughness," *Chem. Mater.*, vol. 23, no. 1, pp. 6–8, Jan. 2011, doi: 10.1021/cm102963k.

[87] Y. Huang, P. G. Lawrence, and Y. Lapitsky, "Self-Assembly of Stiff, Adhesive and Self-Healing Gels from Common Polyelectrolytes," *Langmuir*, vol. 30, no. 26, pp. 7771–7777, Jul. 2014, doi: 10.1021/la404606y.

[88] M. Nakahata, Y. Takashima, and A. Harada, "Highly Flexible, Tough, and Self-Healing Supramolecular Polymeric Materials Using Host–Guest Interaction," *Macromol. Rapid Commun.*, vol. 37, no. 1, pp. 86–92, Jan. 2016, doi: 10.1002/marc.201500473.

[89] T. Xie, "Recent advances in polymer shape memory," *Polymer (Guildf).*, vol. 52, no. 22, pp. 4985–5000, 2011, doi: 10.1016/j.polymer.2011.08.003.

[90] C. C. Hornat and M. W. Urban, "Shape memory effects in self-healing polymers," *Prog. Polym. Sci.*, vol. 102, p. 101208, 2020, doi: 10.1016/j.progpolymsci.2020.101208.

[91] W. M. Huang, Z. Ding, C. C. Wang, J. Wei, Y. Zhao, and H. Purnawali, "Shape memory materials," *Mater. Today*, vol. 13, no. 7, pp. 54–61, 2010, doi: 10.1016/S1369-7021(10)70128-0.

[92] C. C. Hornat and M. W. Urban, "Entropy and interfacial energy driven self-healable polymers," *Nat. Commun.*, vol. 11, no. 1, p. 1028, 2020, doi: 10.1038/s41467-020-14911-y.

[93] J. Su, B. Du, J. Li, and Z. Li, "Electrical tree degradation in high-voltage cable insulation: progress and challenges," *High Volt.*, vol. 5, no. 4, pp. 353–364, Aug. 2020, doi: 10.1049/hve.2020.0009.

[94] T. Tanaka and A. Greenwood, “Effects of Charge Injection and Extraction on Tree Initiation in Polyethylene,” *IEEE Trans. Power Appar. Syst.*, vol. PAS-97, no. 5, pp. 1749–1759, 1978, doi: 10.1109/TPAS.1978.354668.

[95] G. Chen and C. H. Tham, “Electrical treeing characteristics in XLPE power cable insulation in frequency range between 20 and 500 Hz,” *IEEE Trans. Dielectr. Electr. Insul.*, vol. 16, no. 1, pp. 179–188, 2009, doi: 10.1109/TDEI.2009.4784566.

[96] H. Zhang, Y. Shang, M. Li, H. Zhao, X. Wang, and B. Han, “Theoretical study on the radical reaction mechanism in the cross-linking process of polyethylene,” *RSC Adv.*, vol. 5, no. 110, pp. 90343–90353, 2015, doi: 10.1039/C5RA16339K.

[97] J. Su, B. Du, T. Han, Z. Li, M. Xiao, and J. Li, “Multistep and Multiscale Electron Trapping for High-Efficiency Modulation of Electrical Degradation in Polymer Dielectrics,” *J. Phys. Chem. C*, vol. 123, no. 12, pp. 7045–7053, Mar. 2019, doi: 10.1021/acs.jpcc.9b00349.

[98] X. Zheng, Y. Liu, and Y. Wang, “Electrical tree inhibition by SiO2/XLPE nanocomposites: insights from first-principles calculations,” *J. Mol. Model.*, vol. 24, no. 8, p. 200, 2018, doi: 10.1007/s00894-018-3742-4.

[99] M. Jarvid, A. Johansson, R. Kroon, J. M. Bjuggren, H. Wutzel, V. Englund, S. Gubanski, M. R. Andersson, and C. Müller, “A new application area for fullerenes: voltage stabilizers for power cable insulation,” *Adv. Mater.*, vol. 27, no. 5, pp. 897–902, 2015.

[100] Y. Zhang, C. Ellingford, R. Zhang, J. Roscow, M. Hopkins, P. Keogh, T. McNally, C. Bowen, and C. Wan, “Electrical and Mechanical Self-Healing in High-Performance Dielectric Elastomer Actuator Materials,” *Adv. Funct. Mater.*, vol. 29, no. 15, p. 1808431, 2019.

[101] L. M. Salvatierra, L. I. Kovalevski, P. L. D. Quiña, I. M. Irurzun, E. E. Mola, S. J. Dodd, and L. A. Dissado, “Self-healing during electrical treeing: A feature of

the two-phase liquid-solid nature of silicone gels," *IEEE Trans. Dielectr. Electr. Insul.*, vol. 23, no. 2, pp. 757–767, 2016, doi: 10.1109/TDEI.2015.004813.

[102] Y. Yang, Z. Dang, Q. Li, and J. He, "Self-Healing of Electrical Damage in Polymers," *Adv. Sci.*, vol. 2002131, p. 2002131, 2020, doi: 10.1002/advs.202002131.

[103] J. Li, Q. Feng, J. Cui, Q. Yuan, H. Qiu, S. Gao, and J. Yang, "Self-assembled graphene oxide microcapsules in Pickering emulsions for self-healing waterborne polyurethane coatings," *Compos. Sci. Technol.*, vol. 151, pp. 282–290, 2017.

[104] M. Ates, S. Karadag, A. A. Eker, and B. Eker, "Polyurethane foam materials and their industrial applications," *Polym. Int.*, vol. 71, no. 10, pp. 1157–1163, Oct. 2022, doi: 10.1002/pi.6441.

[105] M. V Mokeev, S. A. Ostanin, N. N. Saprykina, V. V Zuev, A. V Menon, G. Madras, and S. Bose, "Microphase structure of polyurethane-polyurea copolymers as revealed by solid-state NMR: Effect of molecular architecture," *Polymer*, vol. 150, pp. 72–83, 2018, doi: 10.1016/j.polymer.2018.07.014.

[106] H. R. Heydarnezhad, N. Mohammadi, A. Arbe, and A. Alegria, "How does microstructural design affect the dynamics and rheology of segmented polyurethanes?," *Macromolecules*, vol. 53, no. 13, pp. 5381–5398, 2020, doi: 10.1021/acs.macromol.0c00998.

[107] A. V Menon, G. Madras, and S. Bose, "The journey of self-healing and shape memory polyurethanes from bench to translational research," *Polym. Chem.*, vol. 10, pp. 4370–4388, 2019, doi: 10.1039/c9py00854c.

[108] P. Król, "Synthesis methods, chemical structures and phase structures of linear polyurethanes. Properties and applications of linear polyurethanes in polyurethane elastomers, copolymers and ionomers," *Prog. Mater. Sci.*, vol. 52, no. 6, pp. 915–1015, 2007, doi: 10.1016/j.pmatsci.2006.11.001.

[109] J. Kang, J. B.-H. Tok, and Z. Bao, “Self-healing soft electronics,” *Nat. Electron.*, vol. 2, no. 4, pp. 144–150, 2019.

[110] M. S. Sánchez-Adsuar, “Influence of the composition on the crystallinity and adhesion properties of thermoplastic polyurethane elastomers,” *Int. J. Adhes. Adhes.*, vol. 20, no. 4, pp. 291–298, 2000, doi: 10.1016/S0143-7496(99)00059-7.

[111] A. M. Castagna, D. Fragiadakis, H. Lee, T. Choi, and J. Runt, “The role of hard segment content on the molecular dynamics of poly(tetramethylene oxide)-based polyurethane copolymers,” *Macromolecules*, vol. 44, no. 19, pp. 7831–7836, 2011, doi: 10.1021/ma2017138.

[112] M. Q. Zhang and M. Z. Rong, “Intrinsic self-healing of covalent polymers through bond reconnection towards strength restoration,” *Polym. Chem.*, vol. 4, no. 18, pp. 4878–4884, 2013.

[113] P. D. Tatiya, R. K. Hedaoo, P. P. Mahulikar, and V. V Gite, “Novel Polyurea Microcapsules Using Dendritic Functional Monomer: Synthesis, Characterization, and Its Use in Self-healing and Anticorrosive Polyurethane Coatings,” *Ind. Eng. Chem. Res.*, vol. 52, pp. 1562–1570, 2013, doi: 10.1021/ie301813a.

[114] E. Koh, S. Lee, J. Shin, and Y.-W. Kim, “Renewable Polyurethane Microcapsules with Isosorbide Derivatives for Self-Healing Anticorrosion Coatings,” *Ind. Eng. Chem. Res.*, vol. 52, no. 44, pp. 15541–15548, Nov. 2013, doi: 10.1021/ie402505s.

[115] M. Haghayegh, S. M. Mirabedini, and H. Yeganeh, “Microcapsules containing multi-functional reactive isocyanate-terminated polyurethane prepolymer as a healing agent. Part 1: synthesis and optimization of reaction conditions,” *J. Mater. Sci.*, vol. 51, no. 6, pp. 3056–3068, 2016, doi: 10.1007/s10853-015-9616-6.

[116] Y. Zhang, Y. Qi, and Z. Zhang, “The influence of 2,4-toluene diisocyanate content on the intrinsic self-healing performance of polyurethane at room-temperature,” *J. Polym. Res.*, vol. 22, no. 5, p. 94, 2015, doi: 10.1007/s10965-015-0744-0.

[117] Y. J. Kim, P. H. Huh, and B. K. Kim, “Synthesis of self-healing polyurethane urea-based supramolecular materials,” *J. Polym. Sci. Part B Polym. Phys.*, vol. 53, no. 7, pp. 468–474, Apr. 2015, doi: https://doi.org/10.1002/polb.23653.

[118] P. Du, X. Liu, Z. Zheng, X. Wang, T. Joncheray, and Y. Zhang, “Synthesis and characterization of linear self-healing polyurethane based on thermally reversible Diels–Alder reaction,” *RSC Adv.*, vol. 3, no. 35, pp. 15475–15482, 2013, doi: 10.1039/C3RA42278J.

[119] G. Fu, L. Yuan, G. Liang, and A. Gu, “Heat-resistant polyurethane films with great electrostatic dissipation capacity and very high thermally reversible self-healing efficiency based on multi-furan and liquid multi-maleimide polymers,” *J. Mater. Chem. A*, vol. 4, no. 11, pp. 4232–4241, 2016, doi: 10.1039/C6TA00953K.

[120] L. Ling, J. Li, G. Zhang, R. Sun, and C.-P. Wong, “Self-Healing and Shape Memory Linear Polyurethane Based on Disulfide Linkages with Excellent Mechanical Property,” *Macromol. Res.*, vol. 26, no. 4, pp. 365–373, 2018, doi: 10.1007/s13233-018-6037-9.

[121] G. Li and N. Uppu, “Shape memory polymer based self-healing syntactic foam: 3-D confined thermomechanical characterization,” *Compos. Sci. Technol.*, vol. 70, no. 9, pp. 1419–1427, 2010, doi: 10.1016/j.compscitech.2010.04.026.

[122] E. D. Rodriguez, X. Luo, and P. T. Mather, “Linear/Network Poly(ε-caprolactone) Blends Exhibiting Shape Memory Assisted Self-Healing (SMASH),” *ACS Appl. Mater. Interfaces*, vol. 3, no. 2, pp. 152–161, Feb. 2011, doi: 10.1021/am101012c.

[123] Y. Xu and D. Chen, “A Novel Self-Healing Polyurethane Based on Disulfide Bonds,” *Macromol. Chem. Phys.*, vol. 217, no. 10, pp. 1191–1196, May 2016, doi: 10.1002/macp.201600011.

[124] N. Van Herck and F. E. Du Prez, “Fast Healing of Polyurethane Thermosets Using Reversible Triazolinedione Chemistry and Shape-Memory,” *Macromolecules*, vol. 51, no. 9, pp. 3405–3414, May 2018, doi: 10.1021/acs.macromol.8b00368.

[125] A. Eigner and S. Semino, “50 years of electrical-stress control in cable accessories,” *IEEE Electr. Insul. Mag.*, vol. 29, no. 5, pp. 47–55, 2013, doi: 10.1109/MEI.2013.6585856.

[126] J. Robertson and B. R. Varlow, “The AC non linear permittivity characteristics of barium titanate filled acrylic resin,” in *Proceedings of the 7th International Conference on Properties and Applications of Dielectric Materials (Cat. No.03CH37417)*, 2003, pp. 761–764 vol.2. doi: 10.1109/ICPADM.2003.1218529.

[127] J. Glatz-Reichenbach, B. Meyer, R. Strümpler, P. Kluge-Weiss, and F. Greuter, “New low-voltage varistor composites,” *J. Mater. Sci.*, vol. 31, no. 22, pp. 5941–5944, 1996, doi: 10.1007/BF01152143.

[128] F. Warkusz, “The scattering of electrons on grain boundaries: Electrical conductivity,” *Thin Solid Films*, vol. 161, pp. 1–11, 1988, doi: 10.1016/0040-6090(88)90230-1.

[129] E. Mårtensson, U. Gäfvert, and U. Lindefelt, “Direct current conduction in SiC powders,” *J. Appl. Phys.*, vol. 90, pp. 2862–2869, 2001.

[130] X. Yang, P. Meng, X. Zhao, Q. Li, J. Hu, and J. He, “How nonlinear V-I characteristics of single ZnO microvaristor influences the performance of its silicone rubber composite,” *IEEE Trans. Dielectr. Electr. Insul.*, vol. 25, no. 2, pp. 623–630, 2018, doi: 10.1109/TDEI.2018.006858.

[131] B Nettelblad, E Mårtensson, C Önneby, U Gäfvert, and A Gustafsson, “Two percolation thresholds due to geometrical effects: experimental and simulated results,” *J. Phys. D. Appl. Phys.*, vol. 36, no. 4, p. 399, 2003, doi: 10.1088/0022-3727/36/4/312.

[132] H. Matsuzaki, T. Nakano, and H. Ando, “Effects of second particles on nonlinear resistance properties of microvaristor-filled composites,” in *2012 Annual Report Conference on Electrical Insulation and Dielectric Phenomena*, 2012, pp. 183–186. doi: 10.1109/CEIDP.2012.6378751.

[133] S. Mashkouri, M. Ghafouri, N. Arsalani, H. Bidadi, and H. Mostafavi, "Mechanochemical green synthesis of exfoliated graphite at room temperature and investigation of its nonlinear properties based zinc oxide composite varistors," *J. Mater. Sci. Mater. Electron.*, vol. 28, no. 6, pp. 4839–4846, 2017, doi: 10.1007/s10854-016-6130-9.

[134] Z. Wang, J. K. Nelson, H. Hillborg, S. Zhao, and L. S. Schadler, "Graphene oxide filled nanocomposite with novel electrical and dielectric properties," *Adv. Mater.*, vol. 24, no. 23, pp. 3134–3137, 2012, doi: 10.1002/adma.201200827.

[135] K. Li, B. Zhang, and X. Li, "Electric Field Mitigation in High-Voltage High-Power IGBT Modules Using Nonlinear Conductivity Composites," *IEEE Trans. Components, Packag. Manuf. Technol.*, vol. 11, no. 11, pp. 1844–1855, 2021.

[136] B. X. Du, H. C. Liang, J. Li, and Z. Y. Ran, "Electrical field distribution along SG6/N2 filled DC-GIS/GIL epoxy spacer," *IEEE Trans. Dielectr. Electr. Insul.*, vol. 25, no. 4, pp. 1202–1210, 2018, doi: 10.1109/TDEI.2018.007079.

[137] C. Li, C. Lin, J. Hu, W. Liu, Q. Li, B. Zhang, S. He, Y. Yang, F. Liu, and J. He, "Novel HVDC Spacers by Adaptively Controlling Surface Charges – Part I: Charge Transport and Control Strategy," *IEEE Trans. Dielectr. Electr. Insul.*, vol. 25, no. 4, pp. 1238–1247, 2018, doi: 10.1109/TDEI.2018.007054.

[138] C. Li, C. Lin, Y. Yang, B. Zhang, W. Liu, Q. Li, J. Hu, S. He, X. Liu, and J. He, "Novel HVDC spacers by adaptively controlling surface charges – part ii: experiment," *IEEE Trans. Dielectr. Electr. Insul.*, vol. 25, no. 4, pp. 1248–1258, 2018, doi: 10.1109/TDEI.2018.007056.

[139] C. Lin, Q. Li, C. Li, B. Zhang, W. Liu, Y. Yang, F. Liu, X. Liu, J. Hu, and J. He, "Novel HVDC spacers by adaptively controlling surface charges – part iii: industrialization prospects," *IEEE Trans. Dielectr. Electr. Insul.*, vol. 25, no. 4, pp. 1259–1266, 2018, doi: 10.1109/TDEI.2018.007555.

[140] X. Zhao, J. Hu, Z. Yuan, and J. He, “Design of adaptive bushing based on field grading materials,” *High Volt.*, vol. 6, no. 4, pp. 625–636, 2021, doi: 10.1049/hve2.12090.

[141] N. Wang, I. Cotton, J. Robertson, S. Follmann, K. Evans, and D. Newcombe, “Partial discharge control in a power electronic module using high permittivity non-linear dielectrics,” *IEEE Trans. Dielectr. Electr. Insul.*, vol. 17, no. 4, pp. 1319–1326, 2010, doi: 10.1109/TDEI.2010.5539704.

[142] T. Umemoto, Y. Otake, M. Yoshimura, T. Nada, and R. Miyatake, “Optimization of double-layer stress grading system for high voltage rotating electrical machines by electric field and thermal coupled analysis,” *IEEE Trans. Dielectr. Electr. Insul.*, vol. 27, no. 3, pp. 971–979, 2020, doi: 10.1109/TDEI.2019.008535.

[143] L. Donzel, T. Christen, R. Kessler, F. Greuter, and H. Gramespacher, “Silicone composites for HV applications based on microvaristors,” in *Proceedings of the 2004 IEEE International Conference on Solid Dielectrics, 2004. ICSD 2004.*, 2004, pp. 403-406 Vol.1. doi: 10.1109/ICSD.2004.1350376.

[144] K. S. Novoselov, A. K. Geim, S. V Morozov, D. Jiang, Y. Zhang, S. V Dubonos, I. V Grigorieva, and A. A. Firsov, “Electric Field Effect in Atomically Thin Carbon Films,” *Science (80-.).*, vol. 306, no. 5696, pp. 666–669, Oct. 2004, doi: 10.1126/science.1102896.

[145] M. D. Stoller, S. Park, Y. Zhu, J. An, and R. S. Ruoff, “Graphene-Based Ultracapacitors,” *Nano Lett.*, vol. 8, no. 10, pp. 3498–3502, Oct. 2008, doi: 10.1021/nl802558y.

[146] C. Lee, X. Wei, J. W. Kysar, and J. Hone, “Measurement of the Elastic Properties and Intrinsic Strength of Monolayer Graphene,” *Science*, vol. 321, no. 5887, pp. 385–388, Jul. 2008, doi: 10.1126/science.1157996.

[147] A. A. Balandin, S. Ghosh, W. Bao, I. Calizo, D. Teweldebrhan, F. Miao, and C. N. Lau, “Superior Thermal Conductivity of Single-Layer Graphene,” *Nano Lett.*, vol. 8, no. 3, pp. 902–907, Mar. 2008, doi: 10.1021/nl0731872.

[148] Y. Zhu, S. Murali, W. Cai, X. Li, J. W. Suk, J. R. Potts, and R. S. Ruoff, "Graphene and graphene oxide: Synthesis, properties, and applications," *Adv. Mater.*, vol. 22, no. 35, pp. 3906–3924, 2010, doi: 10.1002/adma.201001068.

[149] V. Singh, D. Joung, L. Zhai, S. Das, S. I. Khondaker, and S. Seal, "Graphene based materials: Past, present and future," *Prog. Mater. Sci.*, vol. 56, no. 8, pp. 1178–1271, 2011, doi: 10.1016/j.pmatsci.2011.03.003.

[150] D. R. Dreyer, S. Park, C. W. Bielawski, and R. S. Ruoff, "The chemistry of graphene oxide," *Chem. Soc. Rev.*, vol. 39, no. 1, pp. 228–240, 2010, doi: 10.1039/b917103g.

[151] H. Kim, Y. Miura, and C. W. MacOsko, "Graphene/polyurethane nanocomposites for improved gas barrier and electrical conductivity," *Chem. Mater.*, vol. 22, no. 11, pp. 3441–3450, 2010, doi: 10.1021/cm100477v.

[152] D. J. Joshi, J. R. Koduru, N. I. Malek, C. M. Hussain, and S. K. Kailasa, "Surface modifications and analytical applications of graphene oxide: A review," *TrAC Trends Anal. Chem.*, vol. 144, p. 116448, 2021, doi: 10.1016/j.trac.2021.116448.

[153] T. Kuilla, S. Bhadra, D. Yao, N. H. Kim, S. Bose, and J. H. Lee, "Recent advances in graphene based polymer composites," *Prog. Polym. Sci.*, vol. 35, no. 11, pp. 1350–1375, 2010, doi: 10.1016/j.progpolymsci.2010.07.005.

[154] T. Kuila, S. Bose, A. K. Mishra, P. Khanra, N. H. Kim, and J. H. Lee, "Chemical functionalization of graphene and its applications," *Prog. Mater. Sci.*, vol. 57, no. 7, pp. 1061–1105, 2012, doi: https://doi.org/10.1016/j.pmatsci.2012.03.002.

[155] Y. Xu, W. Hong, H. Bai, C. Li, and G. Shi, "Strong and ductile poly(vinyl alcohol)/graphene oxide composite films with a layered structure," *Carbon N. Y.*, vol. 47, no. 15, pp. 3538–3543, 2009, doi: 10.1016/j.carbon.2009.08.022.

[156] H.-B. Zhang, W.-G. Zheng, Q. Yan, Y. Yang, J.-W. Wang, Z.-H. Lu, G.-Y. Ji, and Z.-Z. Yu, "Electrically conductive polyethylene terephthalate/graphene

nanocomposites prepared by melt compounding," *Polymer*, vol. 51, no. 5, pp. 1191–1196, 2010, doi: 10.1016/j.polymer.2010.01.027.

[157] M. A. Rafiee, J. Rafiee, I. Srivastava, Z. Wang, H. Song, Z.-Z. Yu, and N. Koratkar, "Fracture and Fatigue in Graphene Nanocomposites," *Small*, vol. 6, no. 2, pp. 179–183, Jan. 2010, doi: 10.1002/smll.200901480.

[158] H. Kim, Y. Miura, and C. W. Macosko, "Graphene/Polyurethane Nanocomposites for Improved Gas Barrier and Electrical Conductivity," *Chem. Mater.*, vol. 22, no. 11, pp. 3441–3450, Jun. 2010, doi: 10.1021/cm100477v.

[159] K. Kalaitzidou, H. Fukushima, and L. T. Drzal, "Multifunctional polypropylene composites produced by incorporation of exfoliated graphite nanoplatelets," *Carbon N. Y.*, vol. 45, no. 7, pp. 1446–1452, 2007, doi: 10.1016/j.carbon.2007.03.029.

[160] O. C. Compton, S. Kim, C. Pierre, J. M. Torkelson, and S. T. Nguyen, "Crumpled Graphene Nanosheets as Highly Effective Barrier Property Enhancers," *Adv. Mater.*, vol. 22, no. 42, pp. 4759–4763, Nov. 2010, doi: 10.1002/adma.201000960.

[161] M. Fang, K. Wang, H. Lu, Y. Yang, and S. Nutt, "Covalent polymer functionalization of graphene nanosheets and mechanical properties of composites," *J. Mater. Chem.*, vol. 19, no. 38, pp. 7098–7105, 2009, doi: 10.1039/B908220D.

[162] A. Reghunadhan and S. Thomas, "Chapter 1 - Polyurethanes: Structure, Properties, Synthesis, Characterization, and Applications," S. Thomas, J. Datta, J. T. Haponiuk, and A. B. T.-P. P. Reghunadhan, Eds., Amsterdam: Elsevier, 2017, pp. 1–16. doi: 10.1016/B978-0-12-804039-3.00001-4.

[163] T. Lu and F. Chen, "Multiwfn: A multifunctional wavefunction analyzer," *J. Comput. Chem.*, vol. 33, no. 5, pp. 580–592, 2012, doi: 10.1002/jcc.22885.

[164] P. Schön, K. Bagdi, K. Molnár, P. Markus, B. Pukánszky, and G. Julius Vancso, "Quantitative mapping of elastic moduli at the nanoscale in phase separated

polyurethanes by AFM," *Eur. Polym. J.*, vol. 47, no. 4, pp. 692–698, 2011, doi: 10.1016/j.eurpolymj.2010.09.029.

[165] D. Pedrazzoli and I. Manas-Zloczower, "Understanding phase separation and morphology in thermoplastic polyurethanes nanocomposites," *Polymer*, vol. 90, pp. 256–263, 2016, doi: 10.1016/j.polymer.2016.03.022.

[166] D. B. Hall, P. Underhill, and J. M. Torkelson, "Spin coating of thin and ultrathin polymer films," *Polym. Eng. Sci.*, vol. 38, no. 12, pp. 2039–2045, Dec. 1998, doi: 10.1002/pen.10373.

[167] L. Jiang, J. Wu, C. Nedolisa, A. Saiani, and H. E. Assender, "Phase Separation and Crystallization in High Hard Block Content Polyurethane Thin Films," *Macromolecules*, vol. 48, no. 15, pp. 5358–5366, 2015, doi: 10.1021/acs.macromol.5b01083.

[168] M. Furukawa, K. Kojio, S. Kugumiya, Y. Uchiba, and Y. Mitsui, "Microphase separation of bulk and ultrathin films of polyurethane elastomers," *Macromol. Symp.*, vol. 267, no. 1, pp. 9–15, 2008, doi: 10.1002/masy.200850702.

[169] A. Kanapitsas and P. Pissis, "Dielectric relaxation spectroscopy in crosslinked polyurethanes based on polymer polyols," *Eur. Polym. J.*, vol. 36, no. 6, pp. 1241–1250, 2000, doi: 10.1016/S0014-3057(99)00167-6.

[170] S. Qin, Y. Tu, T. Tan, S. Wang, Z. Yuan, C. Wang, L. Li, and Z. Wu, "The effects of γ-ray on charging behaviour using polyimide," *J. Phys. D. Appl. Phys.*, vol. 51, no. 24, p. 245302, 2018, doi: 10.1088/1361-6463/aac375.

[171] R. Chen, "Methods for kinetic analysis of thermally stimulated processes," *J. Mater. Sci.*, vol. 11, no. 8, pp. 1521–1541, 1976, doi: 10.1007/BF00540887.

[172] R. CHEN and Y. KIRSH, "Chapter 6 - Methods for Evaluating Parameters from Thermally Stimulated Curves," in *The Analysis of Thermally Stimulated Processes*, vol. 15, R. CHEN and Y. KIRSH, Eds., in International Series in the

Science of the Solid State, vol. 15. , Amsterdam: Pergamon, 1981, pp. 144–182. doi: 10.1016/B978-0-08-022930-0.50012-8.

[173] A. W. Grzelak, P. Boinard, and J. J. Liggat, “The influence of diol chain extender on morphology and properties of thermally-triggered UV-stable self-healing polyurethane coatings,” *Prog. Org. Coatings*, vol. 122, pp. 1–9, 2018.

[174] A. K. Mishra, D. K. Chattopadhyay, B. Sreedhar, and K. V. S. N. Raju, “FT-IR and XPS studies of polyurethane-urea-imide coatings,” *Prog. Org. Coatings*, vol. 55, no. 3, pp. 231–243, 2006, doi: 10.1016/j.porgcoat.2005.11.007.

[175] B. Imre, H. Gojzewski, C. Check, R. Chartoff, and G. J. Vancso, “Properties and Phase Structure of Polycaprolactone-Based Segmented Polyurethanes with Varying Hard and Soft Segments: Effects of Processing Conditions,” *Macromol. Chem. Phys.*, vol. 219, no. 2, pp. 1–13, 2018, doi: 10.1002/macp.201700214.

[176] W. Wang and S. Li, “Research status and development of insulation breakdown in engineering solid dielectrics,” *Kexue Tongbao/Chinese Sci. Bull.*, vol. 65, no. 31, pp. 3461–3474, 2020, doi: 10.1360/TB-2019-0563.

[177] P. Ortiz-Serna, M. Carsí, B. Redondo-Foj, M. J. Sanchis, M. Culebras, C. M. Gõmez, and A. Cantarero, “Thermal and dielectric properties of polycarbonatediol polyurethane,” *J. Appl. Polym. Sci.*, vol. 132, no. 22, pp. 1–8, 2015, doi: 10.1002/app.42007.

[178] R. R. Mocellini, O. A. Lambri, C. L. Matteo, and P. A. Sorichetti, “Dielectric Properties and Viscoelastic Response in Two-Phase Polymers,” *IEEE Trans. Dielectr. Electr. Insul.*, vol. 15, no. 4, pp. 982–993, 2008, doi: 10.1109/TDEI.2008.4591219.

[179] G. Sauti and D. S. McLachlan, “Impedance and modulus spectra of the percolation system silicon–polyester resin and their analysis using the two exponent phenomenological percolation equation,” *J. Mater. Sci.*, vol. 42, no. 16, pp. 6477–6488, 2007, doi: 10.1007/s10853-007-1564-3.

[180] D. Favero, V. Marcon, C. A. Figueroa, C. M. Gómez, and O. Bianchi, “Effect of chain extender on the morphology, thermal, viscoelastic, and dielectric behavior of soybean polyurethane,” *J. Appl. Polym. Sci.*, 2021.

[181] K. Nakamae, T. Nishino, S. Asaoka, and Sudaryanto, “Relationships between interfacial properties and structure of segmented polyurethane having functional groups,” *Int. J. Adhes. Adhes.*, vol. 19, no. 5, pp. 345–351, 1999, doi: 10.1016/S0143-7496(98)00051-7.

[182] C. Tsonos, L. Apekis, C. Zois, and G. Tsonos, “Microphase separation in ion-containing polyurethanes studied by dielectric measurements,” *Acta Mater.*, vol. 52, no. 5, pp. 1319–1326, 2004, doi: 10.1016/j.actamat.2003.11.015.

[183] H. P. Diogo and J. J. Moura Ramos, “Contribution of the technique of thermostimulated currents for the elucidation of the nature of the Johari-Goldstein and other secondary relaxations in the vitreous state,” *IEEE Trans. Dielectr. Electr. Insul.*, vol. 21, no. 5, pp. 2301–2309, 2014, doi: 10.1109/TDEI.2014.004078.

[184] A. M. Kamalov and M. E. Borisova, “The influence of moisture on charge relaxation in modified polyimide films,” *St. Petersbg. Polytech. Univ. J. Phys. Math.*, vol. 2, no. 3, pp. 188–192, 2016, doi: 10.1016/j.spjpm.2016.08.008.

[185] W. Sun, J. Xu, J. Song, Y. Chen, Z. Lv, Y. Cheng, and L. Zhang, “Self-healing of electrical damage in insulating robust epoxy containing dynamic fluorine-substituted carbamate bonds for green dielectrics,” *Mater. Horizons*, 2023.

[186] T. Takada, H. Kikuchi, H. Miyake, Y. Tanaka, M. Yoshida, and Y. Hayase, “Determination of charge-trapping sites in saturated and aromatic polymers by quantum chemical calculation,” *IEEE Trans. Dielectr. Electr. Insul.*, vol. 22, no. 2, pp. 1240–1249, 2015, doi: 10.1109/TDEI.2015.7076827.

[187] L. Li and G. Yang, “Variable-temperature FTIR studies on thermal stability of hydrogen bonding in nylon 6/mesoporous silica nanocomposite,” *Polym. Int.*, vol. 58, no. 5, pp. 503–510, 2009, doi: 10.1002/pi.2559.

[188] C. C. Hornat and M. W. Urban, “Entropy and interfacial energy driven self-healable polymers,” *Nat. Commun.*, vol. 11, no. 1, pp. 1–9, 2020, doi: 10.1038/s41467-020-14911-y.

[189] P. C. Hiemenz and T. P. Lodge, *Polymer Chemistry*. CRC Press, 2007. doi: 10.1201/9781420018271.

[190] C. C. Hornat, Y. Yang, and M. W. Urban, “Quantitative Predictions of Shape-Memory Effects in Polymers,” *Adv. Mater.*, vol. 29, no. 7, pp. 1–8, 2017, doi: 10.1002/adma.201603334.

[191] I. S. Gunes, F. Cao, and S. C. Jana, “Evaluation of nanoparticulate fillers for development of shape memory polyurethane nanocomposites,” *Polyme*, vol. 49, no. 9, pp. 2223–2234, 2008, doi: 10.1016/j.polymer.2008.03.021.

[192] H. Meng and G. Li, “A review of stimuli-responsive shape memory polymer composites,” *Polymer*, vol. 54, no. 9, pp. 2199–2221, 2013, doi: 10.1016/j.polymer.2013.02.023.

[193] Y. Zhou, Y. Zhu, W. Xu, and Q. Wang, “Molecular Trap Engineering Enables Superior High-Temperature Capacitive Energy Storage Performance in All-Organic Composite at 200 °C,” *Adv. Energy Mater.*, vol. 13, no. 11, p. 2203961, Mar. 2023, doi: 10.1002/aenm.202203961.

[194] Y. Xu, H. Bai, G. Lu, C. Li, and G. Shi, “Flexible Graphene Films via the Filtration of Water-Soluble Noncovalent Functionalized Graphene Sheets,” *J. Am. Chem. Soc.*, vol. 130, no. 18, pp. 5856–5857, May 2008, doi: 10.1021/ja800745y.

[195] S. Peng, Z. Luo, S. Wang, J. Liang, C. Yuan, Z. Yuan, J. Hu, J. He, and Q. Li, “Mapping the Space Charge at Nanoscale in Dielectric Polymer Nanocomposites,” *ACS Appl. Mater. Interfaces*, vol. 12, no. 47, pp. 53425–53434, 2020, doi: 10.1021/acsami.0c13669.

[196] S. Wang, Z. Luo, J. Liang, S. Peng, J. Hu, J. He, and Q. Li, “Nanoscale mapping of electric polarizability in a heterogeneous dielectric material with surface

irregularities," *Nanotechnology*, vol. 32, no. 50, p. 505711, 2021, doi: 10.1088/1361-6528/ac26ff.

[197] C. Lin, D. Sheng, X. Liu, S. Xu, F. Ji, L. Dong, Y. Zhou, and Y. Yang, "NIR induced self-healing electrical conductivity polyurethane/graphene nanocomposites based on Diels−Alder reaction," *Polymer*, vol. 140, pp. 150–157, 2018, doi: 10.1016/j.polymer.2018.02.036.

[198] Y. Ha, Y. N. Kim, and Y. C. Jung, "Rapid and Local Self-Healing Ability of Polyurethane Nanocomposites Using Photothermal Polydopamine-Coated Graphene Oxide Triggered by Near-Infrared Laser," *Polymers*, vol. 13, 2021.

[199] J. Zhu, H. Zhang, F. Li, J. Liu, and Y. Lin, "Photothermal effect of graphene/polymer smart nanocomposites under NIR stimuli," *Appl. Phys. A Mater. Sci. Process.*, vol. 127, no. 10, pp. 1–9, 2021, doi: 10.1007/s00339-021-04900-3.

[200] J. Liu, Z. Zhou, X. Su, J. Cao, M. Chen, and R. Liu, "Stiff UV-Curable self-healing coating based on double reversible networks containing diels-alder cross-linking and hydrogen bonds," *Prog. Org. Coatings*, vol. 146, p. 105699, 2020, doi: 10.1016/j.porgcoat.2020.105699.

[201] W. Zhang, X.-X. Ji, and M.-G. Ma, "Emerging MXene/cellulose composites: Design strategies and diverse applications," *Chem. Eng. J.*, vol. 458, p. 141402, 2023, doi: 10.1016/j.cej.2023.141402.

[202] Y. Zhang, C. Y. Ma, J. L. Xie, H. Agren, and H. Zhang, "Black Phosphorus/Polymers: Status and Challenges," *Adv. Mater.*, vol. 33, no. 37, 2021, doi: 10.1002/adma.202100113.

[203] Z. L. Zhang, X. Dong, Y. Y. Zhao, F. Song, X. L. Wang, and Y. Z. Wang, "Bioinspired Optical Flexible Cellulose Nanocrystal Films with Strain-Adaptive Structural Coloration," *Biomacromolecules*, vol. 23, no. 10, pp. 4110–4117, 2022, doi: 10.1021/acs.biomac.2c00491.

[204] Y. Xu and R. J. Hickey, “Solvent-Responsive and Reversible Structural Coloration in Nanostructured Block Polymer Films,” *Macromolecules*, vol. 53, no. 14, pp. 5711–5719, 2020, doi: 10.1021/acs.macromol.0c00639.